Ionospheric Dynamics by GNSS total electron content observations : the effect of Solar Eclipses and the mystery of Earthquake precursors.

Julian Eisenbeis

To cite this version:

Julian Eisenbeis. Ionospheric Dynamics by GNSS total electron content observations : the effect of Solar Eclipses and the mystery of Earthquake precursors.. Earth Sciences. Université Paris Cité, 2020. English. NNT : 2020UNIP7027 . tel-03181359

HAL Id: tel-03181359
https://theses.hal.science/tel-03181359
Submitted on 25 Mar 2021

UNIVERSITÉ DE PARIS

Thèse préparée
à l'INSTITUT DE PHYSIQUE DU GLOBE DE PARIS
École doctorale STEP'UP – ED N°560
IPGP – Équipe de Planétologie et Sciences Spatiales

Ionospheric Dynamics by GNSS total electron content observations: the effect of Solar Eclipses and the mystery of Earthquake precursors

par
Julian Eisenbeis
présentée et soutenue publiquement le
23 Janvier 2020

Thèse de doctorat de Sciences de la Terre et de l'environnement

dirigée par Giovanni Occhipinti

devant un jury composé de:

Gauthier Hulot	IPGP	Président du jury
Kosuke Heki	Hokkaido University	Rapporteur
Anthea Coster	MIT Haystack Observatory	Rapporteur
Eric Calais	ENS	Examinateur
Mattia Crespi	University of Rome 'La Sapienza'	Examinateur
Giovanni Occhipinti	IPGP	Directeur de thèse

Abstract

This thesis focuses mainly on two topics: one is the ionospheric signature of solar eclipses, the second is the Hole vs Enhancement debate about earthquake precursors. On the 21st August 2017 the shadow of a total eclipse drastically changed the state of the ionosphere over the USA. This effect is visible in the total electron content (TEC) measured by ~3000 GNSS stations seeing multiple GPS and GLONASS satellites. This tremendous dataset allows high-resolution characterization of the frequency content and wavelengths -using an omega-k analysis based on 3D Fast-Fourier-Transform (FFT)- of the eclipse signature in the ionosphere in order to fully identify traveling ionospheric disturbances (TIDs). We confirm the generation of TIDs associated with the eclipse including TIDs interpreted as bow waves in previous studies. Additionally we reveal, for the first time, short (50-100 km) and long (500-600 km) wavelength TIDs with periods between 30 and 65 min (Eisenbeis et al., 2019). On 2nd July 2019 another total solar eclipse happened across the South American continent at magnetic conjugate latitudes as the Great American Eclipse, and consequently useful to visualize the difference response. Although for the South American eclipse we have only data from more than hundred GNSS stations and located in a zone close to the sunset, we can show the clear evidence of the ionospheric signature of the eclipse (Eisenbeis & Occhipinti in prep.a).

The second major topic in this work is the still ongoing debate about the possibility of earthquake precursors. Heki (2011) sparked this debate when he published results of the Tohoku earthquake showing a TEC enhancement before the earthquake. The enhancement claimed by Heki (2011) has been interpreted as a decrease in the background TEC after the seismic event, the so called ionospheric hole in literature. The existence of the enhancement has been promoted by several papers (e.g. He & Heki, 2017) extending the observation to several events with moderate magnitude (M> 7.5) and proposes a new vision of the rupture dynamics. By trying to reproduce their results we show that the reference curve used by Heki (2011) to define the TEC background is strongly affected by the order of polynomial fit as well as the selected time windows. This shows that the TEC enhancement could be, in fact, just an artifact, subjectively selected to create the presumed precursor (Eisenbeis & Occhipinti in prep.b).

key words

Ionosphere

GNSS

Total electron content (TEC)

Solar Eclipse

Traveling ionospheric disturbances (TID)

Earthquake precursor

Resumé en Français

Cette thèse porte principalement sur deux sujets: l'un est la signature ionosphérique des éclipses solaires, l'autre est le débat ‘Hole vs Enhancement’. Le 21 août 2017, l'ombre d'une éclipse totale a changé radicalement l'état de l'ionosphère au-dessus des Etats-Unis. Cet effet est visible dans le contenu total en électrons (TEC) mesuré par ~3000 stations GNSS qui voient des multiples satellites GPS et GLONASS. Ce formidable ensemble de données permet une caractérisation à haute résolution du contenu en fréquences et des longueurs d'onde - en utilisant une analyse omega-k basée sur la Transformée de Fourier Rapide (FFT) 3D - de la signature de l'éclipse dans l'ionosphère afin d'identifier complètement les perturbations ionosphériques mobiles (TID). Nous confirmons la génération de TIDs associées à l'éclipse, y compris les TIDs interprétées comme des ondes de proue dans les études précédentes. De plus, nous révélons, pour la première fois, des TID de courte (50-100 km) et de longue (500-600 km) longueurs d'onde avec des périodes entre 30 et 65 min (Eisenbeis et al., 2019). Le 2 juillet 2019, une autre éclipse solaire totale s'est produite à travers le continent sud-américain. Bien que nous n'ayons que des données provenant de plus de cent stations GNSS et situées dans une zone proche du coucher du soleil, nous pouvons montrer la preuve évidente de la signature ionosphérique de l'éclipse (Eisenbeis & Occhipinti in prep.a). Le deuxième grand sujet de ce travail est le débat sur la possibilité de précurseurs de séismes. Heki (2011) a suscité ce débat en publiant les résultats du séisme de Tohoku montrant une amélioration de la TEC avant le séisme. L'amélioration revendiquée par Heki (2011) a été interprétée comme une diminution de la TEC après l'événement, le soi-disant trou ionosphérique dans la littérature. L'existence de l'amélioration a été promue par plusieurs articles (e.g. He & Heki, 2017) étendant l'observation à plusieurs événements de magnitude modérée (M> 7.5) et propose une nouvelle vision de la dynamique de rupture. En essayant de reproduire leurs résultats, nous montrons que la courbe de référence utilisée par Heki (2011) est affectée par l'ordre d'ajustement polynomial ainsi que par les fenêtres temporelles sélectionnées. Ceci montre que l'amélioration du TEC pourrait en fait n'être qu'un artefact, subjectivement sélectionné pour créer le précurseur présumé (Eisenbeis & Occhipinti in prep.b).

Mots clefs

Ionosphère

GNSS

Contenu total en électrons (TEC)

Éclipse solaire

TID

Précurseur des séismes

Table of Contents

1 Introduction – the Ionosphere

The ionosphere is the ionized part of the atmosphere created by the excitation of neutral molecules by the solar radiation. Due to the atmospheric density decreasing with altitude the ionization process starts to be effective at around 60-80 km of altitude, where the ionization process produces free electrons and ions. Lower than that, the density of the atmosphere is high enough that an excited molecule loses electrons, but they are immediately trapped by other ions (recombination process). This production of electrons and ions continuously grows until 300 km, where the ionization process reaches the maximum (Figure 1). After 300 km, the density of the atmosphere becomes so low that the balance between the production (more effective at this altitude) and the recombination (less effective at this altitude) doesn't produce enough free electrons and ions, consequently the electron density decreases progressively (Figure 1).

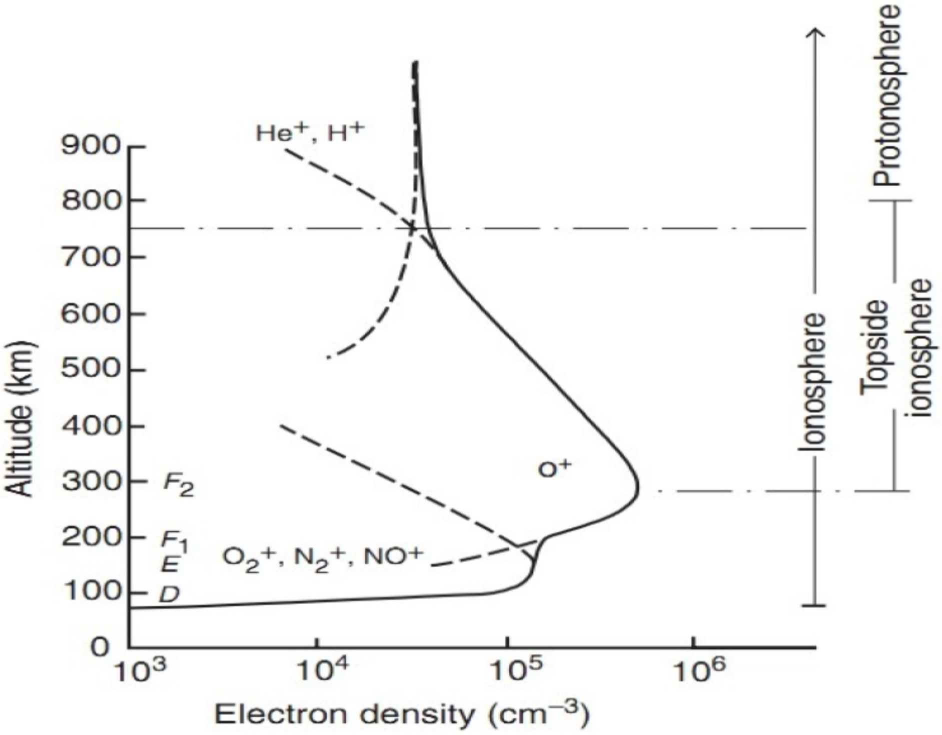

Figure 1: Ionospheric composition at different altitudes. From: Banks (1976)

The probably most popular phenomenon related to the ionosphere is the aurora borealis which is visible for the human eye. The earliest datable observation was in March 567 BC in Babylon (Stephenson, 2004). At that time the geomagnetic latitude was different to today and so auroras were visible in this region. They described an unusual ‘red glow’ in the sky at night without knowledge of the source of this phenomenon. Other reports of the aurora date back to the stone age or can be found in the Old Testament by greek philosophers and in old Chinese writings dating back to 2000 BC. But it wasn’t until 1621 when Galileo suggested the name Aurora Borealis. The very first observation in the southern hemisphere was only in 1773 (Aurora Australis). Anyway, it took some more time until in 1839 Carl F. Gauss, a German mathematician and physicist, was the first to speculate about an ionized region in the upper atmosphere to explain variations of the magnetic field observed at the surface of the Earth (Schunk & Nagy, 2000). The next important step in the discovery of the ionosphere was the proof of the existence of electromagnetic waves, which are strongly affected by the ionosphere when passing through there, by Heinrich Hertz in Karlsruhe in 1887 which lead to the first transatlantic communication established by Guglielmo Marconi. His first claim of a successful transmission was and still is highly contested (Belrose, 2004). Feeling challenged Marconi prepared a better organized and documented test. The SS Philadelphia sailed west of Great Britain in February 1902 recording signals sent daily. The biggest distance in radio transmission was achieved during the night and this was the first time to show that radio signals for medium- and long-wave transmissions travel farther at night. In December 1902 the worlds first radio transmission crossed the Atlantic from the Marconi station in Nova Scotia. Independently and almost simultaneously both Kennelly and Heaviside suggested the presence of a permanent electrically conducting layer high in the atmosphere to explain this achievement (Gillmor, 1982) but it wasn’t until 1924 when Appleton could prove the existence of the ionosphere by broadcasting a continuous signal from a BBC transmitter in Bournemouth to Oxford. Appleton and his student Barnett could determine the height of the reflecting layer at 100 km altitude in comparing the difference in travel time between direct wave along the ground and the signal reflected in the ionosphere (Appleton & Barnett, 1925). In 1926 the Scottish physicist Robert Watson-Watt first introduced the term *ionosphere* in a letter to the United Kingdom Radio Research Board (Watson-Watt, 1929). Later on in 1947 Appleton was awarded the Nobel prize for this achievement and the detected layer was called E layer by Appleton. A possible explanation is that the letter E is supposed to represent the electric field of the waves but the reason for his choice isn't fully clear.

Over the next years there was considerable progress in ionospheric research. Appleton could describe the index of refraction (which depends on the electron density) and the polarization of a plane wave propagating in a plasma, taking into account the magnetic field, absorbing effects and collisions of the electrons. Nowadays the results of those preliminary studies are known as the Appleton-Hartree equation. Sydney Chapman also formulated his theory of the formation of the ionized layers due to the effect of solar ultraviolet (UV) radiation (Chapman, 1931). Because knowledge regarding gas composition, temperature and density was scarce in 1931, Chapman was free to introduce assumptions in the most convenient way. He considered the upper atmosphere as an isothermal plane-stratified region called the Chapman layer. Furthermore, he assumed that density varied exponentially with height. Sunlight ionizes the molecules and as a result produces electrons and positive ions. The electrons remain free for a short time before recombination with the ions which establishes an equilibrium where the rate of production is equal to that of loss. As radiation loses strength as it descends and gas density increases the closer to the Earth, Chapman thought there must be a maximum of free electrons at a certain altitude. He expressed it in a mathematical equation but also illustrated it with graphical curves. Those curves of electron density are called Chapman profile (Anduaga, 2009).

1.1 Structure of the Ionosphere

The Sun's radiation, mainly ultraviolet radiation, is the primary source for the formation of the ionosphere as it ionizes neutral atoms and molecules in the upper atmosphere. A significant amount of electrons and ions are created during the ionization process and could be later recombined. Therefore the ionosphere is an electrically balanced medium. The rate of ionization also depends on neutral density decreasing with height. As quickly mentioned above, at the bottom of the atmosphere the density of molecules is so high that ionization immediately leads to recombination. This is prevailing until 60 to 80 km of altitude. Above this altitude the density is low enough for free electrons to exist. The density of the atmosphere decreases continuously and so does the formation of ions and free electrons until about 300 km where it reaches its maximum. In regions higher than 300 km the atmospheric density is so low that even the most effective ionization processes produce less free electrons than at 300 km. There is no supply of new ions due to the lack of sun radiation during the night and so the electron density gradually diminishes with continuing recombination processes. A characteristic plasma density profile and a representative ion composition are shown in Figure 1. The atmosphere is primarily composed of the gases molecular nitrogen (N_2, 78%), dioxygen (O_2, 21%) and Argon (1%) which make up more than 99% of the air. In the E-region, defined by Appleton, (~150 km) the NO^+ and O_2^+ ions prevail. In general, the ionosphere is described by layers. The following layer, called the F-region, contains the most of the ions: O^+ predominates at altitudes around 200 km and H^+ starts to increase above 300. A general overview of ionospheric 'layers' during day and night is shown in Figure 2.

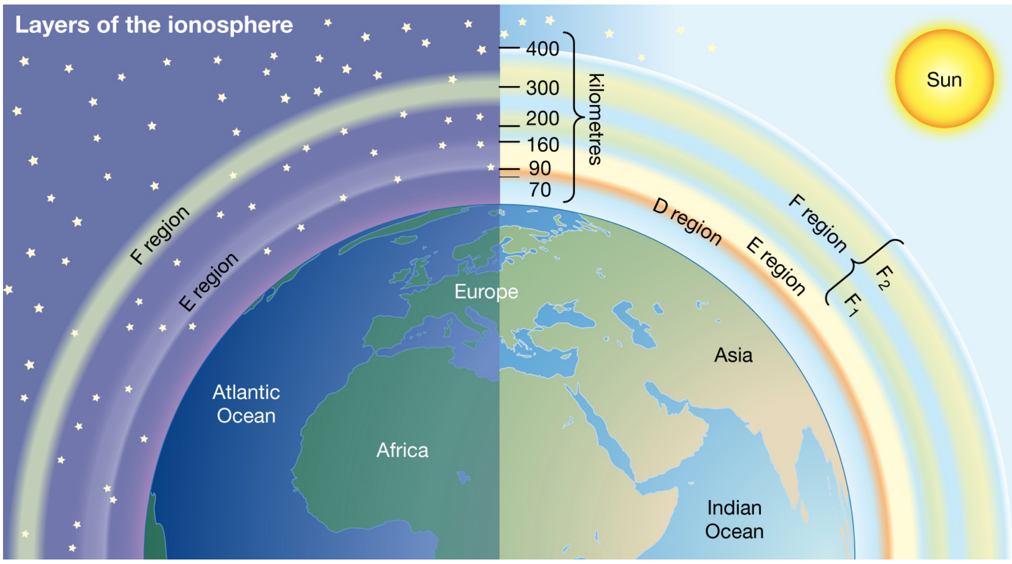

Figure 2: Ionospheric layers during day and night.

The detailed description of each layer will follow. The dynamics of the ionosphere is described with the following reactions:

Photo-ionization reactions:

$$O+h\upsilon\xrightarrow{p_{flux}}O^{+\cdot}+e \tag{1}$$

$$O_2+h\upsilon\xrightarrow{p_{flux}}O_2^{+\cdot}+e \tag{2}$$

$$N_2+h\upsilon\xrightarrow{p_{flux}}N_2^{+\cdot}+e \tag{3}$$

Ion-molecule recombination reactions:

$$O^{+\cdot}+N_2\xrightarrow{\beta}NO^{+\cdot}+N \tag{4}$$

$$O^{+\cdot}+O_2\xrightarrow{\beta}O_2^{+\cdot}+O \tag{5}$$

$$N_2^{+\cdot}+O_2\xrightarrow{\beta}O_2^{+\cdot}+N_2 \tag{6}$$

$$N_2^{+\cdot}+O\xrightarrow{\beta}O^{+\cdot}+N_2 \tag{7}$$

$$N_2^{+\cdot}+O\xrightarrow{\beta}NO^{+\cdot}+N \tag{8}$$

$$O_2^{+\cdot}+N\xrightarrow{\beta}NO^{+\cdot}+O \tag{9}$$

Ion-electron recombination reactions:

$$NO^{+\cdot}+e\xrightarrow{\alpha}N+O \tag{10}$$

$$O_2^{+\cdot} + e \xrightarrow{\alpha} O + O \tag{11}$$

$$N_2^{+\cdot} + e \xrightarrow{\alpha} N + N \tag{12}$$

1.1.1 E region

The E-layer is principally constituted by molecular ions (NO^+, O_2^+, N_2^+). Due to the short recombination time transport processes can be neglected. Photo-ionization plays a dominant role. Chemical processes in the E-layer happens by photo-ionization (Formula 2 and 3), then by recombination reaction (8, 9) and all the ion-electron recombination processes. With the restrictions of the neutral plasma and neglecting transport processes the continuity equation takes the following form:

$$\frac{\partial n_i}{\partial t} = \pm \beta n_i - \alpha n_i^2 + p_{flux} \tag{13}$$

where the parameters α, β and p_{flux} are the recombination frequency (ion-molecule and ion-electron), and the rate of photo ionization which depends mainly on the solar flux but also on the altitude. The profiles of those parameters are shown in Figure 3

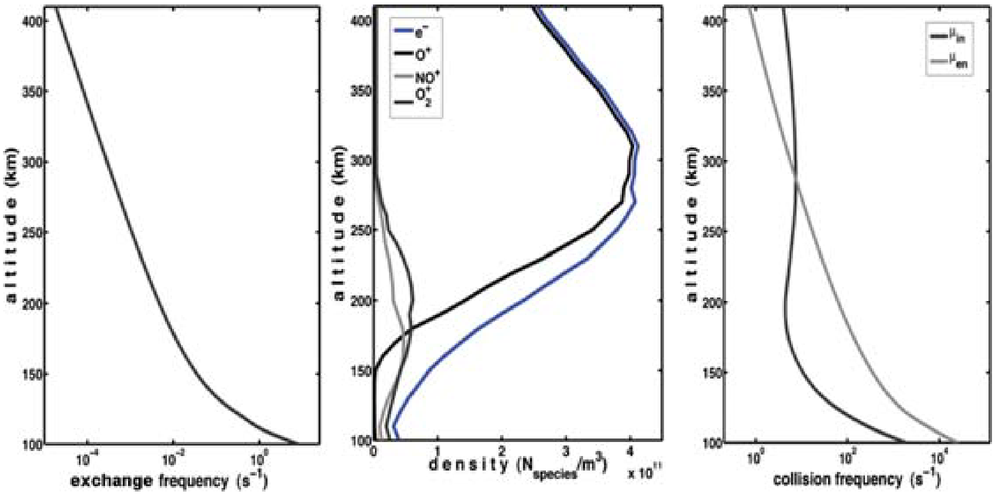

Figure 3: Ionospheric parameter profiles. Left: Ion-molecular exchange frequency; Middle: the three ion species O^+, NO^+, O_2^+ and electron e^- densities; Right: neutral-ion μ_{in} and neutral-electron μ_{en} collision frequencies. From: Occhipinti et al. (2008)

As described above the E-layer is driven mainly by the effect of the Sun. Its weak ionization rate also makes it insensitive to the magnetic field.

Mainly during summer the so-called sporadic E-layer can form sporadically. This composes of thin clouds of intense ionization and can last from several minutes to hours. In general the sporadic E-layers are very narrow but can appear at all altitudes as well as multiple layers simultaneously separated by only a few km. The layer densities reach up to one order of magnitude bigger than the background densities and this layer contains primarily metallic ions (e.g. Fe^+, Mg^+) originating from meteoric sources (Schunk & Nagy, 2000).

1.1.2 F region

The F-layer is the region with the highest ionization. During the day it’s often divided in two layers F1 and F2. Like the E layer, the F1 layer is also dominated by photo-ionization with the difference that only O^+ ions can be found. The dynamics of this region can therefore be described with the continuity equation (13) and the ionization and recombination processes involving O^+ (1, 4-8). where (4 and 5) are negligible as in all of the F region.

For the F2 region the transport processes can’t be neglected anymore. Taking into account the momentum equation (15) the continuity equation takes the following form:

$$\frac{\partial n_i}{\partial t}+\nabla(n_i\vec{v}_i)=\pm\beta n_i-\alpha n_i^2+p_{flux} \tag{14}$$

$$\rho_i\frac{\partial\vec{v}_i}{\partial t}=-\nabla p_i+\rho_i\vec{g}+n_i q_i(\vec{E}+\vec{v}_i\times\vec{B})-\rho_i\mu_{ic}(\vec{v}_i-\vec{v}_n) \tag{15}$$

Where $\vec{v}_i$ is the ion velocity and $\vec{v}_n$ the velocity induced by the neutral winds. The transport process due to the winds is dominated by the friction, guided by the collision frequency μ_{in} and the drift along the magnetic field lines $\vec{B}$. The inclination of the magnetic field lines plays a major role in the transport processes of the F2 region. Due to the absence of vertical winds on a global scale , the coupling between the neutral atmosphere and the plasma is amplified at the geomagnetic equator where the magnetic field lines are horizontal. This effect causes the equatorial fountain and consequently the equatorial anomaly.

1.1.3 D region

The D region is the lowest part of the ionosphere between 60 to 100 km of altitude. It’s the only region of the ionosphere where negative ions can be found. The recombination rate is high due to the air density and therefore the incident radiation declines. Collision frequency of electrons and other particles is very high though which leads to High Frequency radio waves suffering a loss of energy which causes their attenuation and decrease of intensity.

1.1.4 Nighttime

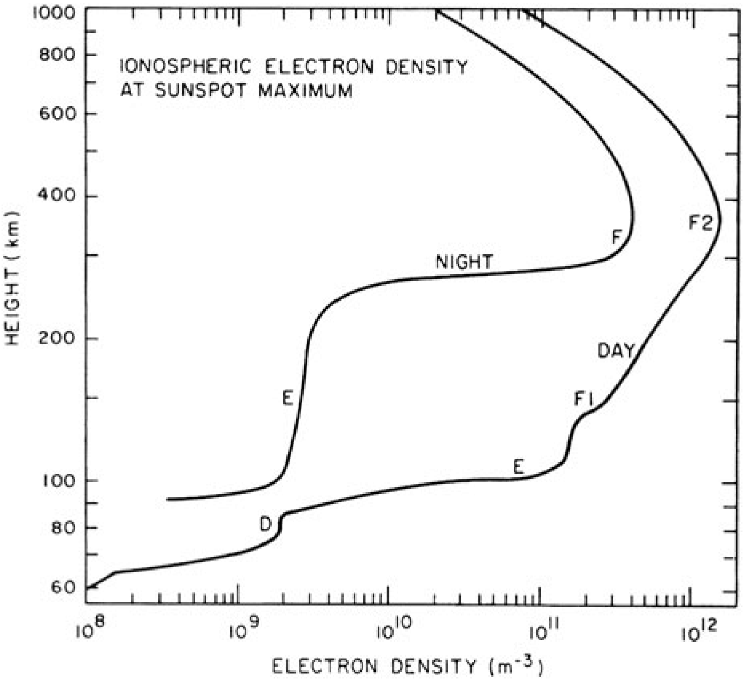

Figure 4: Idealized electron density distribution in the ionosphere during day and night. From: Evans & Hagfors (1968)

During the night the ionization of the ionospheric layers, particularly the F region diminishes by a factor of ten due to the absence of photo-ionization. The ionization rate in the E region is maintained by stellar radiation and the resonance of the solar radiation (Schunk & Nagy (2009)). The ionization of the F region during the night is due to ions descending from the plasmasphere and close to the equator ascending ions from the E regions pushed by a transport phenomenon of the meridional winds. Figure 4 shows an idealized electron density profile during day and night.

1.2 Ionospheric Variations and Anomalies

The ionosphere is a very dynamic medium. As mentioned before Sun radiation is the main source of ionization and therefore introduces periodical variations in the ionosphere related to the time of the day or season. But there are also other non-periodical but reoccurring variations or anomalies of the ionosphere. Some of the phenomena will be explained below.

1.2.1 Diurnal Variations

As explained above the ionosphere varies between day and night. Figure 2 and 4 show the differences between the ionosphere during the day and during the night. These diurnal variation are due to the rotation of the Earth. After sunrise the electron density starts to increase due to photo-ionization and continues to rise during the day until it starts decaying after sunset when the Sun as source for the photo-ionization disappears. Figure 5 shows the daily variations of the global total electron content (TEC). TEC describes the integral of the electron density along a path from the ground station to the satellite. The TEC is usually visualized as global or regional two-dimensional maps showing the state of the ionosphere (Manucci et al., 1998). Figure 5 also shows that the ionization is lower at higher latitudes as due to the zenith angle of the Earth the amount of sun radiation is smaller at higher latitudes. Another effect nicely visible is the equatorial anomaly near the geomagnetic equator. This is a trough in the ionization of the F_2 layer and spans about 17 degrees in geomagnetic latitude. The magnetic field lines are horizontal at the geomagnetic equator. Solar heating and tidal oscillations in the lower ionosphere move plasma up and across the magnetic field lines. This sets up an electric current in the E region which interacts with the horizontal magnetic field and forces ionization up into the F layer. This is also known as the equatorial fountain. The TEC is also measurable by radar altimeters; in this case the signal is propagating vertically from the satellite to the ocean surface and back to the satellite again. The linear combination of the two frequencies allows to estimate the TEC. Figure 6 shows the vertical TEC data from three orbits of the TOPEX altimetry satellite crossing the equator and where the equatorial anomaly can be clearly recognized.

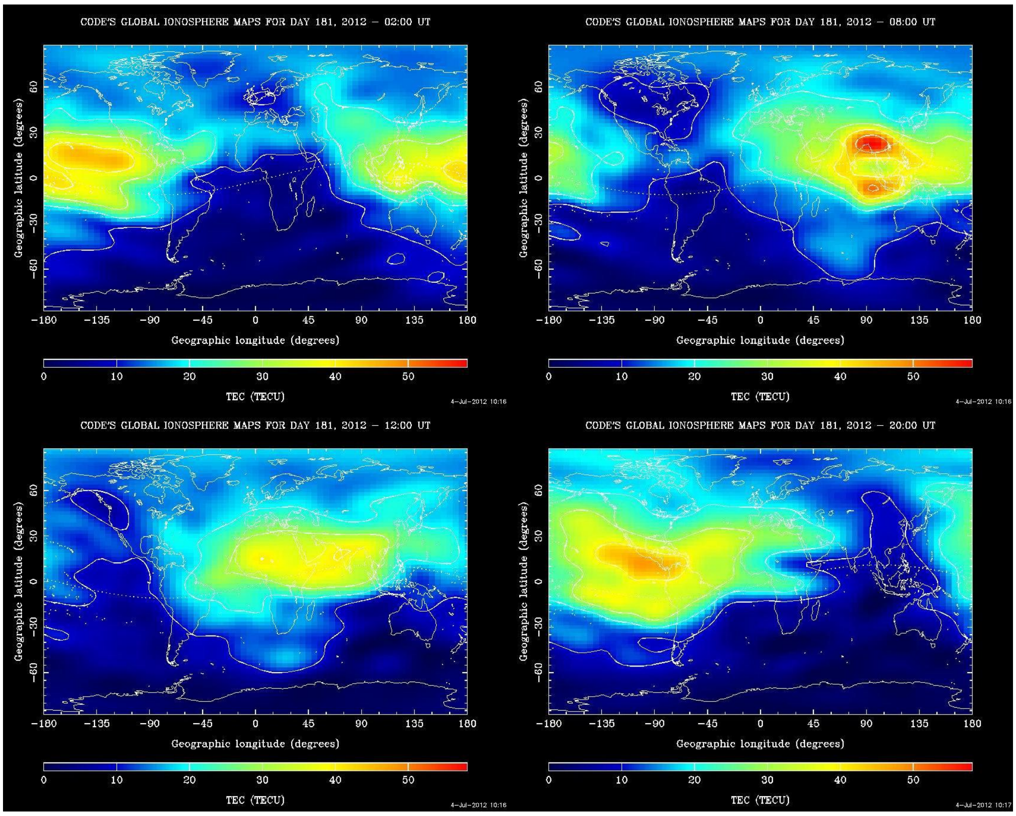

Figure 5: Global Total Electron Content (TEC) maps for day 181 (July 4) at 2 UT, 8 UT, 12 UT and 20 UT. This map was generated on a daily basis with data from about 200 GNSS stations from the University of Bern

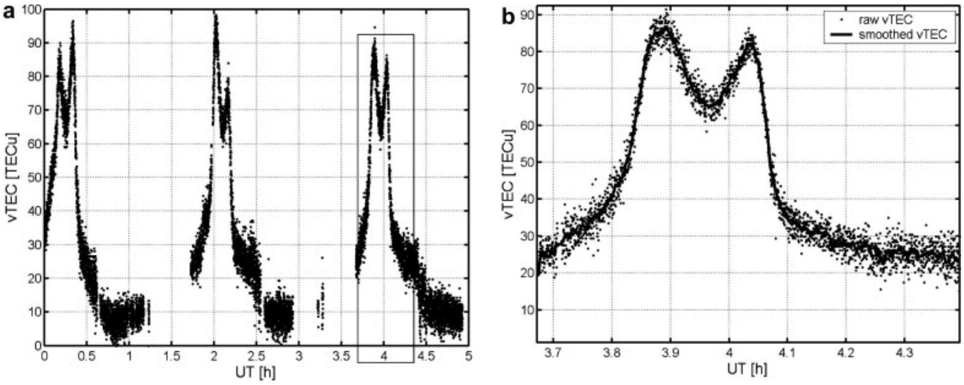

Figure 6: Equatorial anomaly shown by TEC measurements from three passings (left) of the TOPEX satellite over the geomagnetic equator and detailed view of the area inside the rectangle of the graphic on the left. From: Azpilicueta & Brunini (2008)

1.2.2 Seasonal Variations

As predicted by the Chapman theory explained earlier in this chapter, the solar zenith angle should influence the electron density in the ionosphere which means for seasonal variations the electron density should be higher in summer than in equinox and smallest in winter. However, studies have revealed features which differ from the prediction of the Chapman theory (e.g. Jakowski et al, 1981, Ma et al., 2003, Mayr & Mahajan, 1971, McNamara and Smith, 1982, Torr and Torr, 1973, Yonezawa, 1971, Yu et al., 2004, Yuen and Roelofs, 1967, Zeng et al., 2008, Zou et al., 2000, Bailey at al., 2000, Mendillo et al., 2005, Rishbeth, 1998, Rishbeth et al., 2000). Historically they were called anomalies when the behaviour of the ionosphere was different to the solar zenith angle dependence predicted by the Chapman theory. Typical anomalies in the F_2 layer electron density are: the so-called winter or seasonal anomaly which describes that the daytime values of the midlatitude peak of the F_2 layer, N_mF_2, are greater in winter than in summer; annual anomaly or nonseasonal anomaly when N_mF_2 for both hemispheres together in December is greater than in June in both daytime and night; semiannual anomaly, when the N_mF_2 at equinox is bigger than at solstice. Those anomalies are now explained with seasonal changes in atmospheric composition and dynamic processes (e.g. Bailey at al., 2000, Mendillo et al., 2005, Rishbeth, 1998, Rishbeth et al., 2000).

Kirby et al. (1934) was the first to discover the winter anomaly which has been followed by many studies of the ionospheric seasonal behaviour (e.g. Feichter & Leitinger (1997), Huang et al., 1989, Jakowski et al, 1981, Ma et al., 2003, Mayr & Mahajan, 1971, McNamara and Smith, 1982, Torr and Torr, 1973, Unnikrishnan et al., 2002, Yonezawa, 1971, Yu et al., 2004, Yuen and Roelofs, 1967, Zeng et al., 2008, Zou et al., 2000).

Torr and Torr (1973) showed that the winter anomaly is bigger at high solar activity than at low solar activity and that the differences between two solstices are bigger in the Northern Hemisphere than in the Southern Hemisphere. Mayr & Mahajan (1971) could find that during low solar activity N_mF_2 at low-latitudes is larger in summer than in winter and during high solar activity the semiannual effect is bigger at low latitudes whereas the winter anomaly prevails at midlatitudes. Feichter & Leitinger (1997) investigated TEC data to highlight that the semiannual anomaly is well developed during high solar activity, while the annual anomaly predominates during low solar activity during the whole day except a two hour period from 11 to 13 local time.

1.2.3 Solar Cycle

The solar cycle is a change in the Sun’s activity over a period of around 11 years. Levels of solar radiation and ejection of solar material, the number and size of sunspots and solar flares all show a synchronized fluctuation from active to quiet to active again within a period of 11 years. The ionospheric behaviour is controlled by the solar output and therefore the ionospheric variability follows a synchronous variation with the solar activity. Figure 7 shows the dependence of the monthly smoothed TEC on the number of sunspots and therefore on the solar cycle.

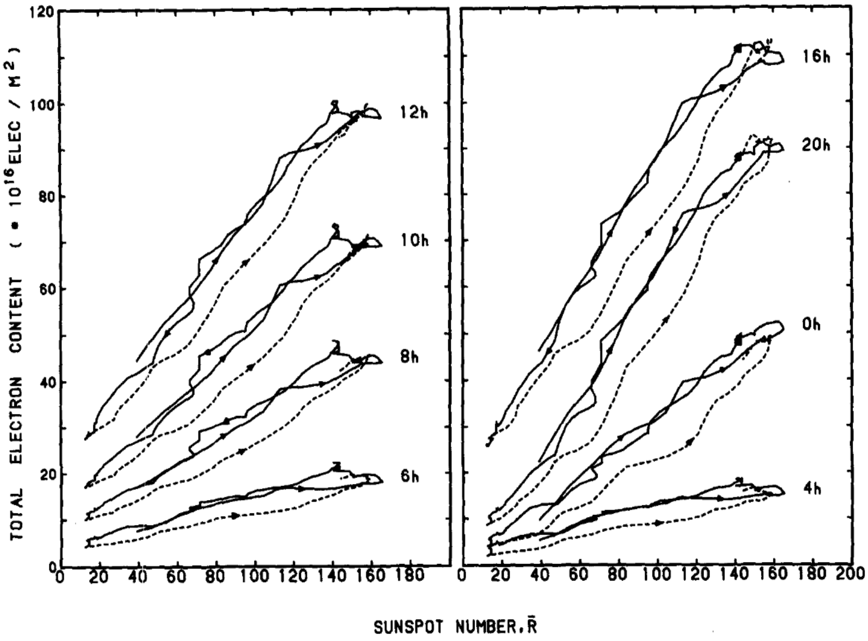

Figure 7: Variations of smoothed monthly mean TEC compared to smoothed sunspot number at different local times as indicated. Solid lines represent solar cylce 21 and dashed ones solar cycle 22. The arrows indicate the progression of the solar cycle. From: Huang & Cheng (1994)

1.2.4 Plasma bubbles

Plasma bubbles are irregularities in the equatorial region. They result from a higher recombination rate in the lower ionosphere after sunset which leads to a smaller plasma density compared to higher altitudes. This layer of lower plasma density can rise due to convection which creates the plasma bubble. They affect radio waves by causing varying delays and also degrade the performance of GPS. A plasma bubble is thought to have affected a battle during the US invasion in Afghanistan in 2002 when radio communication failed and a helicopter landed on a peak under enemy control (Kelly et al., 2014). Figure 8 shows a schematic view of the effect of plasma bubbles on satellite communication.

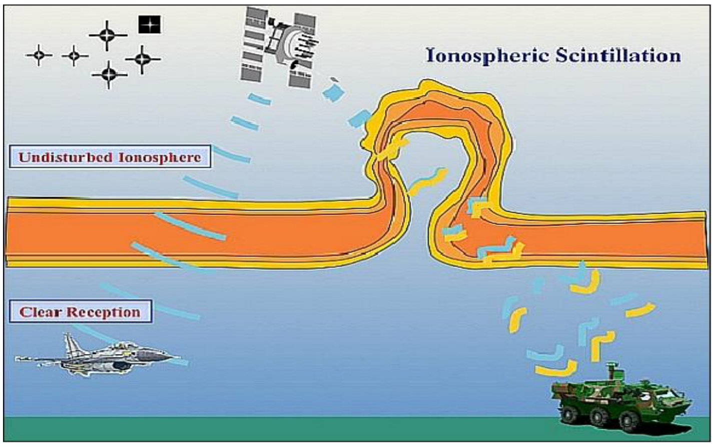

Figure 8: Schematic cartoon showing the influence of plasma bubbles on radio communication

1.2.5 Geomagnetic storms

The ionospheric response to geomagnetic storms, which are often called ionospheric storms, is one of the most complex subjects in the atmospheric coupling system. The storm-time ionospheric behaviour is controlled by several dynamic and electro-dynamic drivers. The changes in the ionospheric plasma density can be positive or negative compared to the undisturbed background ionosphere. A geomagnetic storm normally begins with solar/interplanetary plasma arriving at high speed at the magnetopause. This starts the interaction with the Earth’s magnetic field and leads to solar wind energy in the magnetosphere (Gonzalez et al., 1994). The storm-time neutral winds can alter the F region electron density peak height by pushing ions and electrons up and down along magnetic field lines (e.g. Goncharenko et al., 2007, Lu et al., 2008, Paznukhov et al., 2009, Astafyeva et al., 2016). Thermospheric winds can also drive neutral meridional winds which generate an electric field that influences the ionosphere (Blanc & Richmond, 1980). This disturbances which kind of resembles a dynamo develops slowly over several hours and can last for several hours (Maruyama et al., 2005). Changes in the composition of the thermosphere during a geomagnetic storm can also lead to changes in the ion loss rate and through that influence the ionosphere (e.g. Prölss, 1976, Prölss, 1980, Fuller-Rowell et al., 1994, Crowley et al., 2006, Astafyeva et al., 2018).

Those are some of the main drivers of ionospheric disturbances during geomagnetic storms. However, the ionospheric response to each storm is determined by a unique, complex, non-linear and sometimes even chaotic interaction of drivers playing their roles at a particular time and in a specific location. This leads to big difficulties in the analysis of these storms ad also in forecasting and modeling of the ionospheric behaviour during geomagnetic storms (e.g. Borries et al., 2015, Huba et al., 2016, Astafyeva et al., 2017).

As mentioned before, a more exotic phenomenon affecting the ionosphere is the aurora borealis. During magnetic storms, which mainly happen while the solar activity is increased, the radiation emitted by the Sun interacts with the Earth’s magnetic field to create this phenomenon of rare beauty. The charged particles coming from the Sun and guided by the magnetic field lines focus in the polar regions where they generate a luminous activity visible for human eyes in the sky. It was discovered that, with the light emissions, the aurora generates also acoustic gravity waves that can be detected on the surface of the Earth (Wilson, 1969a; Wilson, 1969b). More recently, the studies of Wilson showed that the waves ignited by the pulsations of the aurora have frequencies higher than 30 mHz (Wilson, 2003; Wilson, 2005; Wilson et al., 2005). This is a good example of the coupling between the neutral atmosphere and the ionosphere.

1.3 Ionospheric sounding techniques

The ionosphere is a dispersive medium, thus the linear combination of observables on the two frequencies of signals traversing it is needed to remove this effect for positioning. On the other hand, the dispersive property provides an opportunity to measure directly the ionospheric electron content, as first published by Klobuchar (1985). The travel time of an electromagnetic wave through a medium with refractive index n is given as:

$$t_{travel} = \int_{raypath} \frac{1}{c_{medium}} d\vec{r} = \int_{raypath} \frac{n_{medium}}{c_{vacuum}} d\vec{r} \tag{16}$$

The phase refractive index as a function of the frequency is:

$$n^2 = 1 - \frac{\omega_p^2}{\omega^2} \tag{17}$$

Where ω_p is the plasma frequency

$$\omega_p^2 = \frac{Ne^2}{\varepsilon_0 m_e} \tag{18}$$

The refractive index is real and smaller than 1 for $\omega > \omega_p$, thus causing the wave to travel slower than in the vacuum. We can expand n in a binomial series that is convergent while $\left|\frac{\omega_p^2}{2\omega^2}\right| < 1$. For a typical value of the electron density in the F-layer of the ionosphere of $N = 5*10^{11} m^{-3}$ and the two GPS frequencies f_1 and f_2 the values of $\left|\frac{\omega_p^2}{2\omega^2}\right|$ are $1.62*10^{-5}$ and $2.67*10^{-5}$ respectively. We expand formula (17) and retain terms up to first order:

$$n = 1 - \frac{\omega_p^2}{2\omega^2} \tag{19}$$

Substituting ω_p gives:

$$n = 1 - \frac{Ne^2}{2\varepsilon_0 m_e \omega^2} = 1 - \frac{Ne^2}{8\pi^2 \varepsilon_0 m_e f^2} \tag{20}$$

with $A = \frac{e^2}{8\pi^2 \varepsilon_0 m_e} \approx 40.3 \frac{m^3}{s^2}$, so that

$$t_{travel} = \frac{1}{c} \int_{raypath} 1 - \frac{A}{f^2} N(\vec{r}) d\vec{r} \tag{21}$$

The ionospheric phase delay relative to wave propagation in a vacuum is:

$$I_{Phase} = t_{travel}^{medium} - t_{travel}^{vacuum} = \frac{-A}{f^2 c} \int_{raypath} N(\vec{r}) d\vec{r} \tag{22}$$

i.e. the phase is advanced (minus sign). Using the group refractive index with (19) it follows that:

$$n_G = 1 + \frac{\omega_p^2}{2\omega^2} \tag{23}$$

The wave group is delayed by:

$$I_{Group} = t_{travel}^{medium} - t_{travel}^{vacuum} = \frac{A}{f^2 c} \int_{raypath} N(\vec{r}) d\vec{r} \tag{24}$$

The group delay is thus equal to the phase advance.

The phase of the GPS carrier wave is advanced by the same amount of time that the information in a wave group is delayed. The latter integral in (22) and (24) is simply the electron density integrated along the raypath from satellite to receiver and is called total electron content.

1.4 Ionospheric models

As described in Chapter 1.2 the ionosphere is very dynamic and constantly changing. This makes it challenging to accurately model its behaviour. Currently more than 170 ionospheric models are in use (Schunk, 2013) and discussed in an overview (AIAA, 1999). These models differ by their degree of complexity, calculation time and their purpose. They are used for different purposes including scientific and applications such as the correction of the ionospheric effects on Global Navigation Satellite Systems (GNSS). The models are often classified into empirical, physics-based numerical, parametrized and data assimilation models. We will give a short overview over the models used in this work, the Global Ionospheric Maps (GIM), the International Reference Ionosphere (IRI) and NeQuick. The latter are two of the most popular empirical models. A comparison of NeQuick and IRI is shown in Figure 9. Empirical models are based on measurements collected over an extended period of time using in situ remote methods. The data consists of easily measured parameters of each ionospheric layer such as critical frequencies (f_0E, f_0F_1, f_0F_2), peak heights (h_mE, h_mF_1, h_mF_2) and half-thicknesses (y_mE, y_mF_1, y_mF_2). Critical frequency being the limiting frequency at or below which a wave component is reflected by, and above which it penetrates through, the corresponding ionospheric layer. The peak height describes the altitude of the density peak where the level of loss and diffusion of the ions are of comparable importance. The term half- or semi-thickness dates back to the 1940s. Based on an assumed parabolic shape of the ionospheric layer, a set of templates was used to find the best alignment with the height of the maximum electron density for the layer. The parabolic curve with the best fit was numbered with the half-thickness of the parabola. Subsequently the collected data is averaged and fitted to simple analytical expressions or orthogonal polynomials in order to construct an electron density profile.

1.4.1 The International Reference Ionosphere

The International Reference Ionosphere (IRI) is one of the standard empirical models providing TEC data. IRI is an ISO (International Standardisation

Organisation) project of the Committee on Space Research (COSPAR) and International Union of Radio Sciences (URSI).

IRI has been steadily improved over the years using updated data and better modeling techniques. Nowadays a working group of 58 experts is in charge of developing and improving the model. A detailed list of improvements provided since its inception can be found in Bilitza et al. (2017). For a given location, time, date and solar activity, IRI provides monthly averages of electron density and temperature, ion temperature and ion composition, in an altitude range from about 60 km to about 2000 km. Thus IRI can describe monthly varying electron densities but no day-to-day variability that requires real-time data and updates or assimilation technique combining IRI with data. This is also discussed in Bilitza et al. (2017).

To obtain the electron density with IRI, the vertical profile is divided into 7 subsections: the D region, the E-bottomside, the E-valley, the intermediate region between E and F1 layer, the F1 layer, the F2 bottomside and F2 topside (Bilitza, 1990). IRI provides three topside electron density profile options (IRI-NeQuick, IRI-Corr, IRI-2001) and three bottom-side thickness options (Bil-2000, Gul-1987, ABT-2009) to control TEC and the electron density profile (Coisson et al., 2008). The upper side electron density profile options are expressed using numerical functions. IRI-2001 contains constant gradients based on the approach of Skelton profile (Booker, 1977). The IRI-NeQuick is given by semi Epstein layer function (Coisson et al., 2006). The topside electron density profiles decrease exponentially with altitude for these options although the decrease for IRI-NeQuick and IRI-Corr is more rapid than for IRI-2001 (Bilitza, 2001). The topside and the bottom side of the electron density profiles are normalized to the F2 peak density and heights. Starting from the 2012 version (IRI-2012) the model is also able to describe storm effects in the auroral E-region and includes auroral boundaries that allow a better representation of density and temperature features at these boundaries (Bilitza et al., 2014).

Empirical models such as IRI rely on solar indices involving daily and seasonal variations as well as the impact of solar activity on ionospheric conditions. In general, these solar indices are the sunspot number R (number of dark spots on the solar disc) and the solar radio flux at 10.7 cm wavelength (F10.7). Both can be observed from the ground and long data records exist.

1.4.2 NeQuick model

The ‘quick calculation model’ NeQuick (Radicella & Leitinger, 2001) is an empirical model as it is based on a model introduced by Di Giovanni & Radicella (1990) taking into account the physical properties of the ionospheric layers. It has been developed by the International Centre for Theoretical Physics (ICTP) in Trieste, Italy, in collaboration with the University of Graz in Austria. NeQuick is a three-dimensional and time-dependent ionospheric model, which provides electron densities in the ionosphere as a function of position and time. The new version NeQuick2 (Nava et al., 2008) allows to compute directly the slant TEC for a given starting and ending point. The input parameters of this model are the position (longitude, latitude, altitude), the period (month and UT) and the solar activity (given by monthly mean sunspot number R_{12} or 10.7 cm solar radio flux). The electron density distribution is reproduced analytically up to the F2 layer peak using five semi-Epstein layers. The model uses the peaks of the E, F1 and F2 layers as anchor points modeled from the ionosonde parameters (f_0E, f_0F_1, f_0F_2). However, the critical frequency of the F_2 layer, f_0F_2, is modeled by the Comité Consultatif International pour la Radio (CCIR) maps; the critical frequency for the E layer, f_0E, is a formulation modified by John Titheridge; and the critical frequency for the F_1 layer, f_0F_1, is assumed to be proportional to f_0E in daytime and 0 during night (Leitinger et al., 2005). The topside is represented by another semi-Epstein layer, calculated from the altitude and an empirical thickness parameter.

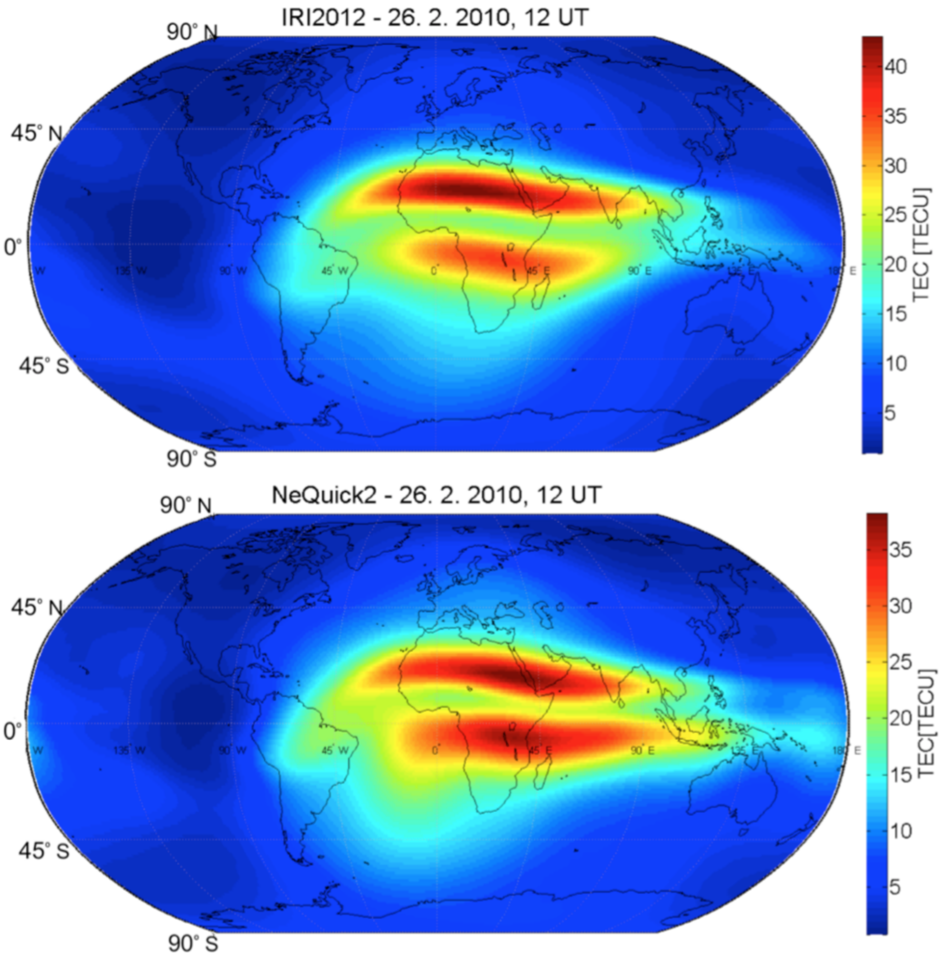

Figure 9: Global ionospheric TEC maps for 26th February at 12 UT modeled by the empirical models NeQuick and IRI. Although they are different in the way they model the ionosphere both distinguish the equatorial anomaly. From: Najman and Kos (2014)

As for the IRI model, several efforts have been made to improve the analytical formulation of the NeQuick model. Leitinger et al. (2005) improved the bottom side description of the model and Coisson et al. (2006) made major changes in the topside formulation leading to NeQuick 2 (Nava et al., 2008) that is now adopted by ITU-R recommendation. The NeQuick model is also used to correct the ionospheric delay for the Galileo satellite system (Arbesser-Rastburg, 2006).

1.4.3 Global Ionospheric Maps

Global Ionospheric Maps (GIM) are maps of vertical TEC on a global scale in a 2.5° x 5° grid in latitude and longitude respectively. The time resolution is, depending on the processing center, one or two hours between separate maps. Since the late 1990s, Jet Propulsion Laboratory (JPL), Center for Orbit Determination in Europe (CODE), Universitat Politecnica de Catalunya (UPC) and ESA's European Space Operations Center have established a supply of global ionospheric models and TEC GIMs on a daily basis (Manucci et al. (1998), Schaer (1999), Hernandez-Pajares et al. (1999), Hernandez-Pajares et al. (2009)). Final TEC GIMs in the IONEX (Ionosphere Map Exchange) format are provided by the International GNSS Service (IGS) by combining the results of several GIMs from several processing centers with corresponding weights (Hernandez-Pajares et al. (2009)). The processing centers that produce GIMs use different methods, e.g. spherical harmonics, generalized trigonometric series, a three-shell model, an inversion of the data or a combination of several of those methods.

To evaluate the accuracy of the GIMs Ho et al. (1996) compared them to TEC data from TOPEX/Poseidon altimetry satellite measurements and found good agreement between both. Orus et al. (2002) did a comparison of GIMS with IRI and the Bent model (Bent & Llewllyn, 1973) and concluded that the performance is better than the other models. Hernandez-Pajares et al. (2009) did another comparison with altimeter vTEC measurements to fully validate the reliability of GIMs. More recently Chen et al. (2019) performed a statistical analysis of the results of the different processing centers to compare the difference induced by the various computing methods and also the amount of data used which lies between 200 and 500 GNSS stations, depending on the processing center.

Figure 9 shows four GIMs over one day from the University of Bern using data from about 200 GNSS stations and spherical harmonics to retrieve the global TEC distribution.

The disadvantage of the use of GIMs is the spatial and time resolution which requires interpolation and makes the modeling of TEC data for single station-satellite pairs more challenging.

1.5 Ionospheric Seismology

One of the objectives of this manuscript is to explore the effect of natural hazards in the ionosphere. The work mainly focuses on the modification induced in the ionosphere by solar eclipses (fully detailed in Chapter 2) and to the recent theory exploring the possibility to predict Earthquakes observing a perturbation in the ionosphere before the seismic event (fully detailed in Chapter 3). As the ionospheric dynamics are mainly driven by the Sun's radiation, it's naturally understandable that the ionosphere is affected by solar eclipses; on the other hand, the relation between the seismic activity and the ionosphere is less trivial. Consequently this section is dedicated to the introduction and understanding of this relation, the so called Ionospheric Seismology. This new scientific area is recent (last 20 years) but can find his origin back in the ancient greek history.

In the Meteorologia (524) Aristotle suggests that winds heated by the Sun are, after falling to the Earth, causing a strong pressure variation inside the cavities of the Earth resulting in an earthquake. This simplistic vision of Aristotle - considering the planet as a unique body where the fluid and the solid part exchange energy - was unfortunately forgotten in modern seismology (R. Mallet created the term seismology in 1850). Seismology finds its origins partly in the application of the elasticity theory to the Earth and in the development of seismometers. In this context, seismology evolves as the physic of the solid Earth, neglecting the atmosphere. Since some decades, and thanks to new technologies, this theory has been extended to the whole system: the solid Earth, the ocean, the atmosphere and even the ionosphere. Remote sensing of earthquakes and tsunamis proved that the vibrations produced by the seismic events are also detectable in the fluid envelopes: nominally the atmosphere and the ionosphere. Figure 10 shows a schematic overview of the coupling mechanism and the ionospheric sounding techniques resuming what we call today ionospheric seismology.

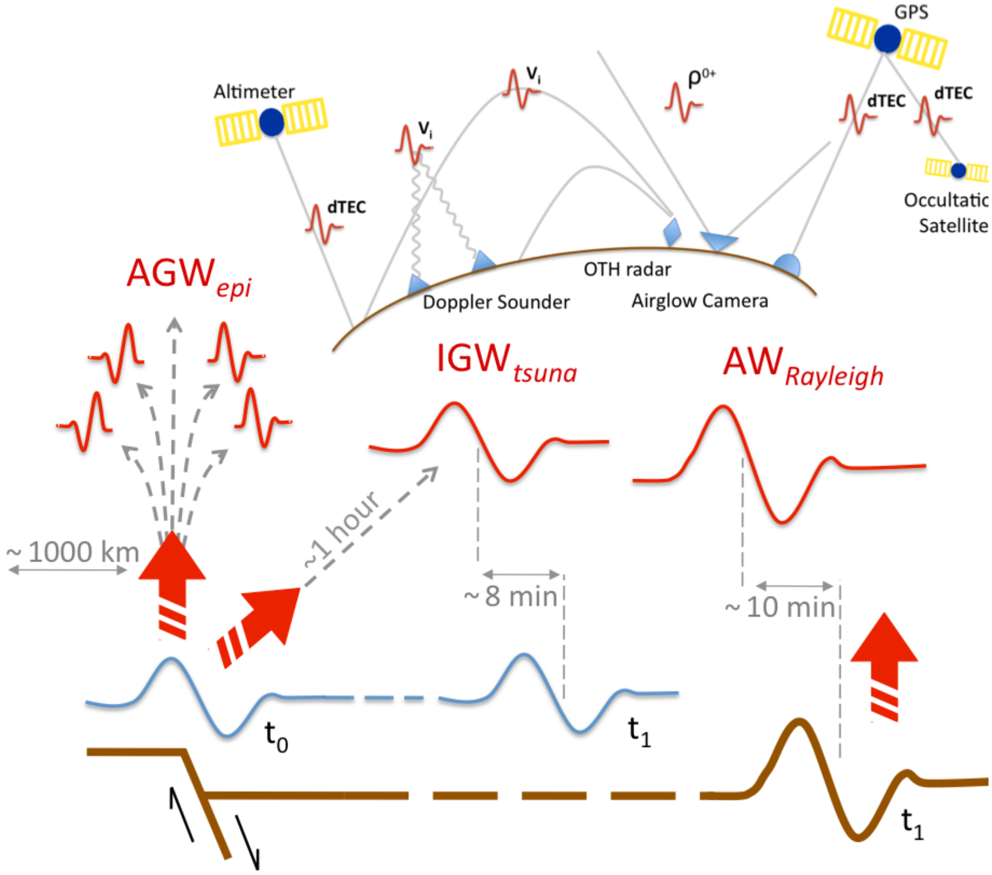

Figure 10: Schematic view of the coupling mechanism (bottom) and the ionospheric sounding technique (top). Ground and ocean displacement at the source produces AGW$_{epi}$ that are observable in the ionosphere ~8 minutes after the rupture and observable until ~1000 km from the epicenter. The oceanic displacement initiates the tsunami that, during its propagation, creates IGW$_{tsuna}$ that reach the ionosphere in ~1 hour and keeps a delay of ~8* minutes compared to the tsunami at the sea surface. At teleseismic distance, the Rayleigh wave induced AW$_{Rayleigh}$ propagating vertically to the ionosphere in ~10 minutes. Times marked (*) are computed for a tsunami with a main period of 10 minutes. Ionospheric sounding techniques (observable): Doppler sounder and OTH radar (vertical ion velocity): Altimeter and GPS (perturbation of the TEC), airglow (O^+ density perturbation). From: Occhipinti (2015)*

This quick introduction mentioned that the first ideas of a coupling between Earth and atmosphere appeared very early in history of science but it wasn’t until the 1960s that, thanks to technical developments, the first observations supported it. During the Cold War the only way to control the nuclear tests were seismometers and atmospheric sensors. The first monitors the Earth, the second the atmosphere; they were used for the localization and to calculate the intensity of the explosion. Those continuous observations produced numerous theoretical and observational results on the propagation of acoustic gravity waves generated by an explosion (Yamamoto, 1956; Yamamoto, 1957; Weston, 1962; Harkrider, 1964; van Hulsteyn, 1965). The observed wave doesn’t seem trapped in the troposphere: its effect has been observed in the ionospheric plasma (Rose et al., 1961; Beynon & Jones, 1962; Dieminger & Kohl, 1962; Saha et al., 1963; Webb & Daniels, 1964). For more details about the structure of the ionosphere see Chapter 1.1. This combination between seismic and atmospheric receivers for the nuclear tests helped to proof the propagation of acoustic-gravity waves generated by earthquakes and similar to those observed in the case of nuclear explosions. It was in 1964 after the earthquake in Alaska (M_w=9.2), the second biggest after the one in Chile in 1960, when the barometer in Berkeley registered two abnormal signals (Bolt, 1964). The first of faint intensity, correlating well with the seismic signals, was the effect of the Rayleigh wave which propagated on the surface of the Earth from the epicenter. The same signal recorded at Papete (Polynesia) allowed to calculate the seismic moment using the mantle magnitude (Okal & Talandier, 1989) with an error of only 0.1 % of the value of M_m=9.91 from Kanamori (1977) and reveals the usefulness of atmospheric detections in the estimation of major earthquakes (Okal & Talandier, 1991). The second signal observed by Bolt (1964) showed an intensity three times bigger than the first and it was described as the seismic air wave. This signal represents, as for the nuclear explosions, the acoustic-gravity wave generated by the vertical displacement at the source, which after creation propagates through the atmosphere where it’s detectable at great distance (AGW_{epi}).

Other publications followed Bolts observations to explain the perturbations generated by the earthquake in Alaska, both for the neutral atmosphere (Donn & Posmentier, 1964) as well as for the ionosphere (Davies & Baker, 1965; Leonard & Barnes, 1965; Row, 1966).

The studies on nuclear explosions have laid the foundation for the observation of post-seismic wave phenomena that took place in the neutral atmosphere and ionosphere. More precisely, the monitoring of the ionosphere allowed to observe the properties of acoustic-gravity waves, their dispersion and attenuation and it confirms the theoretical hypotheses developed earlier (Hines, 1960; Press & Harkrider, 1962; Pitteway & Hines, 1963). The work of Row (1966) summarizes nicely the similarity between those two types of sources: by using a point source described with Green functions, Row (1966) models the propagation of an acoustic-gravity wave in an isothermic atmosphere and is able to generate - with the same method - the atmospheric perturbation induced by the earthquake in Alaska as well as the one induced by the nuclear explosion of October 30th 1961. The resulting model seems to be coherent with the observations using a Doppler sonde by Davis & Baker (1965) and the variations of the f_0F_2 (plasma frequency of the maximum ionization) index presented by Stoffregen (1962).

The Alaskan earthquake brought the attention of Seismology towards the atmosphere and opened the door for the Ionospheric Seismology.

1.5.1 Early observations - mainly by Doppler sounders

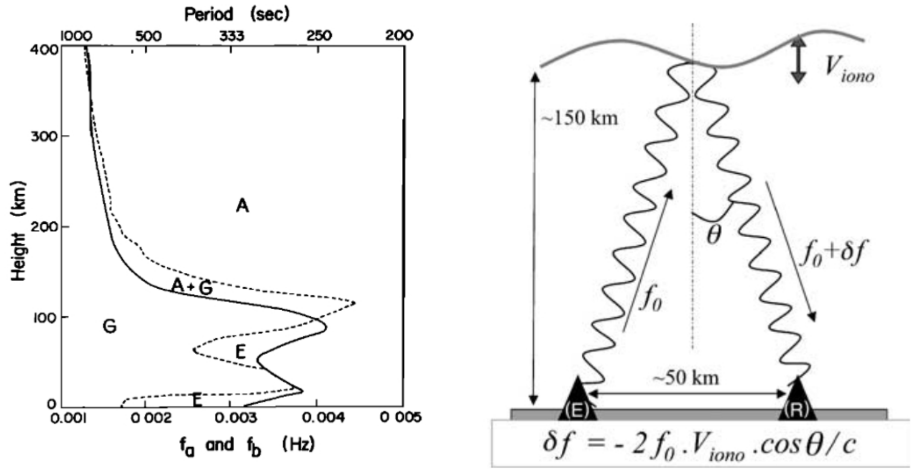

Figure 11: Left: theoretical discrimination of the acoustic (A), acoustic-gravity (A+G), gravity (G) and evanescent (E) domain. Dashed line represents the Brunt-Väisälä (From: Najita & Yuen (1979)). Right: principle of a doppler sounder. The displacement speed of the ionospheric reflexion layer is observed as a delay δf between the emission frequency and the signal that is received again. From: Artru et al. (2004)

The technical development of the following years allowed to enlarge the detections of post-seismic ionospheric perturbations of earthquakes with moderate magnitudes: the earthquakes of Tokachi-Oki in 1968 and of the Kuril Islands in 1969 with a magnitude of 7.5 and 7.9 respectively (Najita & Yuen, 1979).

Different to earlier studies, Najita & Yuen (1979) focus on the acoustic wave generated at the soil-atmosphere boundary by the passing of the Rayleigh wave ($AW_{Rayleigh}$). After a theoretical analysis of the waves propagating in the ionosphere (Figure 11), which confirms that the waves generated by the displacement of the soil ($AW_{Rayleigh}$) are only acoustic waves, Najita & Yuen (1979) calculate the travel time of the vertical propagation of the acoustic wave as a function of the period of the Rayleigh wave (Figure 11). This allowed to deduct the arrival time of the Rayleigh wave from the Doppler data for the two earthquakes and to reproduce the dispersion curve shown in Figure 12.

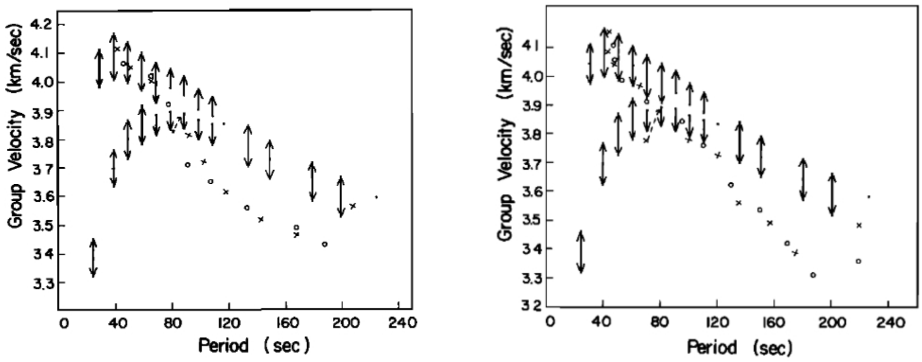

Figure 12: group speed of oceanic Rayleigh waves measured by Doppler sondes after the Tokachi-Oki (left) and Kuril Islands (right) earthquakes. The circles represent the speed and the crosses the displacement. The arrows describe the curve of Olivier (1962) obtained with seismic data. From: Najita & Yuen (1979)

The dispersion curve of Rayleigh waves estimated by Doppler sounder is coherent with the curve of Olivier (1962) which was obtained with seismic measurements. This result shows the evidence of the coupling between the solid Earth with the atmosphere and the ionospheric plasma.

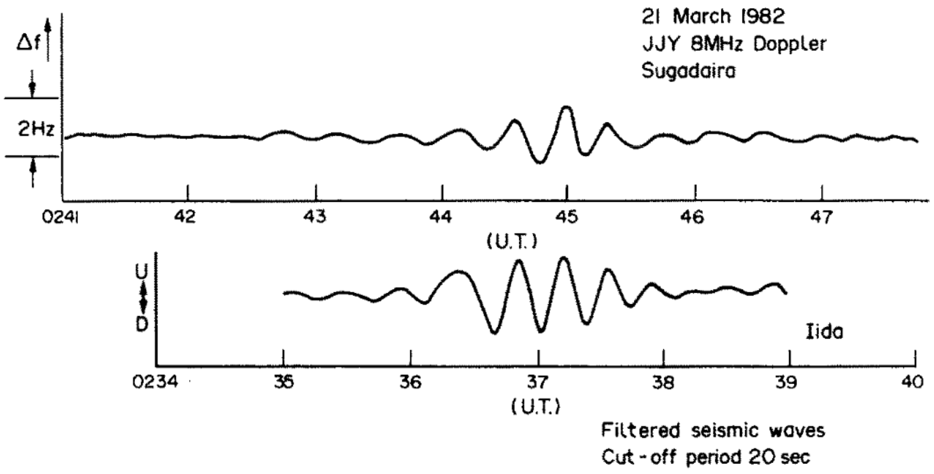

Figure 13: Doppler data measured at Sugadaira and vertical displacement at he seismic station of Ida. Both signals are filtered between 10 and 20 s. From: Tanaka et al. (1984)

We can resume that information about the oceanic crust can be obtained sounding the ionosphere at 175 and 300 km of altitude. A few years later Tanaka et al. (1984) followed the same approach to analyze the earthquake of Urakawa-Oki on 21 March 1982 with a magnitude 7.1. With the help of the Japanese network of Doppler sounders (Sendai, Tokyo, Sugadaira and Kyoto) which are all within 1000 km of the epicenter, they measured a propagation speed of 3.5 km/s for the Rayleigh waves; which was strongly coherent to the value of 3.6 km/s obtained by seismic stations (Akita, Iida, Abuyama). There is a strong similarity in the signals of both Doppler and seismic data filtered between 10 and 20 seconds (Figure 13). This confirms the phenomenon of the coupling driven forward by Najita & Yuen (1979). Additionally the frequency analysis of the three types of signals (seismic, Doppler at 5 M/Hz and Doppler at 8 MHz) clearly shows the atmospheric damping of high frequencies due to the viscous effect. This is in line with the predictions by Pitteway & Hines (1963) and confirms that only Rayleigh waves propagate vertically in the atmosphere as acoustic waves ($AW_{Rayleigh}$) with periods of approximately 20 seconds (Figure 14).

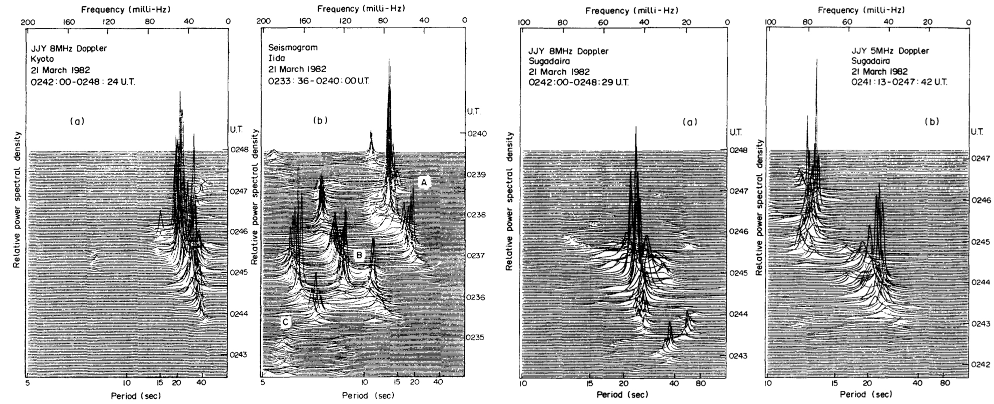

Figure 14: From left to right: Spectra of signals from Doppler sounders at 8 MHz registered at Kyoto, seismic signal registered at Ida and the Doppler signals of 5 MHz and 8 MHz registered at Sugadaira. From: Tanaka et al. (1984)

Although the stations were close to the epicenter, Tanaka et al. (1984) can't observe any acoustic-gravity wave created at the source (AGW_{epi}). The debate concerning the acoustic wave forced by the Rayleigh wave ($AW_{Rayleigh}$) and the acoustic-gravity wave generated at the source (AGW_{epi}) - propagating horizontally in the atmosphere - was ongoing for a long time with several newer articles supporting the second hypothesis (e.g. Heki & Ping, 2005). The Doppler sounding has been renewed with new sounders offering better performance and allowed to detect earthquakes with magnitudes as low as 6.8 (Artru et al., 2004).

Additionally, Occhipinti et al. (2010) clearly proved that over-the-horizon (OTH) radars are also able to detect the ionospheric signature of Rayleigh waves ($AW_{Rayleigh}$) with the same sensitivity as Doppler sounders (Figure 16). Coupling together Doppler sounders, OTH radars and seismometers Occhipinti et al. (2018) successfully estimated the magnitude and the dispersion curve of Rayleigh waves from seismic data and ionospheric data using 38 seismic events (Figure 47). Introducing the Ionospheric Magnitude authors proved that ionospheric monitoring is valuable and a trustable seismological observation as well as seismometers.

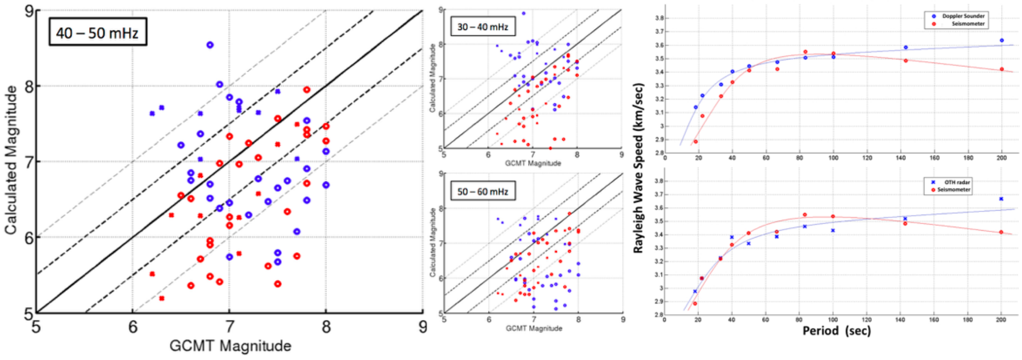

Figure 15: Left: Discrepancies between the official surface wave magnitude estimated by the GCMT and the surface wave magnitude measured with a single seismometer (red cross and red circle), Doppler sounder (blue circle) and OTH radar (blue cross). The different plots show different frequency ranges used to filter the data for the magnitude computation. Right: Rayleigh wave dispersion curve computed using 28 seismic events (top) observed by Doppler sounder (blue circle) and seismometer (red circle) and 10 events (bottom) observed by OTH radar (blue cross) and seismometer (red cross). From: Occhipinti et al. (2018)

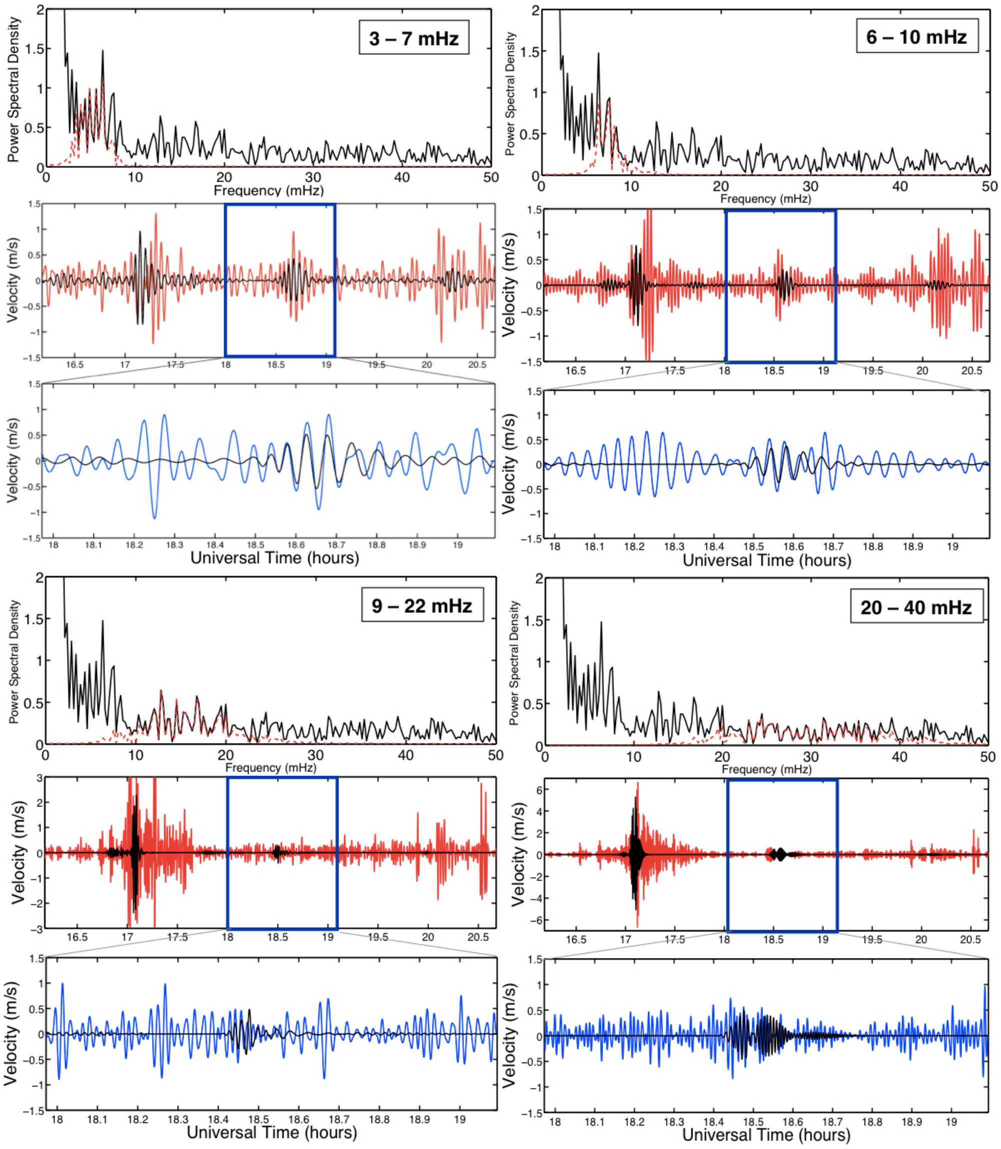

Figure 16: Spectral analysis of the AGW$_{Rayleigh}$ detected by Doppler sounder and OTH radar after the Sumatra event (28 April 2005, M$_w$ 8.1) In each triptych (three plots for each highlighted bandpass range): top, spectrum of the Doppler sounder raw-data. Middle, Doppler sounder filtered data (red) and modeling (black), showing clearly R1 and R2, and sometimes a clear signature of R3. Bottom, OTH radar filtered data (blue) and modeling (black) showing only R2 (the timescale corresponds to the blue square in the middle plot). The R1 AW$_{Rayleigh}$ in the Doppler sounder is still recognizable independent of the frequency range; the signature of R2 AW$_{Rayliegh}$ for that after 10 mHz. From: Occhipinti et al. (2010)

1.5.2 Modern Ionospheric Seismology – mainly by GNSS-TEC

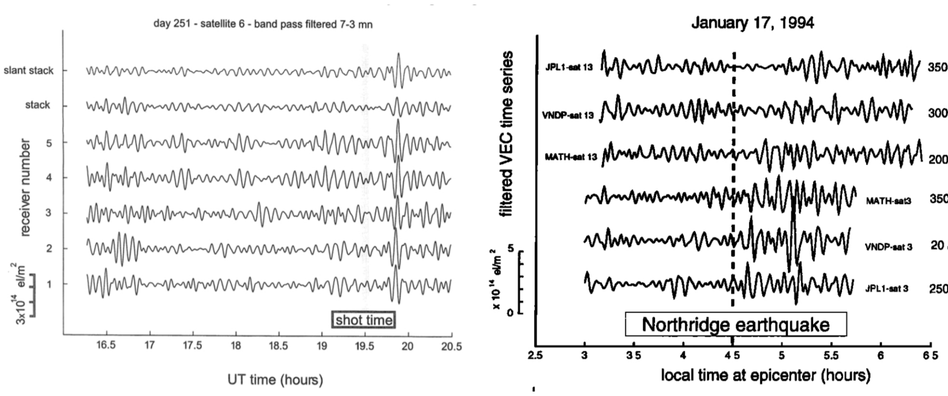

Figure 17: TEC perturbation registered after an explosion of 1.5 kt in a mine in Wyoming (left) and after the earthquake of Northridge (right) for the first case the receivers are all at the same distance to the explosion, for the earthquake they are sorted according to their epicentral distance. From: Calais & Minster (1995) & Calais et al. (1998)

The introduction of the Global Positioning System (GPS) in 1980 seemed to have the potential to revolutionize Geodesy. Therefore thanks to Manucci et al. (1993) who introduced the measurement of the total electron content (TEC) by GPS, meaning the amount of electrons along the station-satellite path, research on the physics of the ionosphere also made great progress. The first works showed the capability of GPS to observe variations in electron density after natural or artificial events: three explosions of 1.5 kt each in the Black Thunder mine in eastern Wyoming (Calais et al., 1998), the launch of Space Shuttle STS-58 (Calais & Minster, 1996) and the earthquake of magnitude 6.7 in Northridge, California, on January 17 1994 (Calais & Minster, 1995, Figure 17).

Following Manucci et al. (1998) it became possible to image TEC on a global scale using GPS (Figure 5). Thanks to the large number of measurements due to dense networks like in the US or Japan with more than 1000 GPS receivers, the two dimensional propagation of post-seismic perturbations could be imaged for the first time (Ducic et al., 2003, Heki & Ping, 2005). Ducic et al., 2003 showed the ionospheric signature of the Rayleigh wave over California (Figure 18). The geometrical structure of the station-satellite pairs allows to calculate the propagation speed of the Rayleigh wave over the ocean at 500 km from the Californian coast. However, no analysis of the dispersion of Rayleigh waves was possible due to the integrated nature of the TEC measurement. The moving sub-ionospheric points as well as the intersection of the satellite-station path at the altitude of maximum ionization (290-300 km), doesn't make the frequency analysis of the Rayleigh wave easy.

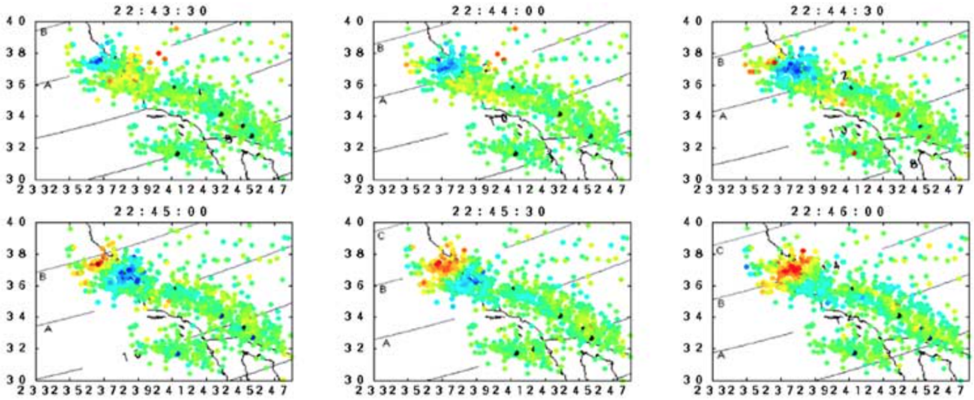

Figure 18: TEC perturbations generated by the passing of the Rayleigh wave induced by the Denali earthquake (3 November 2002, Alaska, M_w=7.9). The altitude of the points shown is supposed to be between 290 and 300 km positioned along the satellite-receiver path. Lines A, B and C indicate the propagation of a wavefront with 3.5 km/s. From: Ducic et al. (2003)

Although limited to earthquakes of greater magnitude than the ones detected using Doppler sounders, the enormous quantity of available data makes GPS the new revolutionary tool in the analysis of post-seismic perturbations, particularly in the near-field (Heki & Ping, 2005) and in order to estimate the source parameters (Afraimovich et al., 2005, Heki et al., 2006).

The giant tsunami following the Sumatra-Andaman event (M_w=9.3, 26 December 2004, Lay et al., 2005) provided worldwide remote sensing observations in the ionosphere, giving the opportunity to explore ionospheric tsunami detection with a vast dataset. In addition to seismic waves detected by global seismic networks (Park et al., 2005), co-seismic displacement measured by GPS (Vigny et al., 2005), oceanic sea-surface variations measured by altimetry (Smith et al., 2005), detection of magnetic anomaly (Iyemori et al., 2005; Balasis & Mandea, 2007), and acoustic-gravity waves (Le Pichon et al., 2005), a series of ionospheric disturbances, observed with different techniques, have been reported in literature (Occhipinti, 2015 and references therein). Two ionospheric anomalies in the plasma velocities were detected north of the epicenter by a Doppler sounding network in Taiwan (Liu et al., 2006a). The first was triggered by the vertical displacement induced by Rayleigh waves ($AW_{Rayleigh}$). The second, arriving one hour later with a longer period, is interpreted by Liu et al. (2006a) as the response of ionospheric plasma to the atmospheric gravity waves generated at the epicenter (AGW_{epi}). A similarly long period perturbation, with an amplitude of 4 TECU peak to peak, was observed by GPS stations located on the coast of India (DasGupta et al., 2006). These perturbations are interpreted by the authors as the ionospheric signature of internal gravity waves generated at sea level by the tsunami (IGW_{tsuna}) or the atmospheric-gravity waves generated at the epicenter (AGW_{epi}). Comparable TEC observations were done for five GPS stations (12 station-satellite pairs) scattered in the Indian Ocean (Liu et al., 2006b). The differential amplitudes are equal to or smaller than 0.4 TECU which generates amplitudes comparable to the observations of DasGupta et al. (2006) and arrival times coherent with the tsunami propagation. Occhipinti et al. (2006) use three-dimensional modelling to compute the atmospheric IGW_{tsuna} generated by the Sumatra tsunami and their interaction with the ionospheric plasma. This quantitative approach reproduces the TEC observed by Topex/Poseidon and Jason-1 satellites over the Indian Ocean on the 26 December 2004. Consequently the results of Occhipinti et al. (2006) closed the debate about the nature and the existence of the tsunami signature in the ionosphere. Those results obtained by Occhipinti et al. (2006) were also later reproduced and confirmed by Mai & Kiang (2009).

Further studies have shown several ionospheric tsunami detections in the far field by GPS-derived TEC (Rolland et al., 2010). The observed ionospheric perturbation is moving coherently with the tsunami at sea level. Comparison with oceanic data from DART buoys shows similarity both in the waveform as well as in the spectral signature of the ionospheric and oceanic data, again proving that the ionosphere is sensitive to the tsunami propagation.

Particular attention has been paid to the Tohoku-Oki event (11 March 2011, M_w=9.0) as one of the strongest earthquakes that also induced a fatal tsunami. Thanks to the great coverage of the really dense GPS network in Japan

(GEONET), the co-seismic TEC perturbations at the source give a clear image of the ionospheric perturbation in the near-field (Tsugawa et al., 2011; Saito et al., 2011; Rolland et al., 2011, Occhipinti et al., 2013), including the acoustic-gravity waves generated by the vertical displacement of the source (Astafyeva et al., 2011), acoustic waves coupled with Rayleigh waves (AGW_{epi}) as well as the gravity wave induced by the propagtion of the tsunami (IGW_{tsuna}) (Liu et al., 2011; Galvan et al., 2012, Occhipinti et al., 2013). The analysis of the first arrival in TEC data allowed to also localize the epicenter with less than 100 km difference from the official USGS localization (Tsugawa et al., 2011; Tsai et al., 2011; Astafyeva et al., 2011). The physical characteristics of the observed AGW_{epi}, IGW_{tsuna} and $AW_{Rayleigh}$ are detailed by Occhipinti et al. (2013) and Occhipinti (2015).

For the Tohoku-Oki event Heki (2011) found an anomalous enhancement of the ionospheric total electron content immediately before the large earthquake claiming to be earthquake precursors. Heki & Enomoto (2015) confirmed those findings for all earthquakes of this century with M_w>8.2. Several papers (e.g. Kamogawa & Kakinami, 2013; Utada & Shimizu, 2014) criticize Heki (2011) by interpreting the anomaly as a decrease of the ionospheric plasma density after the earthquake, that the authors called Ionospheric Hole. Masci et al. (2015) did a statistical analysis of the surrounding 30 days showing that the magnitude of the anomalies lies within the standard deviation of the whole 30 day dataset and therefore neither the hole nor the enhancement cannot be distinguished from other daily variations. Although Heki & Enomoto (2013), Heki & Enomoto (2014) and Heki & Enomoto (2015) replied to the criticism, the hole vs enhancement debate, to explore the possibility to predict earthquakes and their magnitude, is still open today. A more detailed description can be found in Chapter 3 that is entirely dedicated to the hole vs enhancement debate.

1.6 Richter Exercise Caraibes 2017

A Richter crisis management exercise took place from 21 to 24 March 2017. The simulation ran on an unprecedented scale, testing responses to a major earthquake. The exercise simulated an M_w 8.5 earthquake in north-eastern Guadeloupe (of similar intensity as the devastating earthquake of 1843), generating a tsunami hitting all of the islands coastlines as well as a large part of the Caribbean Arc.

Taking the opportunity of the Richter Exercise and the Lesser-Antilles scenario, we were able to quickly calculate the TEC in the ionosphere using COCONet (Continuously Operating Caribbean GPS Observational Network) data and produced the first image of the TEC variations for selected stations (Figure 19). The produced image of the TEC variation is included in the official report for the Richter exercise proving that the ionospheric monitoring, and more generally the ionospheric seismology, is getting accepted by the seismic community and could -in the near future- be included in the operational scenario for warning purpose and tsunami risk estimation. This effort shows the importance of exploring the possibility to run the processing of TEC data in real time for future use in an early warning system.

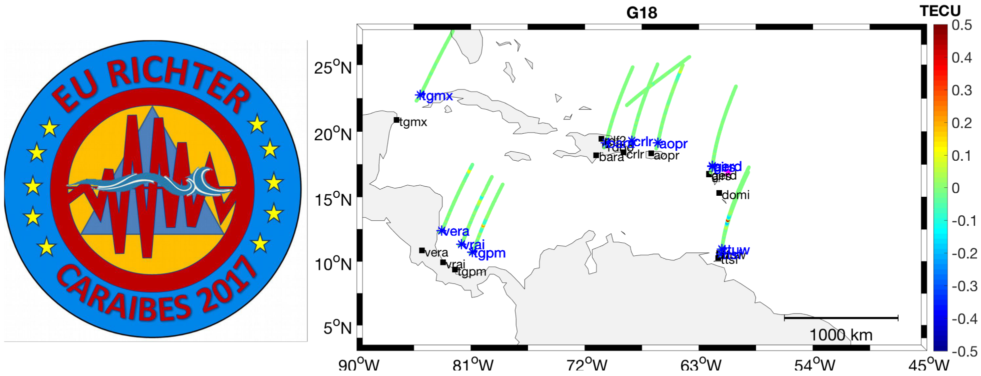

*Figure 19: Left: Logo of the Richter Exercise. Right: TEC variations for selected stations in the Caribbean for satellite 18. Positions of the GNSS stations are marked with a black square. Blue * shows IPP at the time of the assumed earthquake. The lines starting at the time of the earthquake show TEC variations of the station-satellite pair over time.*

2 TEC signature of Solar Eclipses

In this Chapter we explore the recent progress in the analysis of the ionospheric signature of Solar eclipses: nominally the Great American Eclipse (21 August 2017) and the South American Eclipse (2 July 2019). The first was visualized by the entire GNSS network in the United States opening terrific perspectives in the analysis of the effect of the Solar eclipses in the ionosphere.

2.1 The Great American Eclipse

On the 21st August 2017 the eclipse shadow drastically changed the state of the ionosphere over the USA. This effect on the ionosphere is visible in the total electron content (TEC) measured by GNSS. The shadow moved with the supersonic speed of ~1000 m/s over Oregon to ~650 m/s over South Carolina. In order to exhaustively explore the ionospheric signature of the eclipse, we use data of total electron content (TEC) from ~3000 GNSS stations seeing multiple GPS and GLONASS satellites to visualize the phenomena. This tremendous dataset allows high-resolution characterization of the frequency content and wavelengths -using an omega-k analysis based on 3D Fast-Fourier-Transform (FFT)- of the eclipse signature in the ionosphere in order to fully identify traveling ionospheric disturbances (TIDs). We confirmed the generation of TIDs associated with the eclipse including TIDs interpreted as bow waves in previous literature. Additionally we revealed, for the first time, short (50-100 km) and long (500-600 km) wavelength TIDs with periods between 30 and 65 minutes. The sources of the revealed short wavelength TIDs are co-located with the regions of stronger gradient of EUV related to sunspots. Our work confirms and describes the physical properties of the waves observable in the ionosphere during the Great American Eclipse.

2.1.1 Introduction

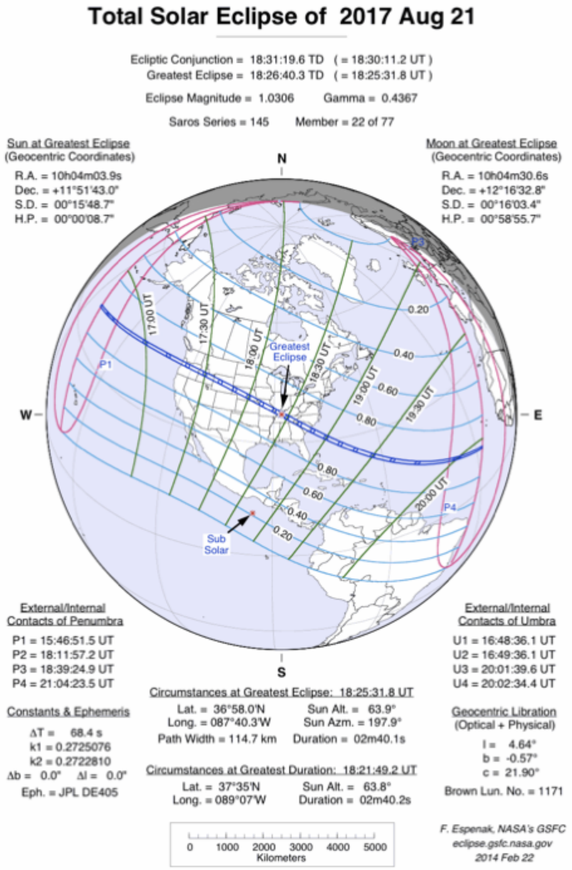

Figure 20: Map of the eclipse path and details of its physical properties. From: eclipse.gsfc.nasa.gov

During the total solar eclipse of 21st August 2017 the Moon's shadow travels with supersonic speed (~1000 m/s - 650 m/s) from the west to the east coast of the continental US. It takes about 95 minutes for the shadow to cross the USA. The exact path of totality as well as the boundaries of 80, 60, 40 and 20% magnitude and the physical properties of the eclipse are shown in Figure 20. Called the Great American Eclipse nowadays, the first total eclipse visible in North America in the XXI century, it also traverses a dense network of ~3000 GNSS stations giving, for the first time, the unique opportunity to analyze and deeply explore the effect of the Moon's shadow on the ionosphere with high spatial resolution. The Moon's shadow crosses the North American continent from ~10:00 local time (LT) in Oregon to ~15:00 LT in South Carolina.

Therefore, the largest eclipse effects would be expected over the central US between local noon and 13:00 LT, when the solar radiation is highest. The radical changing of the solar radiation due to the Moon's shadow produced a quick electron density decrease in the ionosphere, clearly visible in the total electron content (TEC) measured by GNSS stations. Indeed, the TEC represents the electron density integrated along a ray-path between a GNSS station and a satellite. The magnitude of the TEC depletion produced by the Moon's shadow was already studied in the past and was found to depend on the latitude (Le et al., 2009). Other studies confirmed this effect: for a total solar eclipse the TEC depletion can reach 30-40% at mid latitudes with a delay of 5-20 min after the passing of the Moon's shadow (Jakowski et al., 2008; Ding et al., 2010), 10-30% at high latitudes (Afraimovich et al., 1998; Momani et al., 2010; Hoque et al., 2016) whereas for the equatorial latitudes it can reach more than 40% due to the increased ionization within the equatorial anomaly (Tsai and Liu, 1999). The effect related to the latitude mainly depends on the elevation angle of the Sun and therefore higher ionization at low latitudes, which increases the background TEC and it amplifies the effect of the solar eclipse.

The TEC depletion due to the Moon's shadow and the related change of the solar flux is not the only effect that is expected to occur during the eclipse. The supersonic speed of the shadow of the Moon is predicted to excite lower atmospheric acoustic and gravity waves that can reach the ionosphere and generate various traveling ionospheric disturbances (TIDs), some of them explained as bow waves (Chimonas, 1970; Chimonas and Hines, 1971) that are preceding and trailing the solar eclipse and are produced by the reduction of heating sources (e.g. ozone at 45 km or extreme ultraviolet heating above 100 km). TIDs generated by the eclipse have been found to have a wide range of wave periods, ranging from 4 minutes (Sauli et al., 2006), 60 minutes (Jakowski et al., 2008) and to 87 minutes (Liu et al., 1998). Additionally, TIDs with a period of 20-40 minutes have been interpreted as bow waves (Ivanova et al., 1998).

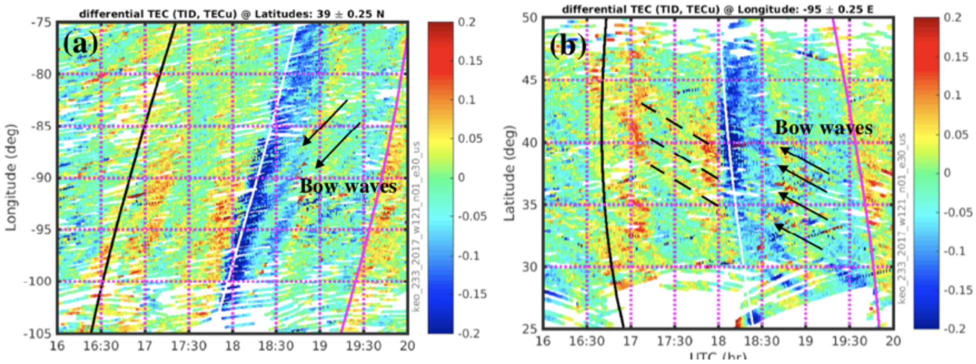

Figure 21: Keograms by Zhang et al. (2017) showing the time evolution of differential TEC at 39° latitude (top) and -95° longitude (bottom). The observed bow waves are marked with black arrows. From: Zhang et al. (2017)

First results for the 21 August 2017 solar eclipse confirmed the expectations by detecting a TEC depletion due to the Moon's shadow as well as the consequent generation of bow waves induced by the supersonic speed of its moving, and other TIDs were clearly visible in the TEC thanks to the high spatial resolution of the dense GNSS network over the entire US (Zhang et al., 2017; Coster et al., 2017; Cherniak and Zakharenkova, 2018; Sun et al., 2018). Those first studies mainly used keograms to obtain information about the TIDs. Pradipta et al. (2018) confirmed those first observations and the predictions by Huba & Drob (2017) additionally using ionosonde data. Nayak and Yigit (2018) performed a 2D Fast-Fourier-Transform to analyze the frequency content of the TIDs at selected stations. Their results showed TIDs with a dominant peak at about 20-30 minutes and broadly extended to 20-90 minutes periods, without details about the wavelength of the observed TIDs. A simulation of bow waves during the eclipse (Lin et al., 2018) reproduced TIDs with a period of 20-30 minutes (Figure 22) and therefore similar characteristics to the bow waves observed by Zhang et al. (2017) and also fall within the range of the dominant frequency peak of the TIDs observed by Nayak and Yigit (2018). The modeled thermospheric/ionospheric bow waves by Lin et al. (2018) and Lei et al. (2018) are evanescent in situ generated bow waves (Ridley et al., 1984) and are not a wavefield generated at stratospheric heights as predicted by Chimonas (1970). Harding et al. (2018) present observational evidence for those thermospheric bow waves using direct measurements of a neutral wind disturbance on the nightside. A simulation of the global upper atmospheric responses to the eclipse by Dang et al. (2018) shows that the effect of the eclipse is not just regional but global and that large-scale atmospheric disturbances were triggered by the eclipse. Thermospheric winds lead to a large TEC enhancement over South America. Aryal et al. (2019) observe wave-like perturbations in red and green line brightness from ground-based optical measurements. Although the ionosphere-thermosphere system could still be perturbed by the solar eclipse they link LSTIDs generated during the night, with a dominant period of about 1.5 hours and a long wavelength of more than 1000 km, to an increased geomagnetic activity.

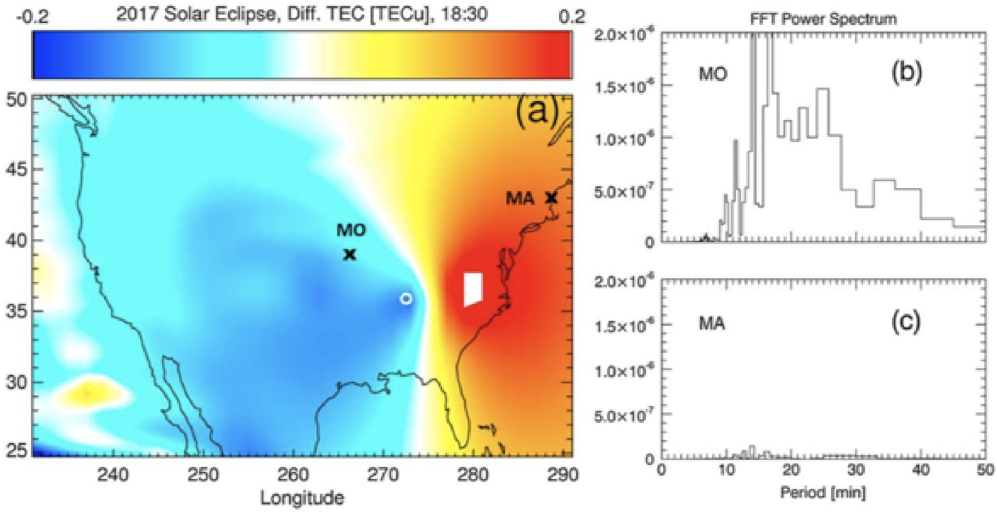

Figure 22: Results of Lin et al. (2018) for modeling the eclipse. a) differential TEC over North America at 18:30 b) Spectrum for synthetic TEC shown in a) at a specific location in Missouri (MO), marked with a cross in a). c) Same as b but for a location in Maryland (MA), also marked in a)

The debate about the physical origin of the perturbations and waves observed during the eclipse in the ionosphere is still open. For instance, Mrak et al. (2018a) name the modulation of the extreme ultraviolet (EUV) related to high energy sunspots as the origin of the TIDs instead of the generation of bow waves (Figure 24). More recent work of Mrak et al. (2018b) claim that thunderstorm initiated gravity waves are a source for observed TIDs before as well as during the eclipse, in addition to the EUV (Figure 23).

Here, we present -for the first time- a complete omega-k analysis, based on 3D-Fast-Fourier-Transform, of the TEC variation observed by GNSS during the solar eclipse over the entire US to highlight extensively the main periods, wavelengths and speeds of the observed waves and separate the signature of the different observed waves.

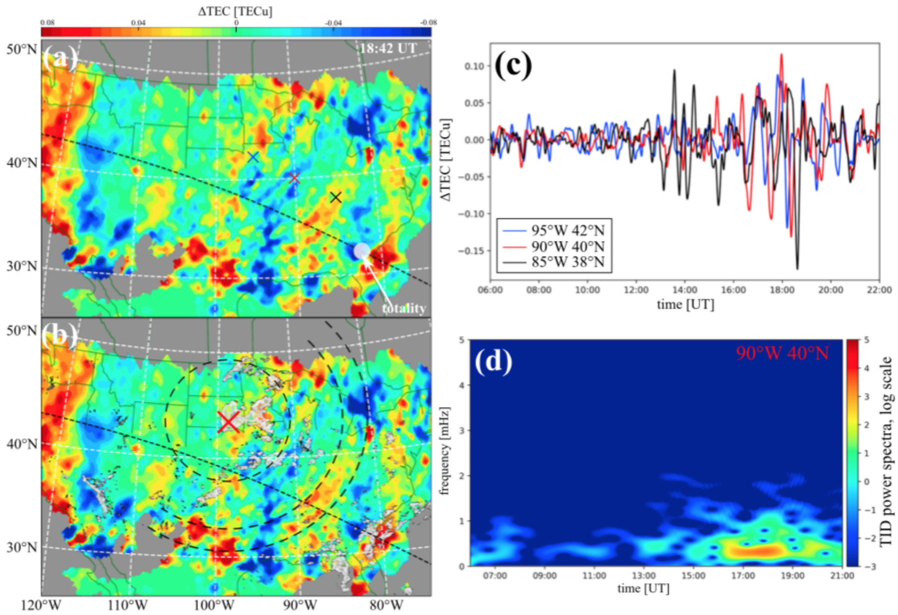

Figure 23: (a) An image of traveling ionospheric disturbances trailing the totality (white circle), the TIDs are modulated on top of the salient eclipse-induced modification. The image bolsters simultaneous and cooperative forcing of the ionosphere from below (TIDs) and from above (large-scale TEC perturbations). (b) Same as panel (a) with an overlay of tropospheric weather storms (gray) from the Next Generation Weather Radar maps. Red X denotes a position of the most intense precipitation inside the storm system. Dashed fiducial lines emphasize concentric nature of TIDs, with a center in the storm system, center of the red X. (c) Time series plot of dTEC perturbation for three regions identified X in panel (a). (d) A representative spectrogram of dTEC at 90°W, 40°N. From: Mrak et al. (2018b)

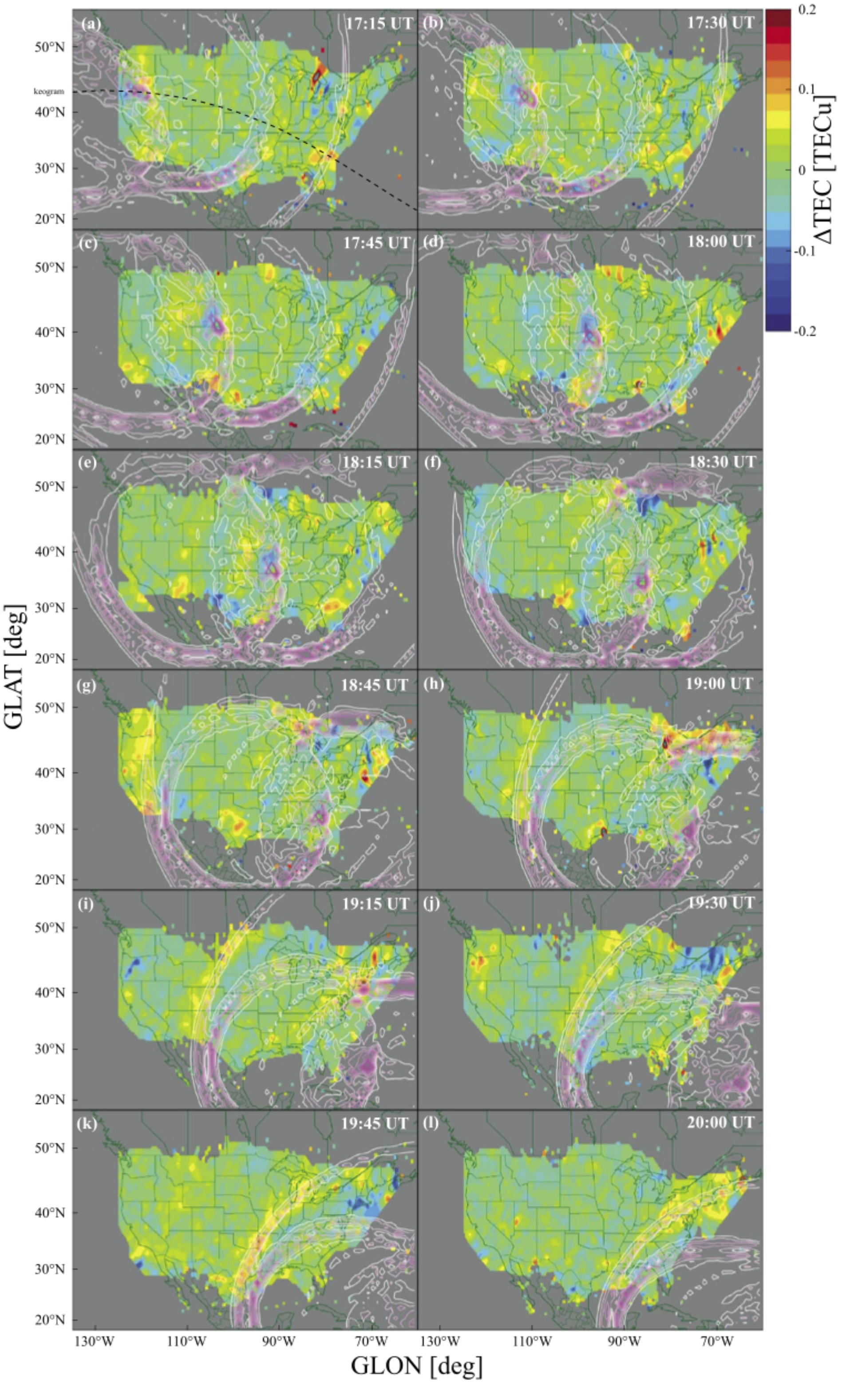

Figure 24: (a-l) Successive snapshots of imaged TEC residuals at 15-minute interval. Each image consists of an overplotted (contours) EUV Laplacian of the penumbra. Individual large-scale TEC disturbances (1)-(4), caused by the EUV modulation, are identified. Dashed line in panel (a) depicts the center line of totality at 300 km. From: Mrak et al. (2018a)

2.1.2 Data & Methodology

In order to visualize the TEC perturbations induced by the solar flux variations related to the Great American Eclipse, we used an extensive database consisting of ~3000 GNSS stations and capturing signals from GPS and GLONASS satellites. Using both GPS and GLONASS increases the number of available data by a factor of 1.5-2 compared to the use of GPS only. The used ground-based stations continuously record data with a sampling rate of 30s. We only use data of satellite-station pairs with an elevation angle of more than 15°. As mentioned above, the TEC is the integral of the electron density along the line-of-sight between the ground-based GNSS receiver and the satellite. The slant TEC (sTEC) for each satellite-receiver pair is converted to vertical TEC (vTEC) for the height of the maximum ionization of the ionosphere, so it represents the vTEC directly above the receiver. For the conversion of slant TEC to vertical TEC we use the following mapping function (Dautermann & Calais, 2008):

$$vTEC = sTEC * \sqrt{1-\left(\frac{\cos(\theta)R_E}{R_E+h_I}\right)^2} \tag{25}$$

where Θ is the satellite elevation angle, R_E is the mean radius of the Earth and h_I the height of maximum ionization in the ionosphere (here 300 km).

In order to compute the differential vTEC to use for the omega-k-analysis, we define the unperturbed background as the polynomial fit of 10th degree of our data. According to Mrak et al. (2018a) the polynomial fit of 10th degree creates artificial maxima and therefore they used a different approach splitting the data and using two polynomials of varying degree. By filtering the raw data using a butterworth bandpass filter from 0.2 – 2 mHz we can show that those maxima are also present in the filtered data and therefore are not artificial (Figure 25). The differential vTEC for each receiver-satellite couple is computed separately. The differential vTEC -shown in detail in the supplementary materials (Movies S1 and S2) and resumed in Figure 27, was computed using only a running mean filter to highlight the TEC depletion due to the eclipse. Further analysis of the eclipse induced phenomena by omega-k analysis is done using the polynomial fit as the only filtering as this provides the best signal to noise ratio.

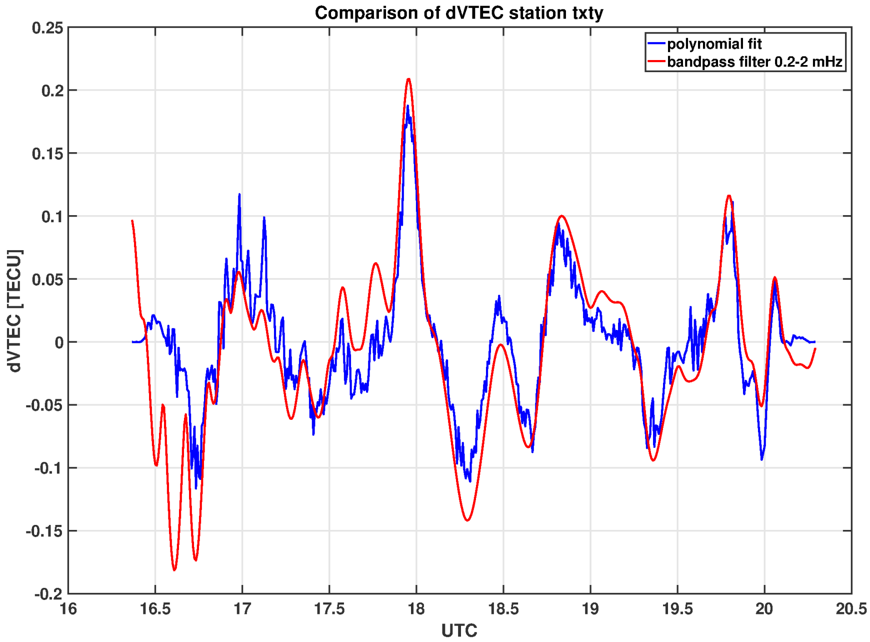

Figure 25: Comparison of differential VTEC for station txty in Texas. In blue dVTEC computed using a polynomial fit and in red using a butterworth bandpass filter from 0.2 – 2 mHz. The plot shows that the polynomial fit is indeed working well for the eclipse and not creating artificial maxima as stated in Mrak et al. (2018a)

Our omega-k analysis consists of detecting plane wave structures of the form $A_0 e^{-i(\boldsymbol{k}\cdot\boldsymbol{r}+\omega t)}$ in the space-time domain of the differential vTEC dataset, where omega ω represents the wave's angular frequency which equals to 2π/T, where T is the period of the wave, and ***k*** is the wave vector, which is the vector with a length equal to the wavenumber *k* in the direction perpendicular to the wavefronts. This means $|\boldsymbol{k}|=k=2\pi/\lambda$. The direction of the wave vector ***k*** is ordinarily the direction at which the plane wave is traveling. This signal representation is adequate to detect the traveling waves signature by both measuring their characteristic temporal scale as well as their physical extent in the considered region. For the computation of the omega-k analysis we use the Fast Fourier Transform algorithm (Bracewell & Bracewell, 2000).

For the omega-k analysis we use differential vTEC computed with a polynomial fit as described above. This gives us a better signal to noise ratio performing the Fourier transform compared to the use of the running mean filter or bandpass filter and therefore enables to detect and differentiate the TIDs. Note that no further filtering is performed, theoretically allowing the detection of low-frequency waves with periods larger than one hour. The discrete values for the angular frequency ω depend on the length of the total duration T_{length} of our differential vTEC dataset and the sampling rate dt, where ω ranges from -π/dt to π/dt in steps of $2\pi/T_{length}$. The discrete values of the k-vector **k** (k_x, k_y) are described as follow: k_x depends on the size dlx of the grid cell in longitude and the size L_x of the whole grid's dimension in longitude (~4600 km); consequently k_x ranges from -π/dlx to π/dlx in steps of $2\pi/L_x$.

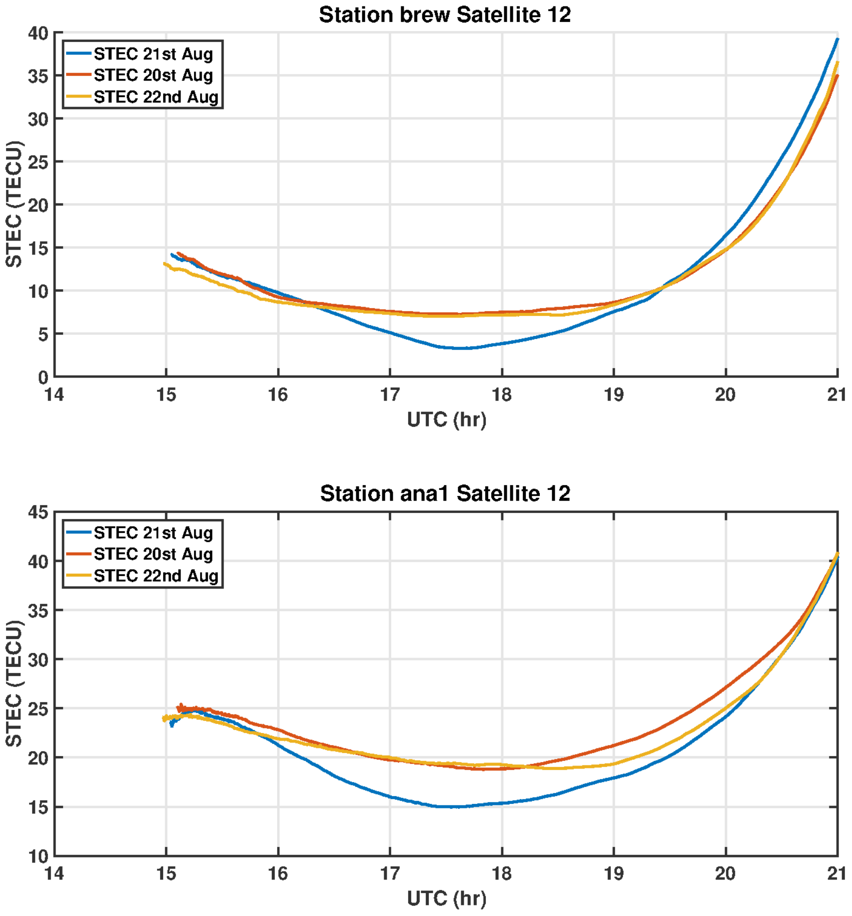

Figure 26: Absolute sTEC for satellite 12 and stations brew (up) and ana1 (bottom). Shown is the absolute sTEC for the day of the eclipse (blue) as well as the day before (red) and the day after (yellow) the eclipse. The stations are located within the path of totality (brew) and within 80% obscuration (ana1)

Following the same description, k_y depends on dly and Ly, respectively the cell size and the whole grid's dimension in latitude (~2200 km). The ω and **k**

(k_x, k_y) are related to period $T=2\pi/\omega$ and wavelengths **λ** (λ_x, λ_y) = ($2\pi/k_x$, $2\pi/k_y$) and expressed in minutes and km respectively to simplify the description of the observed TIDs.

In order to perform the omega-k analysis of the ionospheric signature of the eclipse, the differential vTEC is averaged and binned into a grid laid over the US from 30° – 50° in latitude and 235°-290° in longitude with cells of 0.28° x 0.39° in latitude/longitude, respectively. No interpolation is applied, so that cells without data are marked as blank. The blank cells are set to zero, they correspond to around 11% of our grid cells. As we use differential TEC for the TEC maps, setting blank cells to zero implies that there's no variation of the TEC in that area at that time. The maximum number of station satellite pairs binned in one pixel varies from 60-100 for each epoch, whereas the average number of dTEC measurements per cell is around 35. The 3D FFT is computed by doing a 1D Fast Fourier Transform in each direction of the three dimensional array. The TEC maps were created each 30s for a period of 4 hours starting at 16:18 UTC which is one hour before the center of the eclipse first enters Oregon. The resulting 3D box of 2D TEC maps per 30 seconds over 4 hours is used as input for the 3D Fast-Fourier-Transform. This tremendous dataset allows a deep analysis of the frequency content and wavelength of the eclipse signature in the ionosphere in order to fully identify the waves associated with the eclipse phenomena.

To highlight the TIDs detected in the omega-k space we perform an inverse 3D FFT to show the propagation of the TID in time domain. The inverse 3D FFT is performed for only the part of the cube identified as contributing to the TID and all other cells are set to zero.

2.1.3 Results

Figure 27 shows the differential vTEC map for four different time-steps during the eclipse, from 16:30 UT before the Moon's shadow appears over Oregon until 19:30 UT when the Moon's shadow moved past North America. For better comparison with the day before and after the eclipse we compute absolute sTEC. To correct for the satellite bias we use the values from the CODE IONEX files of the University of Bern. The receiver bias is removed using the minimum-scalloping method (Rideout & Coster, 2006). We compare the absolute sTEC single station-satellite of the eclipse day with the day before and the day after the eclipse, in order to highlight the level of perturbation - reaching around 5 TEC-unit (TECU), and corresponding to 25 % of the background TEC, produced by the eclipse (Figure 26). We also show differential vTEC maps in order to highlight higher frequency perturbations and wave propagation (Figure 27). Before the Moon's shadow arrives over Oregon, no ionospheric disturbances are detectable in the differential vTEC map. A strong depletion of ~0.4 TECU is located in the area corresponding to the 100% of shadow and it affects large parts of the US until the 60 % of shadow. The eclipse TEC depletion is clearly visible in the TEC maps from 17:30 to 19:30 UT. The largest depletion has a time lag of ~10 min to the center of total eclipse, showing the time of reaction of the ionosphere to the change of solar flux. The TEC depletion follows the Moon's shadow during its movement across the U.S. and the TEC background returned to normal level

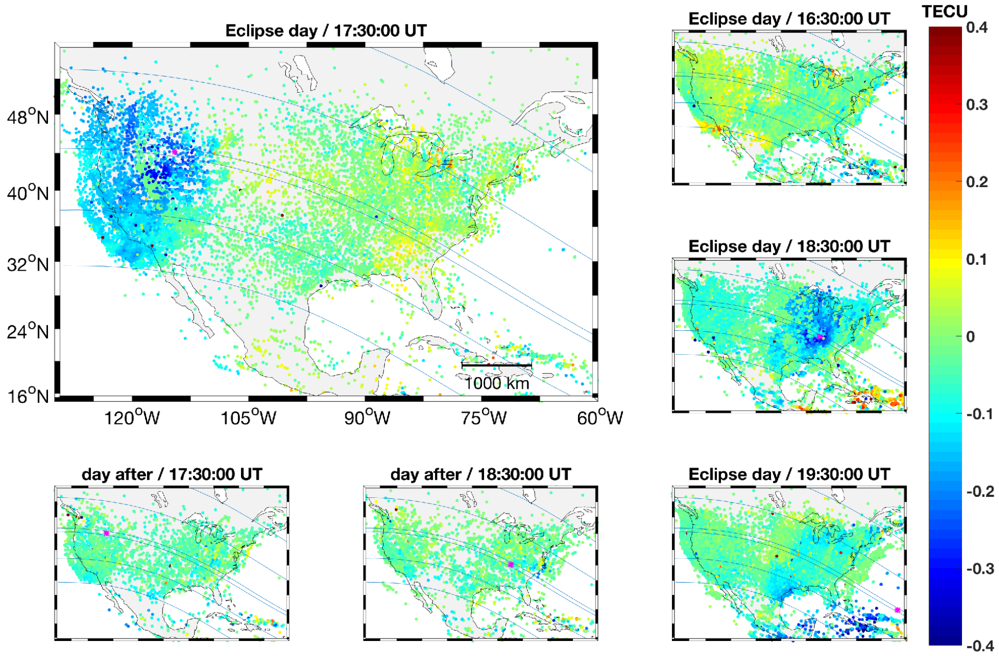

Figure 27: TEC maps for the eclipse day (top left and right side) and for 22 August, the day after the eclipse (bottom, left and center). Shown are differential vTEC values for 4 moments of time during the totality passing over the US (16:30 UT, 17:30 UT, 18:30 UT and 19:30 UT). The location of each observation is the piercing point at 300 km of altitude. The blue lines are the northern and southern boundary of the totality, 80% and 60% of magnitude while the magenta star shows the location of the center of totality.

after the Moon's shadow left North Carolina. Besides the depletion caused by the Moon's shadow other waves are visible, identified as general TIDs and also more specific bow waves preceding and following the main TEC depletion. Bow waves are expected to form if the penumbra moves faster than the local sound speed (Chimonas, 1970, Chimonas and Hines, 1971). The sound speed in the ionosphere ranges from 600 m/s to 800 m/s (Picone et al., 2002). Therefore the speed of the Moon's shadow is supersonic on the west coast (~1100 m/s) but drops down to around sound speed at the east coast (~650 m/s) of the US.

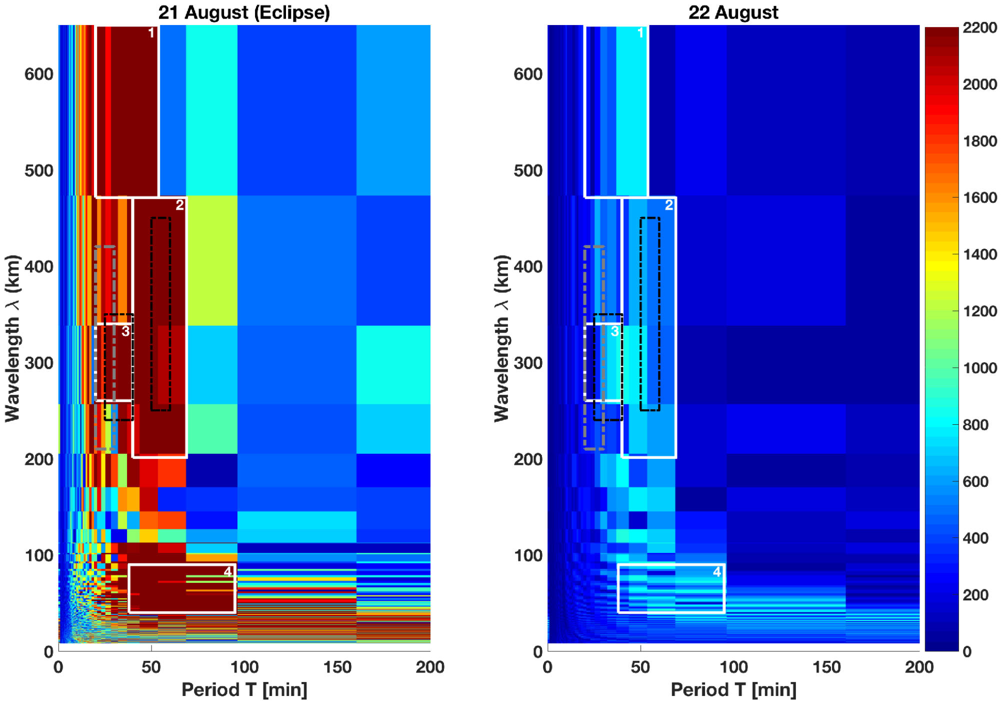

Figure 28: 3D FFT result for the day of the eclipse and the day after. The diagrams show the wavelength l over the period T of the observed waves. Colors show the intensity for specific wavelengths and periods. White boxes numbered one to four highlight the zones of high intensity associated with TIDs following the eclipse. The phase speed range for those boxes is as follows: 145-542 m/s (box 1), 49-196 m/s (box 2), 108-283 m/s (box 3) and 16-39 m/s (box 4). Black dashed boxes correspond to the observations and interpretation of Zhang et al. (2017): TIDs generated by the TEC depletion by the Moon's shadow (box 2) and by bow waves (box 3). The grey dashed box corresponds to modeled bow waves (Lin et al., 2018). The day after the eclipse is plotted for comparison and to show that the observed TIDs are not daily reoccurring but associated with the solar eclipse.

To further investigate the physical characteristics of the TIDs we perform the omega-k analysis on the differential vTEC maps using the 3D Fast-Fourier-Transform method on a grid of 0,28° x 0,39° in cell size in latitude/longitude. This means the size of a pixel is around 33 km in latitude and ranging from ~29 km at 50°N to ~38 km at 30°N in longitude. As mentioned above, the differential vTEC values were averaged for each cell and no interpolation applied. Cells without data were set to zero. The results of the 3D FFT show the wavelength over the period (Figure 28) to identify propagating waves. For comparison, the results for the day after the eclipse (22 August) are also shown to highlight that the observed TIDs (on 21 August) are induced by the solar eclipse and are not daily reoccurring events. To support our comparison between the two observed days, we highlight that geomagnetic activity for both days was low, so that the solar eclipse is left as the most likely explanation for the generation of the observed TIDs. In Figure 28 we see 4 zones with higher intensity, representing TIDs. To define the zones we look for cells with a significant higher intensity as the background and with neighbouring cells of the same intensity. We define the boxes trying to avoid including areas of lower intensity. Also it looks like for small wavelengths and long periods of 100 – 200 minutes there could be a zone of high intensity but this is regularly intercepted by cells of lower intensity and therfore not considerd as TID in this study. Zone 2 shows waves with period of 40-70 minutes and wavelength of 200-450 km, which confirms the observations of Zhang et al. (2017); they speculate that the source of those TIDs is the TEC depletion induced by the solar eclipse. In essence, Zhang et al. (2017) suggest that the TIDs are directly generated by the plasma density variation in the ionosphere. Zone 3, related to a period of 25-30 minutes and wavelength of 300 km, has been interpreted by Zhang et al. (2017) –using keograms- as bow waves induced by the supersonic speed of the shadow. Indeed, zone 3 also corresponds to physical properties of bow waves modeled by Lin et al. (2018) where the exact eclipse parameters were used to model the generation of bow waves in the low atmosphere, then propagating to the ionosphere. Additionally we found TIDs with period of 40-65 minutes and wavelength of 50-100 km (zone 4), as well as TIDs with period of 30-60 minutes and wavelength of 500-600 km (zone 1). The TIDs with physical properties corresponding to zone 1 and 4 were not yet reported in literature. They correspond to long (zone 1) and short (zone 4) wavelength gravity waves that are potentially generated in the low neutral atmosphere and perturb the ionosphere during their upward propagation or are directly generated at ionospheric altitude by the quick plasma density change as speculated by Zhang et al. (2017). Additionally, the short wavelength gravity waves related to zone 4 present localized sources that around 18:00 UT correspond to the regions of stronger gradient of EUV as suggested by Mrak et al. (2018a) and support their hypothesis on the role of the modulation of EUV related to sunspots in the ionospheric signature of the eclipse (Figure 29). Our results support the idea that the localized effect of sunspots generates short wavelength TIDs moving at around 16-39 m/s (zone 4) that co-exist with bow waves (zone 3) and other TIDs (zone 1 and 2) related to the eclipse.

In order to better visualize the TIDs related to the 4 boxes, Figure 3 shows the results of an inverse 3D FFT of each box identified in Figure 28. It shows the propagation of those TIDs in time domain after filtering in the omega-k space for the characteristics seen in Figure 28. As described above, box 2 represents the TEC depletion by the shadow of the Moon itself and it’ss clearly visible in Figure 29 in the plot to the upper right that the depletion corresponds to the position of the totality with a small time lag. Box 1 shows the same correlation with the totality for a longer wavelength. Same as box 2 it represents the TEC depletion due to the Moon’s shadow itself but with a longer wavelength then reported for this eclipse before. Box 3 is linked to show the same characteristics as the TIDs described as bow waves by Zhang et al. (2017) or modeled by Lin et al. (2018) and as we see in Figure 29 in the bottom left plot it’s not only limited to the position of totality but seems to create a wavefield trailing and preceding the totality. Those oscillations are partially showing the limitations of our methodology that is sensitive to detecting plane wave structures and introducing oscillations in the inversion for structures not fully fulfilling this. Box 4 shows circular structures that seem related to a more static source. Their position doesn’t correspond to thunderstorms occurring during the eclipse (Mrak et al., 2018b), but around 18:00 UT the position corresponds to that of EUV modulations shown by Mrak et al. (2018a). Aryal et al. (2019) show that increased geomagnetic activity after the eclipse generated large scale TIDs with a wavelength of more than 1000 km and a dominant period of 1.5 hours. As our choice of the grid limits the resolution to a maximum wavelength of 600 km we can’t see TIDs of the same type during the day, although Box 4 lies within the same period.

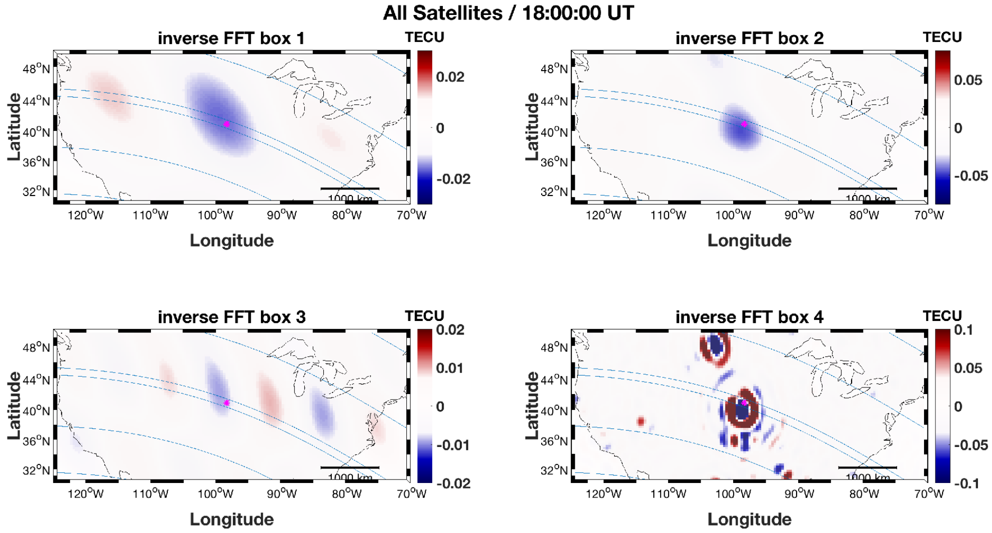

Figure 29: Results for boxes 1-4 from Figure 2 after filtering the data for characteristics of each box in frequency domain and performing an inverse 3D FFT. Shown is an image for each box at 18:00 UTC to highlight the characteristics of the TIDs. As in Figure 1 the magenta star shows the center of the totality at a specific time and the blue lines represent the northern and southern boundaries of the path of totality and 80/60% of obscuration respectively.

He et al. (2018) show results of a 3D tomography of the solar eclipse focusing only on the depletion due to the Moon’s shadow itself without further investigation of other TIDs. Notwithstanding additional efforts are necessary to clearly locate the altitude of TID formation, our work clearly quantifies the physical characteristics (period and wavelength) of the observed TIDs, their location and the propagation pattern. Modeling or 3D high-resolution reconstruction of the ionosphere (tomography) could help to fully understand whether the generation process happens at the low altitude neutral atmosphere or at ionospheric altitude.

2.1.4 Conclusion

The Great American Eclipse moved with a narrow 160 km wide Moon’s shadow over the entire North America during daytime (10:00-15:00 LT) and along a path from Oregon to North Carolina. Outside of the totality zone, a partial solar eclipse associated with the penumbra covered the majority of the US. This amazing and unique phenomena was also observed by the wide network of ~3000 GNSS stations. They showed for the first time, and with an unprecedently high spatial and time resolution, the response of the ionosphere visualized by TEC measurements all around North America. The TEC signature of the eclipse shows a strong absolute sTEC depletion of the order of 25% of the normal background estimated using the day before and day after the eclipse. We particularly image the signature of the eclipse on the entire North American subcontinent computing differential vertical TEC maps based on ~3000 stations and 21 satellites between GPS and GLONASS. Our differential vertical TEC maps show a depletion of -0.4 TECU in average following the Moon's shadow with a delay of around 10 minutes and broadly extended until 60 % of shadow in North America. Using different data fitting approaches we can show a proof of the existence of a bow wave trailing the eclipse in the TEC maps. We additionally use the high spatial and temporal resolution of our maps to fully analyze the wave propagation visible in the ionosphere as TIDs related to the Great American Eclipse: we perform an omega-k analysis by a 3D Fast Fourier Transform. We confirm the presence of TIDs with period of 40-70 minutes and wavelength of 200-450 km already observed in the literature using keograms, as well as the presence of TIDs with a period of 25-30 min and the wavelength of 300 km possibly triggered by the supersonic speed of the Moon's shadow. We also highlighted –for the first time in literature- longer wavelength (500-600 km) TIDs with a period of 30-60 minutes that are related to the TEC depletion due to the Moon's shadow, as well as shorter wavelength (50-100 km) TIDs with period of 40-65 minutes. Those last TIDs have sources co-located with the regions of stronger gradient of EUV at a specific time and consequently support the role of the modulation of sunspot in those waves generation. With our work we wish to push forward the full interpretation of the effect of the Great American Eclipse and generally the fast changing of the ionospheric plasma density related to quick solar flux variation.

2.2 South American Eclipse of 2nd July 2019

A total solar eclipse occurred at the ascending node of the Moon’s orbit on July 2nd, 2019, with an eclipse magnitude of 1.0459. Totality was visible from the southern Pacific Ocean east of New Zealand to the Coquimbo Region in Chile and Central Argentina at sunset, with the maximum of 4 minutes 32 seconds visible from the Pacific Ocean.

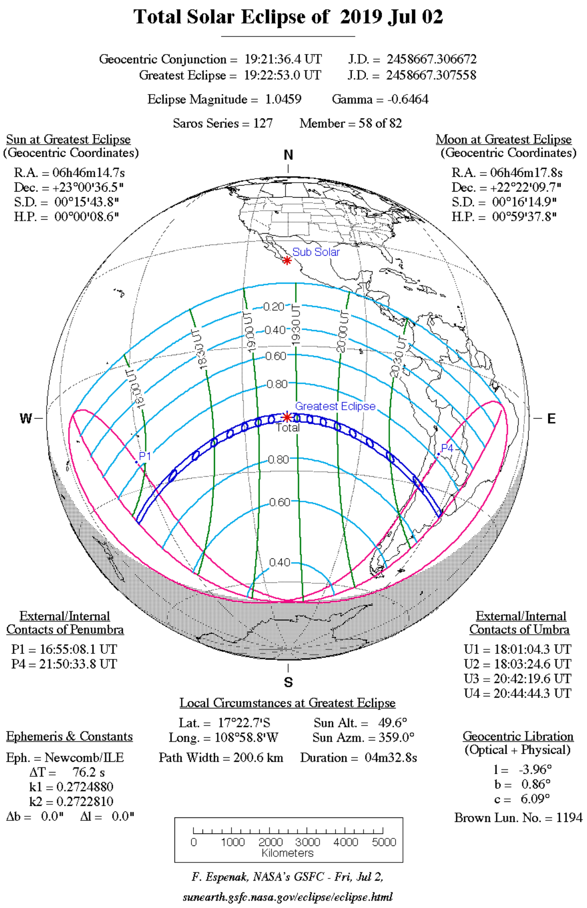

Figure 30: Eclipse path and parameters for the July 2nd, 2019 total solar eclipse over the South Pacific and South America. From: eclipse.gsfc.nasa.gov

During daytime around local noon when we would expect to see the biggest effect in the ionosphere the totality passed over the Pacific Ocean without any coverage by GNSS stations. By the time the Moon’s shadow reached the South American continent at the Chilean coast the Sun was already about to set and totality was visible for the last 4 minutes before sunset in Chile and Argentina. The path of totality is depicted in Figure 30. As shown in Chapter

2.1 the biggest decrease in TEC lags the totality by a few minutes. This means it is no surprise that for some station-satellite combinations no quick recovery of the TEC is visible as the expected time lag for the biggest decrease in TEC coincides with the sunset. The time of the appearence of the eclipse right before sunset makes it challenging to fully discover the effects on the ionosphere in this case.

2.2.1 Data & Methodology

To analyze the response of the ionosphere to the total solar eclipse we used the freely available data from the RAMSAC (Red Argentina de Monitoreo Satelital Continuo) network in Argentina (Pinon et al., 2018) and stations in neighboring countries as Chile, Uruguay or Brazil which gives us a total of around 110 stations in working order and receiving signals on the day of the eclipse. Although the coverage is by far not as dense as for the Great American Eclipse the stations cover fairly well the whole area as can be seen in Figure 31.

Although we already used GLONASS (Globalnaya navigatsionnaya sputnikovaya sistema) data for the Great American Eclipse this was not yet processed using the Spectre code (Lognonne et al., 2006). In order to uniformize the TEC computation, using the same software for both GPS and GLONASS data, for the analysis of the South American eclipse of July 2019, I implemented the computation of GLONASS TEC in the processing of the data. The main difference in processing GLONASS compared to GPS is in the different frequencies used for each satellite (FDMA – Frequency Division Multiple Access) depending on the channel it’s operating in, with only antipodal satellites using the same channels and therefore the exact same frequencies. As antipodal satellites can never be seen by one station at the same time this doesn’t pose a problem for the computation of the signal. The main advantage of FDMA when compared to CDMA (Code Division Multiple Access, as used by e.g. GPS) is that it guarantees signal separation since each signal is transmitted in a different frequency. On the other hand, it requires a higher complexity (and cost) regarding antenna and receiver design, related to the implementation of the different band-pass filters and calibration. The addition of GLONASS increases the number of measurements by 1.5 to 2 times compared to the use of GPS only.

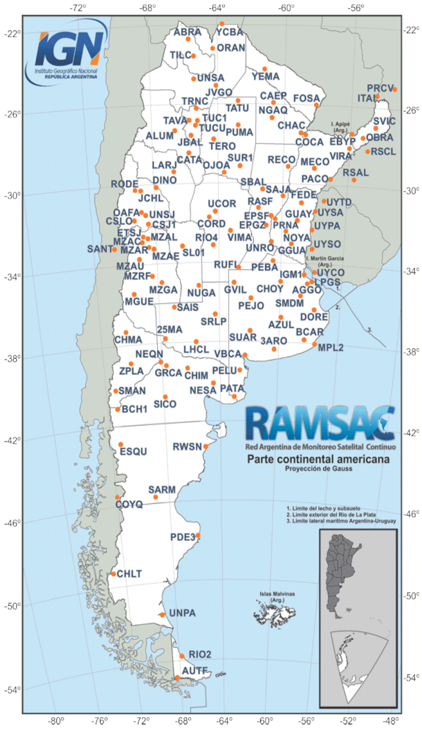

Figure 31: Map of the Argentinian GNSS network used for the total solar eclipse of July 2nd, 2019. From: Pinon et al. (2018)

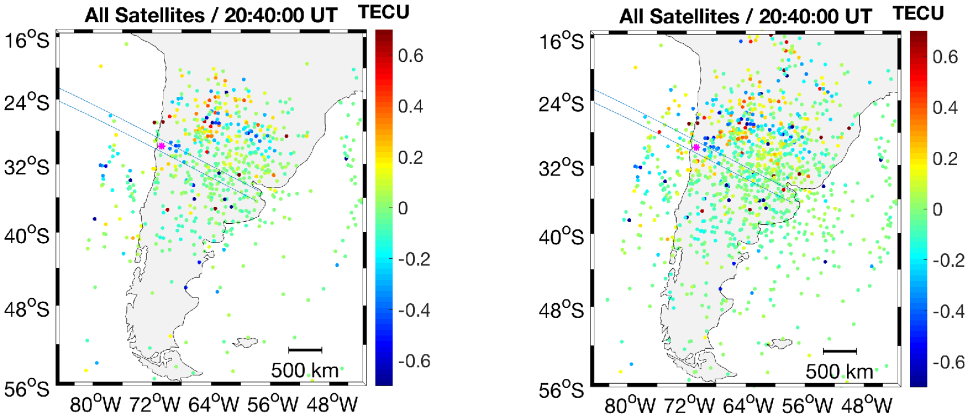

Figure 32: TEC maps at 20:40:30 UTC on July 2nd, 2019. Shown is the dTEC (computed using a polynomial fit) for GPS only (left) and GPS+GLONASS (right)

A comparison of this is shown in Figure 32. It's easily visible that the additional GLONASS satellites add not only more data points but also significantly increase the spatial coverage.

To compare the effect of the eclipse to the surrounding days for single station satellite pairs we have calculated absolute sTEC again as for the Great American Eclipse described in Chapter 2.1.2. For comparability we have set the three days to the same level for the time before the eclipse started.

2.2.2 Results

Figure 33 shows the absolute sTEC for the South American Eclipse compared to the surrounding days. The four stations are all in the western part of Argentina within the path of totality and not too far from the border with Chile. That is the part of South America that experienced the eclipse first, starting with 80% obscuration and the arrival of totality at approximately 20:40 UTC (Figure 30). In Figure 33 we can see a decrease in TEC starting around the time of the eclipse and reaching up to 15 TECU which resembles up to 40% of the background ionosphere of the surrounding days. In this case the TEC also doesn’t recover from the decrease as the end of the eclipse correlates with the sunset and therefore a lack of sun radiation to restore the state of the ionosphere prior to the eclipse. This is clearly visible for data from Satellite 19 used in Figure 33. The eclipse acts in a way as an abrupt early sunset and afterwards the ionosphere returns to normal sunset behavior without recovering from the strong depletion due to the totality. In the bottom plots of Figure 33 we see a bit different behavior compared to both stations using satellite 19. In both cases for station UNSJ and CSJ1 using satellite 30 and 13 respectively we see a depletion starting earlier and also the ionosphere recovering after the eclipse. We see a decrease of roughly 3-4 TECU which resembles 25-40% of the background ionosphere of the surrounding days.

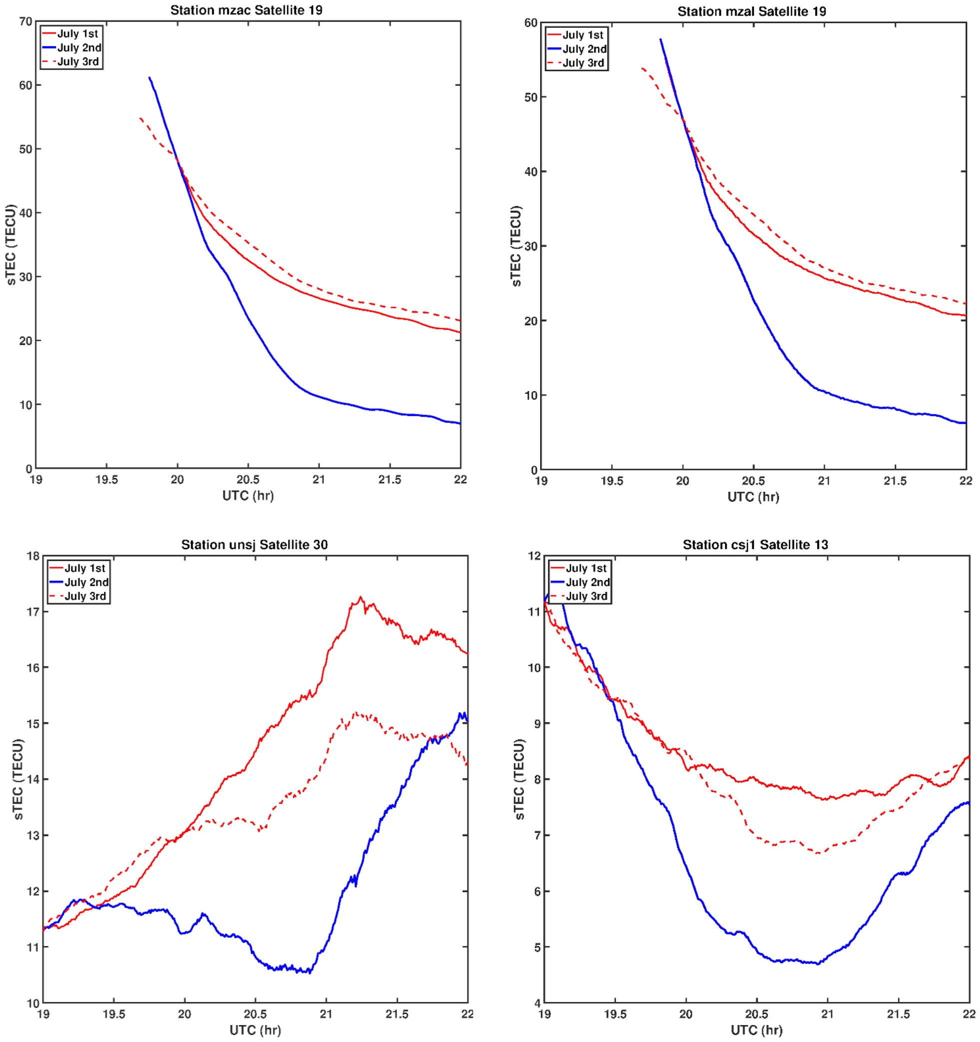

Figure 33: absolute sTEC for stations MZAC (top left), MZAL (top right) and satellite 19, station UNSJ (bottom left) and satellite 30 and station CSJ1 (bottom right) and satellite 13 for the Eclipse (blue) and the surrounding days (red)

Figure 34 shows the time evolution of the IPPs for the four shown satellite-station pairs. For satellite 19 (red lines in Figure 34) the satellite moves from the north right into the eclipse path and the signal stops when the satellite is a bit further south. This explains well the effect of the early sunset observed for those satellite station pairs (Figure 33). For the two other satellite-station pairs where we can see a recovery after the eclipse (Figure 33 bottom plots) the path of the satellite is moving through the path of totality but leaves it again on a northerly trajectory (black and magenta lines in Figure 34). Therefore we can see a recovery of the TEC after the eclipse for those two stations

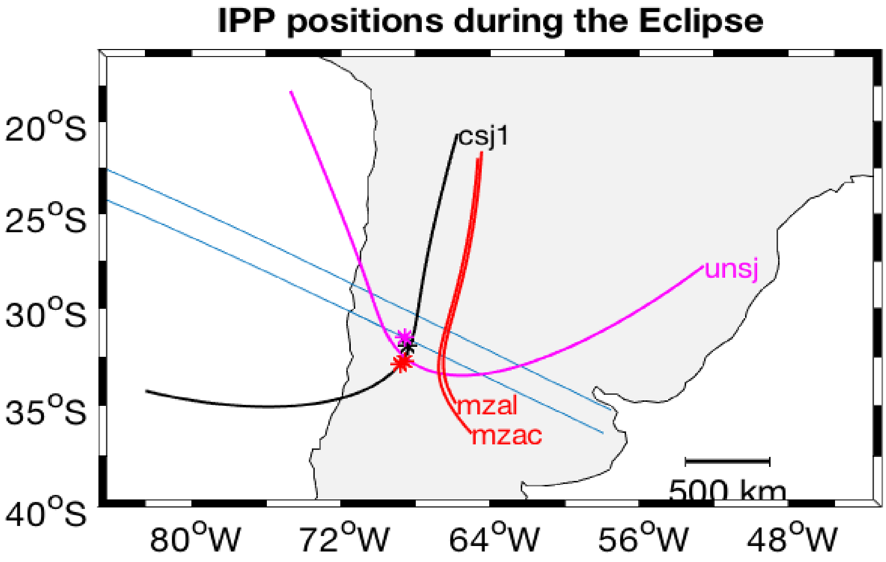

*Figure 34: Time evolution of the IPPs for the station satellite pairs shown in Figure 33. Same colors for same satellites. Positions of the stations is marked with an *.*

2.2.3 Conclusion

A total solar eclipse occurred on July 2nd 2019 over the Pacific Ocean and South America. Due to sparse or rather non-existent coverage over the Pacific Ocean we can only observe the last minutes of totality before sunset in Chile and Argentina. We could see a clear decrease in TEC for some stations in western Argentina where the Moon’s shadow first arrived over South America. Compared to the surrounding days those stations show a decrease of about 25-40% compared to the background ionosphere. This lies within the expectations for solar eclipses at mid-latitudes (Jakowski et al., 2008, Ding et al., 2010).

As also shown for station MZAL and MZAC, for which the IPPs moves further south in the path of the eclipse than the other stations shown, the TEC didn’t recover to the level before as the eclipse coincided with sunset. This made it challenging to show the depletion due to the eclipse using differential TEC for the spatial coverage on maps. Both the use of a polynomial fit as well as a bandpass filter didn’t show clear results due to the overlap of the eclipse with the sunset. Also due to the low elevation angle of the sun right before sunset the moon shadow at the ground doesn’t necessarily coincide with the position of the shadow in the ionosphere. Therefore the biggest effect would be expected slightly north of the path of totality on Earth. Nevertheless the implementation of GLONASS data in the processing added to the coverage compared to GPS use only. This increased the number of measurements by 1.5 to 2 times compared to GPS only and is a significant improvement of the Spectre code for processing GNSS TEC.

3 Hole vs Enhancement – Earthquake Precursors

The earthquake prediction has been investigated since a long time in order to prevent disaster and reduce the number of losses. Scholz et al. (1973) showed optimism that seismology was ‘on the verge’ of making reliable predictions. Nevertheless that optimism fell short by the 1990s with Geller et al. (1997) claiming that earthquakes cannot be predicted, followed by a debate (Main, 1999). Although precursors such as geochemical anomalies and seismic quiescence have been reported since (Uyeda et al., 2011), the research for the short-term precursors is still ongoing. Electromagnetic anomalies (Uyeda et al., 2009) and atmospheric-ionospheric anomalies (e.g. Liu et al., 2004; Kamogawa, 2006 and references therein) have been reported. Between the physical hypothesis explored, scientist imaged that during the nucleation process, the fault already acts as an electromagnetic dipole, producing electromagnetic perturbations detectable near the source, and perturbing the ionosphere. Notwithstanding the physical mechanism of the generation of EM perturbation is still not clear, many authors explored the possibility to highlight the existence of ionospheric anomalies with statistical studies (Liu et al., 2006; Hayakawa et al., 2011; Le et al., 2011). They tried to prove the statistical significance of the ionospheric perturbations preceding earthquakes, but a lot of arguments have arisen agains the existence of those ionospheric precursors (Rodger & Clilverd, 2007; Kamogawa, 2007). The reported anomalies in the ionosphere, interpreted as precursors, seem to appear randomly in the days or even weeks before the seismic events. As the ionospheric dynamics are strongly active, it is difficult to find coherence between the cause and effect of those presumed perturbations. The reported anomalies are also suspected to be other disturbances such as magnetic storm (Rishbeth, 2007).

As mentioned before in the introduction of this manuscript (Chapter 1.5.2), after the Tohoku event in 2011, Heki (2011) claimed to have found a TEC enhancement preceding the rupture by 40 minutes.

Heki (2011) shows the spatial distribution of the TEC enhancement observed by the GEONET network before the Tohoku-Oki earthquake with three

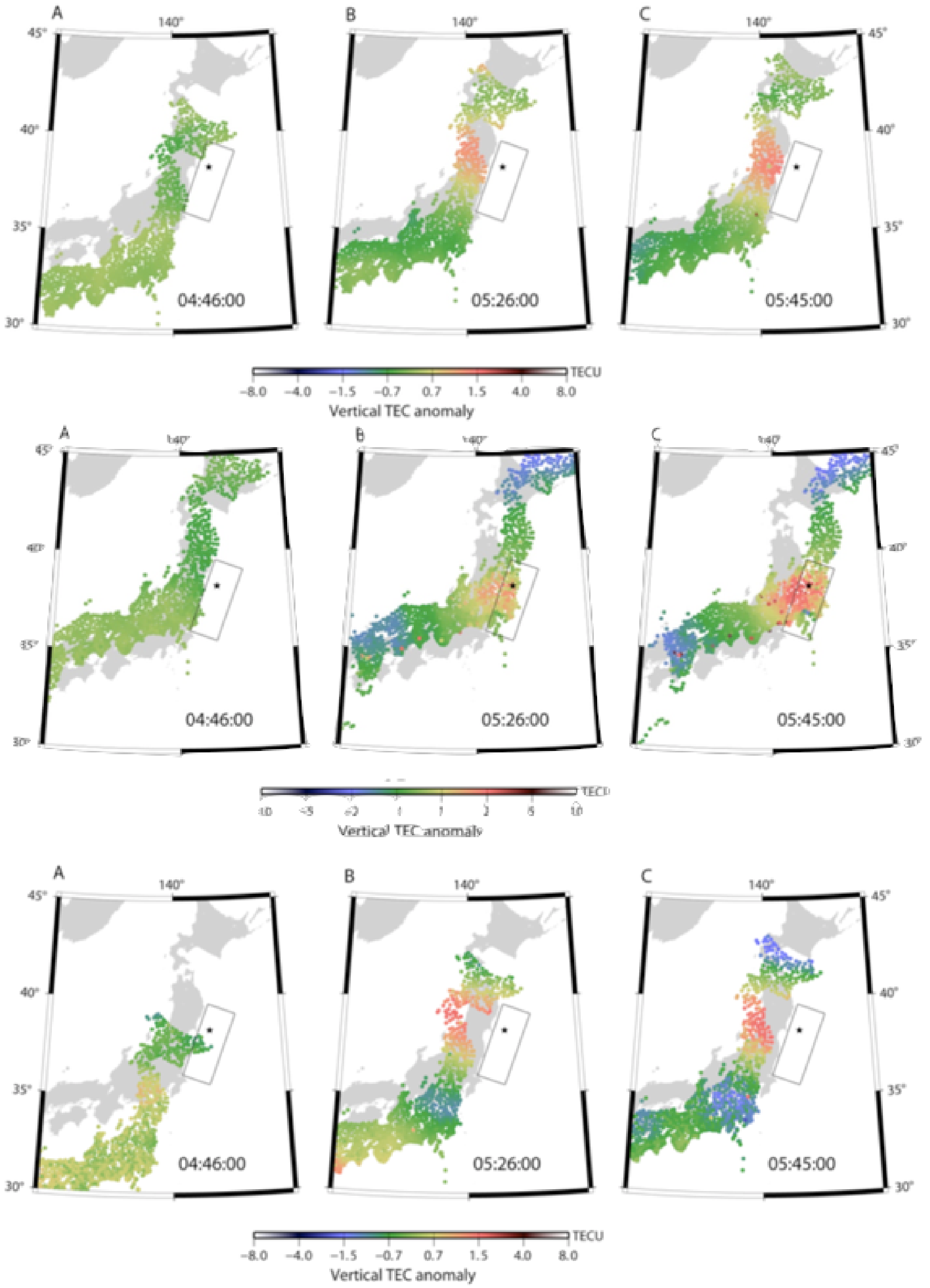

Figure 35: Vertical TEC anomalies at (A) 1 hour, (B) 20 minutes and (C) 1 minute before the Tohoku-Oki earthquake observed with satellite 27 (top), 26 (middle) and 9 (bottom). From: Heki (2011)

different satellites (Figure 35). The showed TEC enhancement is calculated as difference between the observed slant TEC and a polynomial fit to remove the unperturbed daily TEC background.

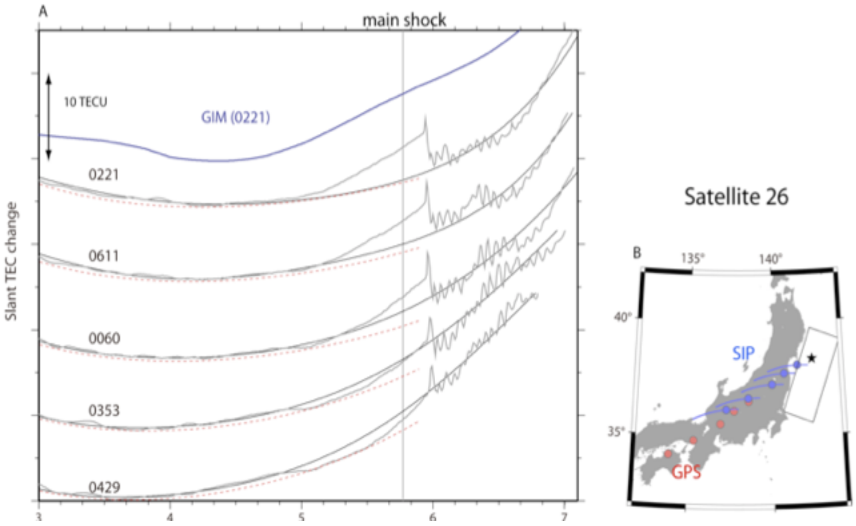

Figure 36: (A) Slant TEC change time series observed at five GPS stations with satellite 26. Black smooth curves are the models derived using a polynomial fit. The blue curve shows the slant TEC changes calculated using GIM for station 0221. Dashed curves in red show the models (polynomial degree 10) derived with data prior to the precursor onset (5.2 UT) and extrapolated to the later period. (B) Positions of five GPS stations (red dots) in (A) and their 5:00-6:00 UT SIP trajectories (blue dots show 5:46). From: Heki (2011)

Figure 36 shows the slant TEC and the corresponding TEC background fit for several stations for satellite 26. In order to calculate a TEC background not affected by the earthquake, Heki (2011) excluded, from the observed slant TEC, the time windows from the onset of the precursor to 20 minutes after the earthquake to calculate the polynomial fit. This approach produces a differential TEC showing the enhancement 40 minutes before the earthquake. To additionally support the hypothesis of the existence of the TEC enhancement starting 40 minutes before the earthquake, Heki (2011) also extrapolates the behavior of the beginning of the TEC curve, excluding the observation before the supposed increasing of the TEC (red-dashed line in Figure 36). The results of Heki (2011) were followed by a debate where other authors (e.g. Kamogawa & Kakinami, 2013; Utada & Shimizu, 2014) interpret the data differently: the TEC does not recover back to the unperturbed state at a normal rate but decreases after the acoustic wave generated by the source displacement (AGW_{epi}) reaches the ionosphere. In this interpretation the giant tsunami after the earthquake produces what they call the ionospheric hole: a wide depletion of the TEC on a hundred-kilometer scale and lasts for a few tens of minutes. Heki (2011) additionally showed the GIM model produced by the University of Berne for station 0221 (Figure 36): he mentioned that the GIM computation includes station 0221, consequently the GIM behavior already shows the enhancement. On the other hand, we can already interpret this behavior as a proof of the existence of the ionospheric hole after the arrival of the AGW_{epi} in the ionosphere instead of the enhancement before claimed by Heki (2011). Indeed, the GIM is calculated with a large scale resolution and a vast number of data. Consequently we can claim that the GIM is not affected by the local effect of the earthquake.

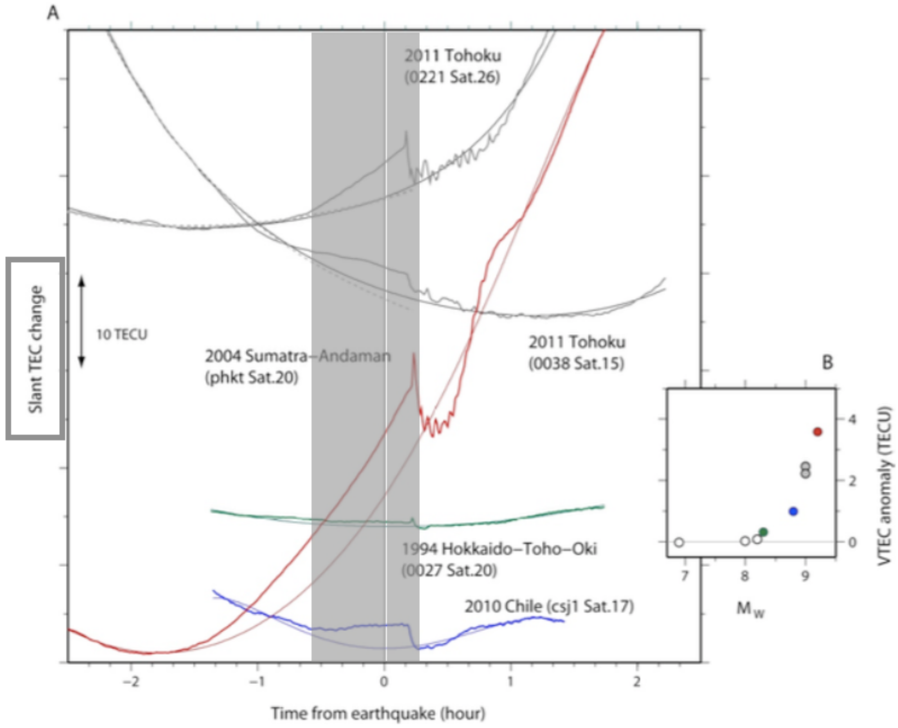

Figure 37: (A) sTEC changes and their models of the 2011 Tohoku, the 2004 Sumatra-Andaman, the 1994 Hokkaido-Toho-Oki and the 2010 Chile (Maule) earthquake. The horizontal axis shows the time from earthquakes. Dashed curves in gray for the top two time series show the models derived with data prior to the possible onset of the precursor (before 5.2 UT) and extrapolated to 5.2-6 UT. The gray zone is the the time window excluded from fitting. (B) vTEC anomalies immediately before the earthquakes as a function of their moment magnitudes. Colors correspond to those in (A). From:Heki (2011)

Heki (2011) finds the same behavior for three additional events: the 2004 Sumatra-Andaman, the 1994 Hokkaido-Toho-Oki and the 2010 Chile (Maule) earthquakes (Figure 37). The gray zone in Figure 37 shows the time window excluded from the TEC data to compute the polynomial fit and to define the unperturbed TEC. We highlight that the selection of this time windows is subjective and is based on the hypothesis that the ionosphere is not perturbed by the seismic event more than 40 minutes before and more than 20 minutes after the rupture.

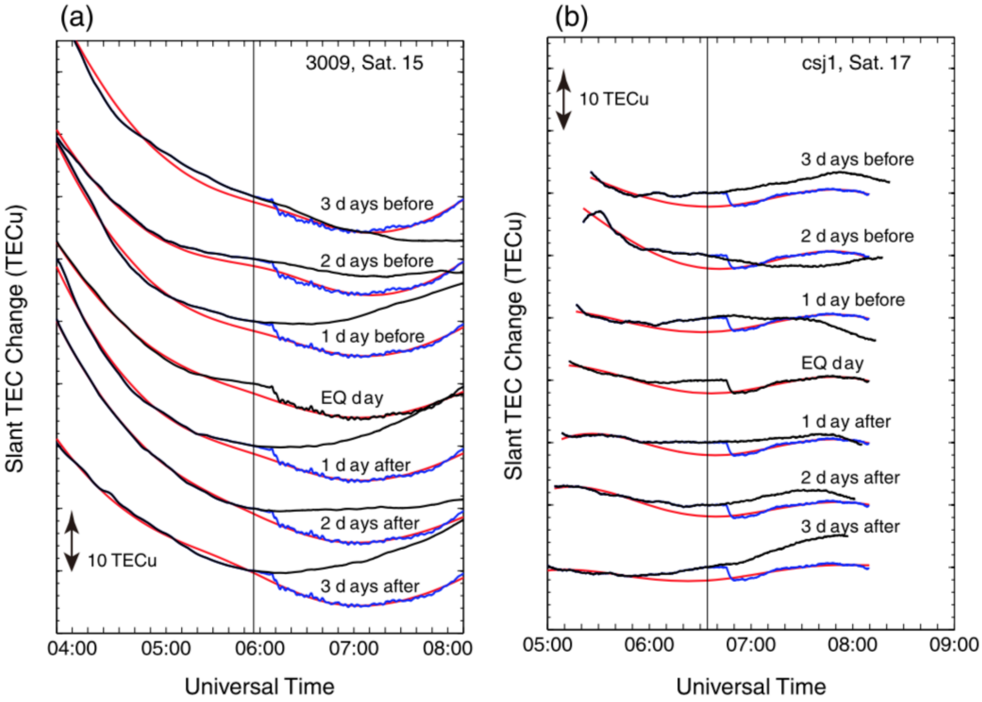

Figure 38: Slant TEC changes 3 days before and after the mainshock. Black, blue and red lines denote the original time series, the slant TEC time series of the EQ day after the mainshock and the reference curve by using the polynomial fit as in Heki (2011) (a) Tohoku EQ and (b) the Chile EQ. From: Kamogawa & Kakinami (2013)

Kamogawa & Kakinami (2013) used the three days before and after the earthquakes of Tohoku and Chile to differently define the unperturbed TEC and to support the hypothesis of the ionospheric hole (Figure 38). As the mean-daily value of the TEC is strongly affected by the solar radiation, they compared the TEC observed during the day of the seismic events with the TEC of the days surrounding the event by shifting the TEC curve of the days before and after at the TEC value observed at the time of the rupture. This approach is also subjective because it is already excluding the possibility of the enhancement before the earthquake.

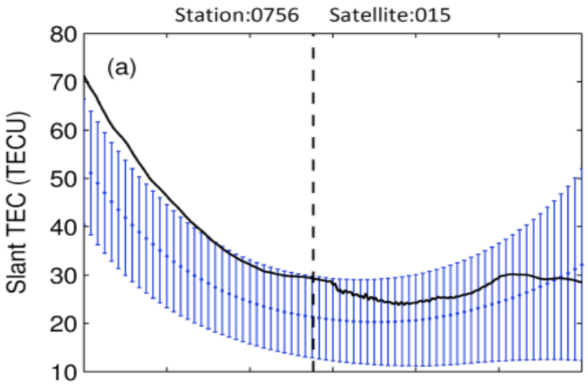

Figure 39: Superposed Epoch analysis for GEONET station 0756 in Japan and satellite 015. The time of the earthquake (5:46 UT) on 11 March is shown as the black dashed line. The black line is the day of the earthquake slant TEC and the blue dots represent the mean of 61 curves from ±30 days of the earthquake. The blue error bars are ±1 standard deviation from the mean. From: Masci et al. (2015)

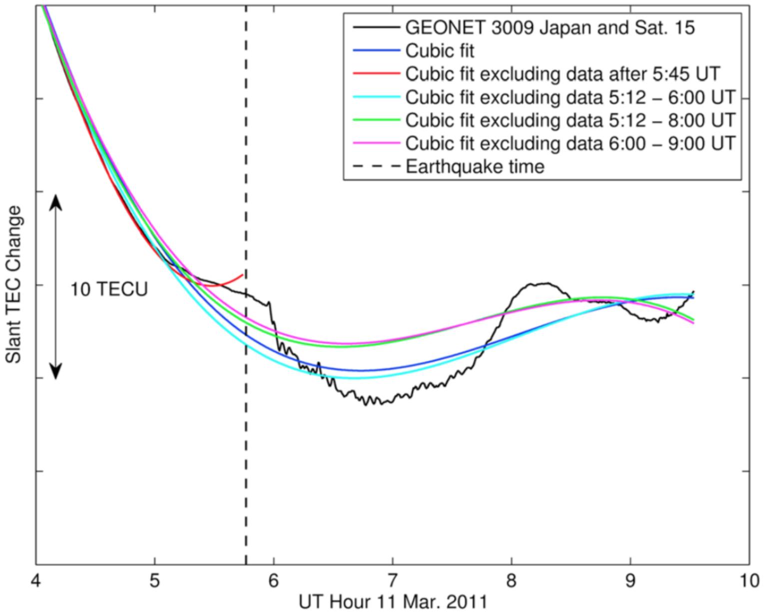

Figure 40: sTEC on 11 March 2011 for GEONET station 3009 in Japan and satellite 15. The time of the earthquake (5:46 UT) on 11 March is shown as the black vertical line. Cubic least squares fits to the sTEC with and without the preseismic and coseismic disturbance are shown. From: Masci et al. (2015)

Masci et al. (2015) used a more objective approach by comparing the slant TEC of the day of the Tohoku earthquake to the mean level of the 30 surrounding days. Figure 39 shows that the variations of the day of the earthquake lie within one standard variation of the surrounding 30 days and that therefore both the TEC enhancement as well as the hole can’t be distinguished from standard variations observed in the TEC. Masci et al. (2015) also did an analysis of the effect of the choice of the time window excluded to compute the polynomial fit used by Heki (2011) to define the unperturbed TEC (Figure 40). The choice of the excluded time window is interesting as it can clearly affect the fit of the data. In the case of the Tohoku earthquake several papers have reported perturbations in ionospheric TEC having large amplitude and exceptional time duration induced by the Tohoku-Oki main shock and/or the generated Tsunami (Astafyeva et al., 2013; Galvan et al., 2012; Rolland et al., 2011; Tsugawa et al., 2011; Occhipinti et al., 2013). These perturbations last more than two hours after the main shock. Therefore since Heki (2011) in his analysis excludes only data in the period of 5:12-6:00 UT and Heki & Enomoto (2013) exclude data during the period -40 to +20 minutes from the earthquake time, their fitting is very likely strongly affected by the earthquake-related perturbations that are present in sTEC data after 6:00 UT. Additionally, even if the enhancement of TEC before the seismic events is real, this enhancement is derived by comparison with a reference curve that can only be calculated after the analysis of the entire TEC observation by the satellite-station pair; in essence the reference TEC is calculated using up to few hours before and after the event. Consequently, using a polynomial fit it's not possible to highlight the enhancement in an operational real-time scenario to predict the earthquake.

Heki & Enomoto (2013) use additional data from ionosondes and magnetometers to confirm the existence of the precursory TEC enhancement by showing the simultaneous appearance of TEC, geomagnetic declination and changes in the critical frequency of the sporadic E layer. Utada & Shimizu (2014) further examined the geomagnetic declination changes paying special attention to spatial dependence which received little attention in Heki & Enomoto (2013). Their results suggest that the geomagnetic declination change is due to the ionospheric conductivity change caused by acoustic disturbance generated by the tsunami as suggested by Kakinami et al., (2012).

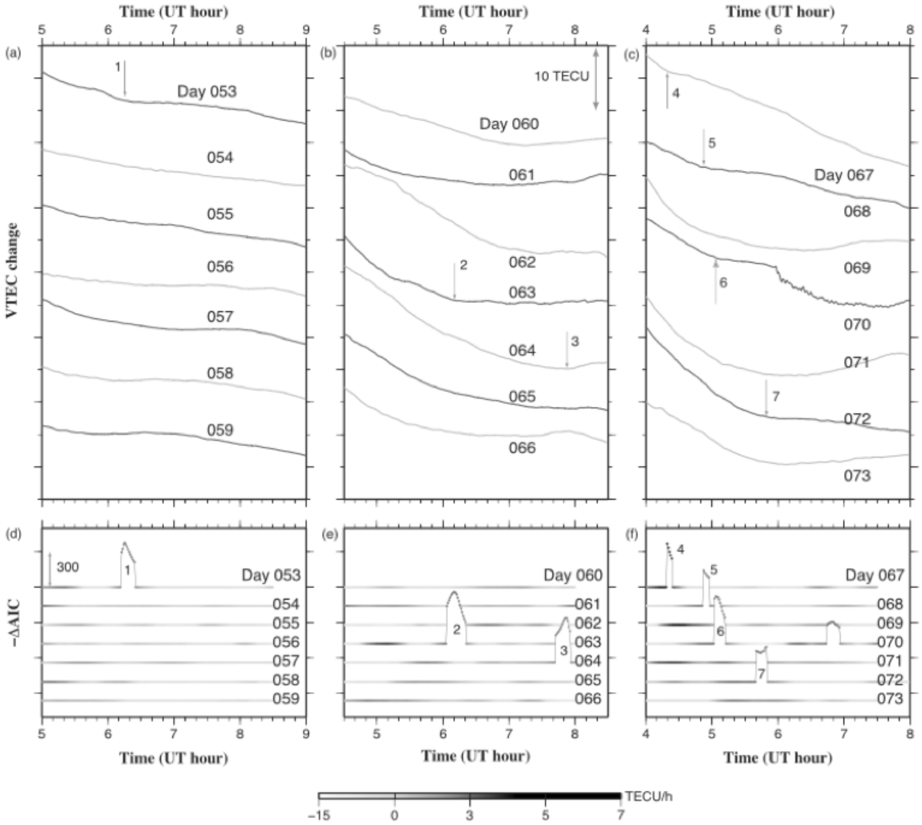

Figure 41: (a-c) VTEC time series for the three week period of the same station (3009) satellite (15) pair as used in Heki & Enomoto (2013). The geomagnetic activity was calm in the first week and more severe in the second and third week. By using the VTEC change rate six significant positive breaks (sudden increase of TEC rate) larger than 3.5 TECU/h in addition to the pre-seismic one on day 070 could be detected. The breaks propagate southwards and are considered to be parts of small-amplitude LSTIDs. From: Heki & Enomoto (2015)

As a reply to the criticism about the impossibility to use the TEC enhancement to predict seismic events in an operational scenario, Heki & Enomoto (2015) propose a new approach to identify abrupt increase in TEC rate (breaks) in absolute vTEC time series instead of the reference curves. Notwithstanding such breaks were detected for all recent M_w>8.5 earthquakes except the 2005 Nias earthquake (Cahyadi & Heki, 2013), Figure 41 shows that during three weeks around the Tohoku event seven such breaks were detected by Heki & Enomoto (2015) but only one correspond to the seismic event of Tohoku. This clearly proves that the proposed method to identify the abrupt increase in TEC before seismic events is not suitable for warning purposes.

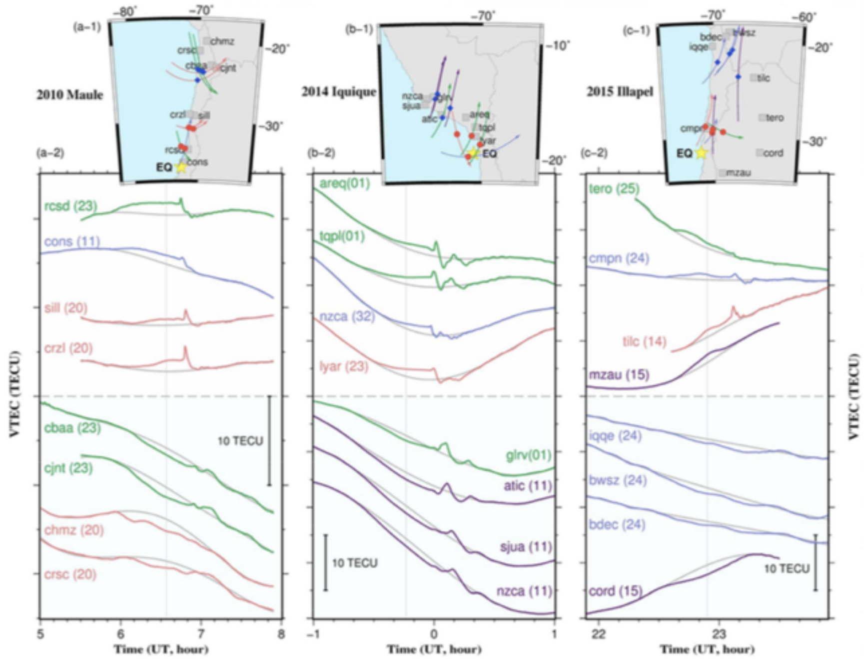

Figure 42: VTEC time series observed with eight station-satellite pairs (same colours for same satellites) showing preseismic enhancements and decreases. The gray curves are the reference models. The vertical gray lines indicate the earthquake occurrence times. The maps at the top show the positions of GPS stations (gray squares) and the SIP trajectories (red dots and blue diamonds indicate the earthquake time for stations showing enhancements and decreases, respectively) over the studied intervals. The yellow stars show the epicenters. From: He & Heki (2016)

Later on, He & Heki (2016) focus on three earthquakes in South America the 2010 Maule, 2014 Iquique and 2015 Illapel events. In this work authors highlight, for the first time, a next version of the TEC enhancement theory, introducing the idea that the enhancement of the TEC observed by GPS close to the epicenter becomes a depletion (negative variation) of the TEC in the far field, and follows the direction of the magnetic field line. The idea behind those new observations is that the electromagnetic dipole behavior of the source during the nucleation phase attract electrons of the ionospheric plasma to the dipole at the epicenter (creating the enhancement) along the geomagnetic magnetic line. Consequently this movement reduces the ionospheric plasma density (number of electrons) far away from the epicenter following the geomagnetic lines. It is also logic, in their hypothesis, that the enhancement of the TEC appear in the lower ionosphere and the depletion in the higher ionosphere. He & Heki (2016, 2018) explored the geometrical distribution of the supposed enhancement and depletion and we dedicate the section 3.2 to the subject. Anyway, both the enhancement and the depletion are calculated by comparison with a TEC unperturbed background based on the previously described polynomial fit. We will focus our analysis (Chapter 3.1) of TEC on the same events and same station-satellite pairs as used in He & Heki (2016) in order to exhaustively explore the limitations and the subjectivity of the polynomial fit to define the unperturbed background TEC variations.

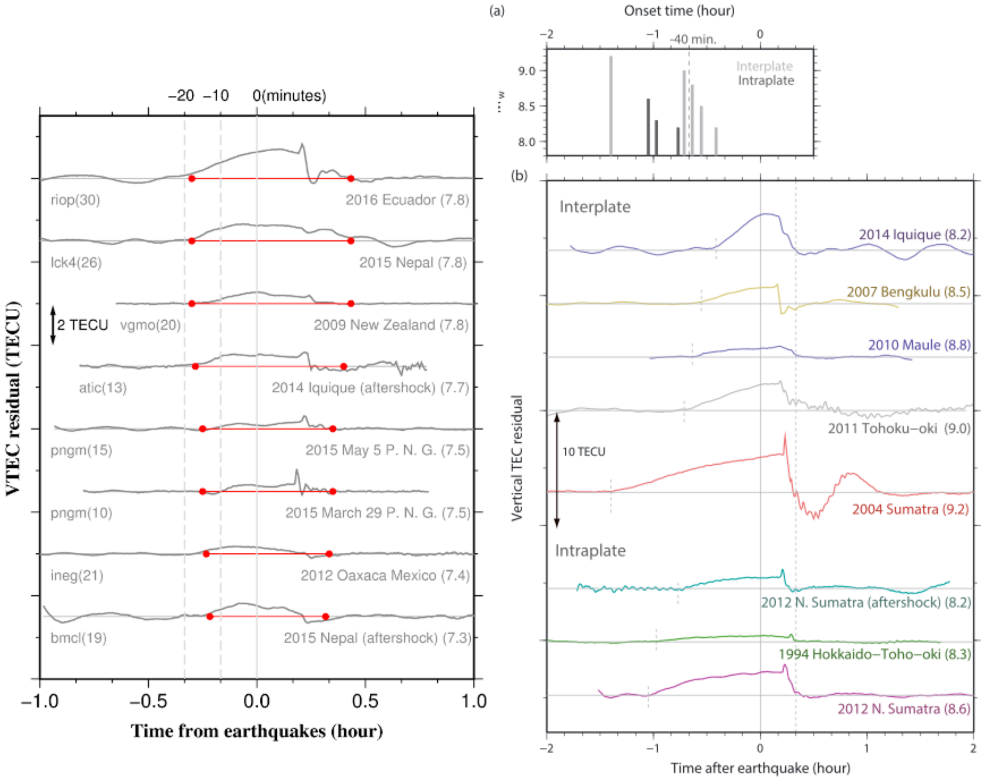

Figure 43: Left: Comparison of the residual vTEC plots for the eight earthquakes with possible precursors. To the left of the curve station names and satellite numbers are shown, to the right the M_w. Two vertical dashed lines indicate 20 and 10 minutes before earthquakes. The red lines indicate the exclusion windows used in defining the reference curves. From: He & Heki (2017) Right: (a) Comparison of the onset times of the precursory TEC enhancement for earthquakes with various M_w. Precursors tend to start earlier before larger earthquakes and intraplate earthquakes (dark gray). (b) The residual plot of vTEC for the eight earthquakes that are compared. Short vertical dashed lines indicate the times of positive breaks. From: Heki & Enomoto (2015)

He & Heki (2017) extend the analysis to earthquakes $M_w< 8.5$ and $M_w>7.0$ (Figure 43) and can detect anomalies preceding the earthquakes for 8 out of 32 earthquakes using the polynomial fit as reference curve. In order to validate the methodological approach to compute the polynomial fit to define the TEC unperturbed background, the authors used the so called L-curve method (Menke, 1989) to choose the degree of the polynomial fit (Figure 44, small inlets).

Figure 44 shows the variation of the VTEC residual depending on the degree of the polynomial fit used. Whereas the TEC enhancement showed by the residual seems stable for the earthquake in New Zealand, it strongly depends on the choice of the polynomial degree for the earthquake in Papua New Guinea. He & Heki (2017) defines the degree when RMS for the polynomial shows the largest drop as the most appropriate as also shown in the small insets in Figure 44.

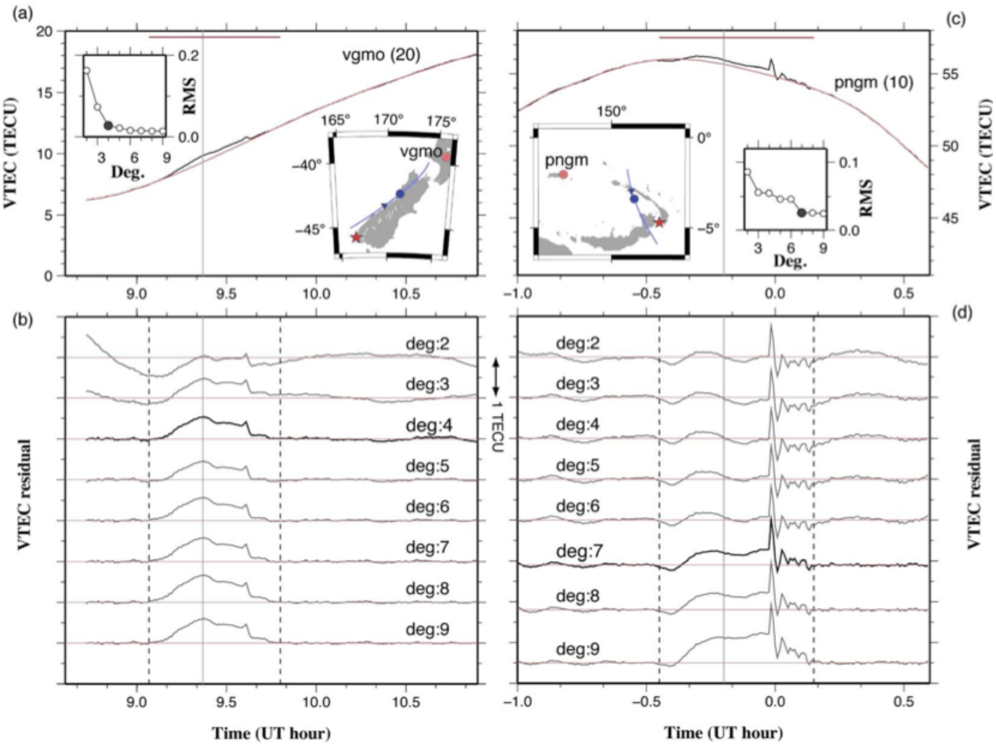

Figure 44: Fit of polynomials to the VTEC curves with excluding windows for (a and b) the 2009 July New Zealand EQ and (c and d) the 2015 March Papua New Guinea EQ. Polynomials of degree 2 to 9 are fitted to the curves excluding the window shown with dashed vertical lines. Small insets in (a) and (c) compare the RMS for these polynomials. From: He & Heki (2017)

Heki & Enomoto (2015) also write about a dependence of the pre-seismic enhancements on M_w showing that larger and longer TEC enhancements appear for larger magnitudes (Figure 43). This would implement that the size of an earthquake is known before it is happening. Common belief in seismology is rather that it is a spontaneous rupture and the duration and size not known until it stops. The pre-seismic enhancements being real and dependent on M_w would therefore revolutionize seismology. At the same time if the enhancement is just an artifact caused by the calculation of the reference curve it could be easy to explain that the produced artifact-enhancement is simply influenced by the hole after the earthquake. Indeed, larger earthquakes are creating larger co-seismic ionospheric disturbances and therefore explain the relation between the magnitude and the duration of the artifact-enhancement. In the following section, we try to introduce some constraints to better understand if the enhancement is an artifact or not.

3.1 The station LYAR

Starting from the results of He & Heki (2016), Eisenbeis & Occhipinti (in prep.b) analyzed the same South American earthquakes and tried to reproduce the same results for the pre-seismic enhancement as shown by He & Heki (2016). The processing of the TEC data was done as described before (e.g. Chapter 2.1.2).

Figure 45 shows the results of the attempt to reproduce the reference curve of He & Heki (2016) for the LYAR station used in their study (see Figure 42). We first used the full time series to compute the polynomial fit of 3rd and 5th degree as within the specifications of He & Heki (2016) to calculate the reference curve. The upper left plot in Figure 45 shows those results and in both cases the reference curve doesn’t resemble the TEC time series well and doesn’t show an enhancement at all. Using a polynomial fit of 9th degree, which would be out of spec according to the fitting done by He & Heki (2016) we can resemble the original TEC time series much better although no enhancement is visible but rather a hole after the earthquake (Figure 45, top right). Using the full time series for this station we find no evidence to support the theory of the TEC enhancement before the earthquake but can rather support the theory of an ionospheric hole forming after the earthquake. He & Heki (2016) in Figure 42 only shows a time window of 1 hour before and 1 hour after the earthquake. Consequently, we have changed the time window used for the fitting of the reference curve to 2 hours before and 1 hour 45 min after the earthquake (Figure 45, bottom left) and 2 hours before to 2 hours 45 minutes after the earthquake (Figure 45, bottom right). Whereas the longer time window of those in the bottom right plot now also resembles the hole

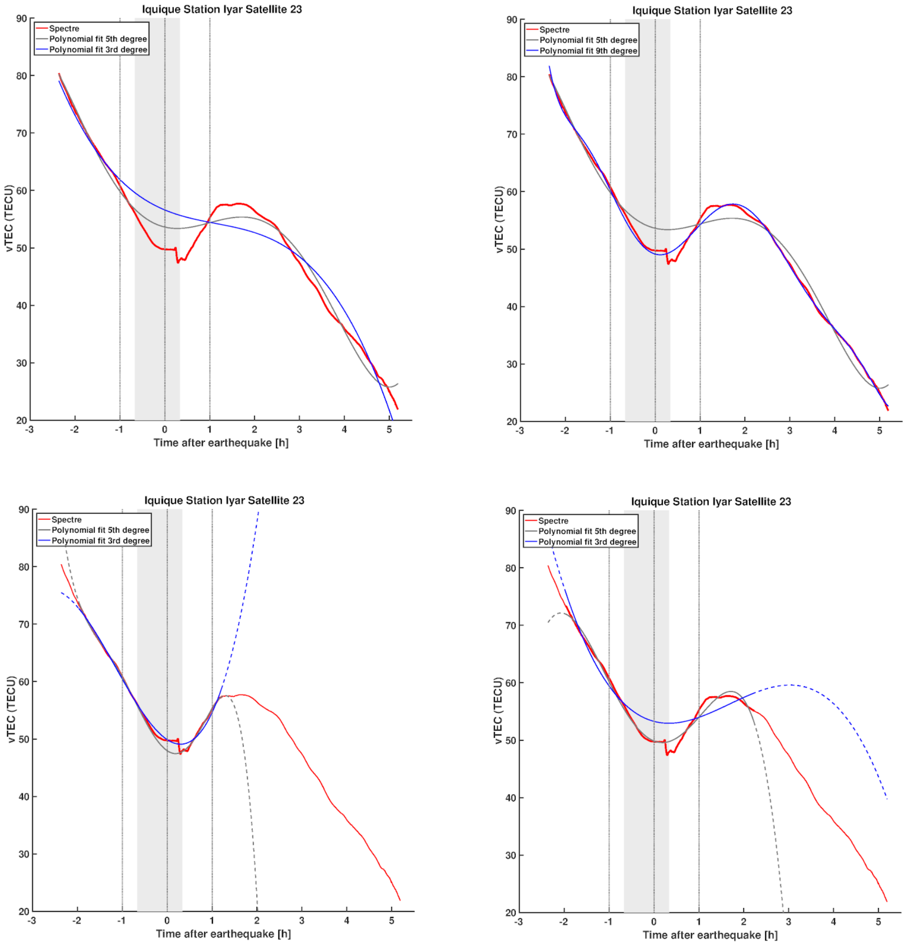

Figure 45: vTEC time series for station LYAR for the Iquique event. The gray area shows the time window excluded from fitting as in He & Heki (2016). The vertical dashed gray lines show the start and end of the time window shown in Figure 42. Red line is the original vTEC time series, blue and black lines show the polynomial fit of 3rd and 5th degree, respectively. Except upper right picture which shows 5th and 9th degree. Upper plots the whole time series is used for the calculation of the reference curve, lower left 2 hours before and 2 hours after the earthquake and lower right 2 hours before and 3h after the earthquake are used for the calculation of the polynomial fit.

after the earthquake, for the polynomial fit of 5th degree, we can only arrive to reproduce the fit of He & Heki (2016) by cutting the time window for the fitting even shorter (Figure 45, bottom left). Also for the shorter time window the polynomial fit of 3rd degree seems to support the hole after the earthquake theory. As can be seen in those attempts to reproduce the data of He & Heki (2016) within the specification given in their paper, we arrive to the same result only after putting some effort in trying different time windows for the fitting of the reference curve proving the subjectivity and the limit of the methodology to define the unperturbed reference TEC highlighting the enhancement.

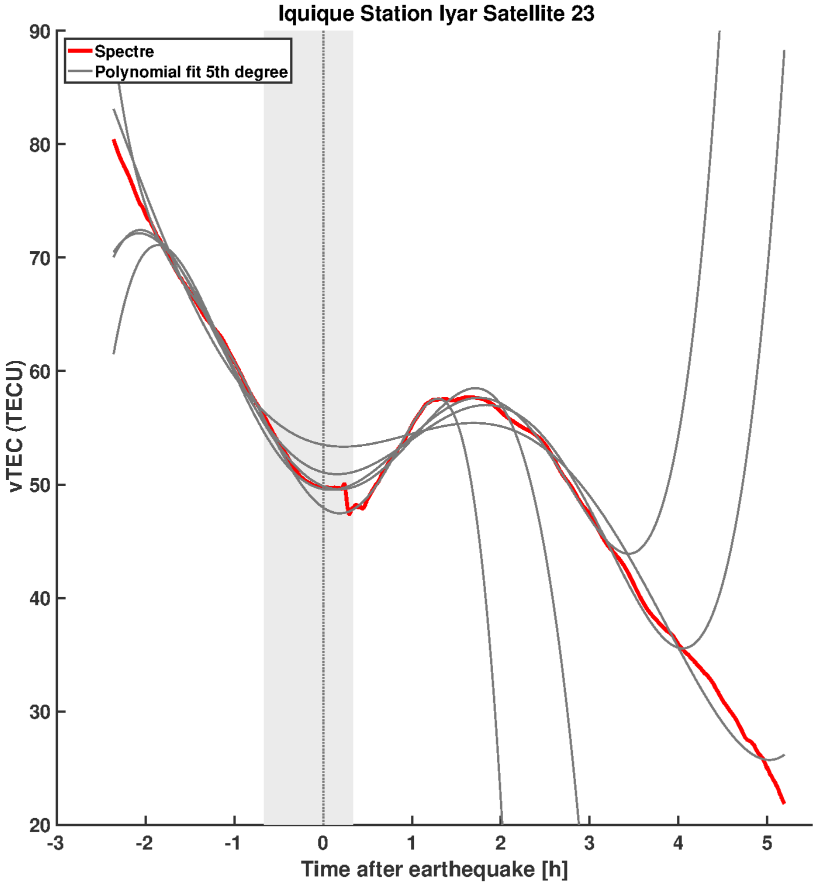

Figure 46: Same VTEC time series as in Figure 45 for station LYAR. Red is the original time series and in black are the curves of the polynomial fit of 5th degree using different time windows for the fitting. The gray area is again the time window excluded from the fitting as in He & Heki (2016). The dashed vertical line is the time of the earthquake.

Figure 46 shows the variations of the polynomial fit of 5th degree for one station satellite pair using different time windows for the fitting. For all the variations used, there is only one curve showing the pre-seismic enhancement and all other curves are either showing the hole after the earthquake or neither of them. Station LYAR clearly shows the difficulties in reproducing the pre-seismic enhancement shown in He & Heki (2016) and also shows that the residuals depend indeed on the degree of the polynomial but also depend highly on the chosen time window for the fitting.

3.2 3D theory of the ionospheric precursor

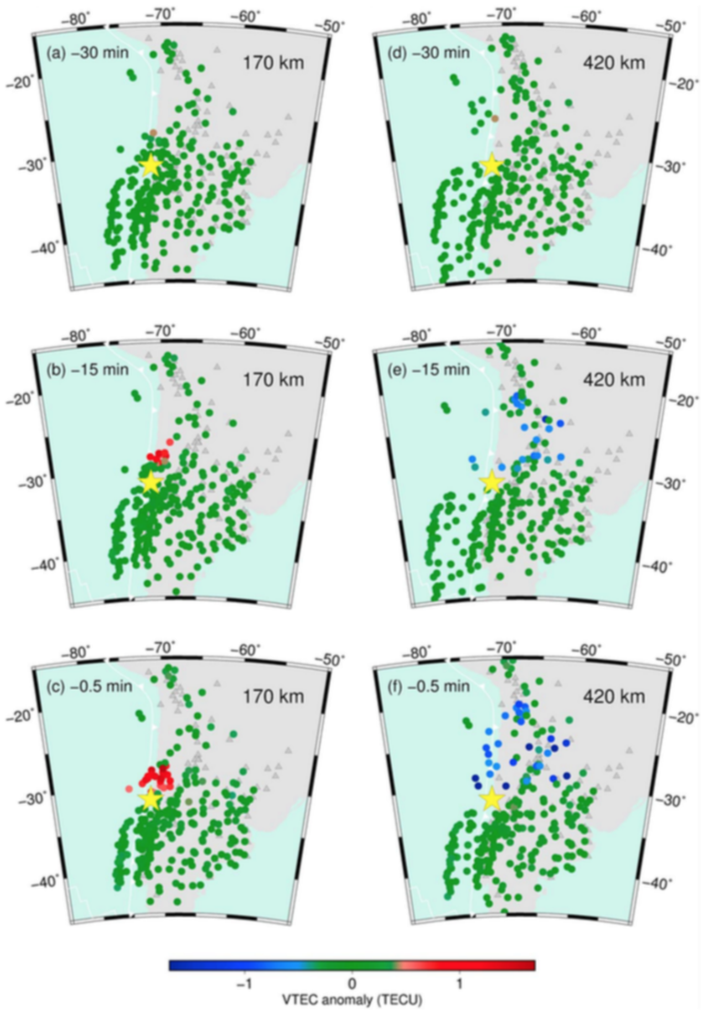

Figure 47: Distribution of SIPs showing preseismic positive/negative VTC anomalies at (a, d) 30 min, (b, e) 15min and (c, f) 30 sec before the 2015 Illapel earthquake. Data is derived using five satellites and using the ionospheric heights of 170 km (left) and 420 km (right) for the position of the SIPs. The yellow star shows the epicenter and gray triangles indicate GPS receivers. From: He & Heki (2016)

As mentioned above, He & Heki (2016) already tried to expand the analysis of the earthquake precursors to a more three dimensional approach (Figure 47). They nominally used different ionospheric heights for the calculation of the sub-ionospheric points (SIPs). Indeed, SIP coordinates depend on the assumed height of an ionospheric anomaly and multiple SIPs obtained with different satellite-station pairs are expected to converge when the assumed anomaly height is correct. In order to constrain the altitudes of the positive and negative anomalies. He & Heki (2016) tuned their altitudes so that they minimize the angular standard deviations of the SIPs of positive and negative groups. This leads to altitudes of ~170 km for positive and ~420 km for negative TEC anomalies.

He & Heki (2018) show results of a more robust 3-D tomography for the Illapel earthquake (Figure 49). The results of their tomography support the earlier obtained results about pre-seismic anomalies (He & Heki, 2016). This is not surprising as the input data for the tomography is the same used by He & Heki (2016) and it is obtained using the polynomial fit as reference curve which has been criticized before by several studies (e.g. Kamogawa & Kakinami, 2013; Masci et al., 2015, Eisenbeis & Occhipinti, in prep.b).

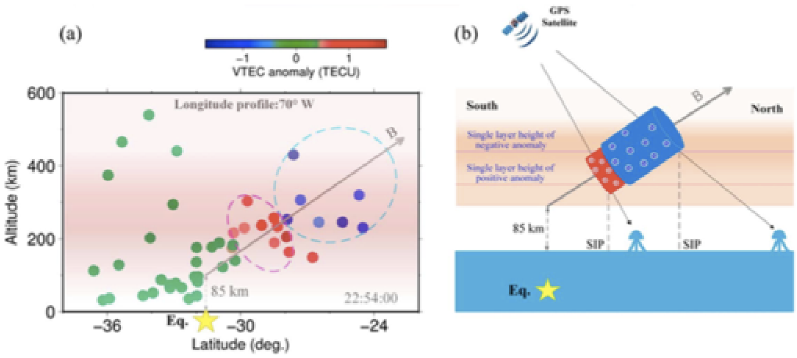

Figure 48: (a) Longitudinal profile at 70°W of vTEC anomalies immediately before the 2015 Illapel earthquake drawn using satellite 14 and 25. (b) Schematic illustration showing the 3D distribution of positive and negative anomalies. The thick gray arrow shows the geomagnetic field. The red and blue regions show the positive and negative electron density anomalies. The yellow star shows the epicenter. From: He & Heki (2016)

Figure 48 illustrates that the positive and negative anomalies found by He & Heki (2016) and shown in Figure 47 align along the geomagnetic field. As mentioned before, He & Heki (2016) suggest that positive charges from rocks under near-failure stress, possibly in the earthquake nucleation stage, cause the ionospheric anomalies immediately before large earthquakes. This means that, during the nucleation process, the fault acts as an electromagnetic dipole, producing electromagnetic perturbations which propagate into the ionosphere following the geomagnetic lines.

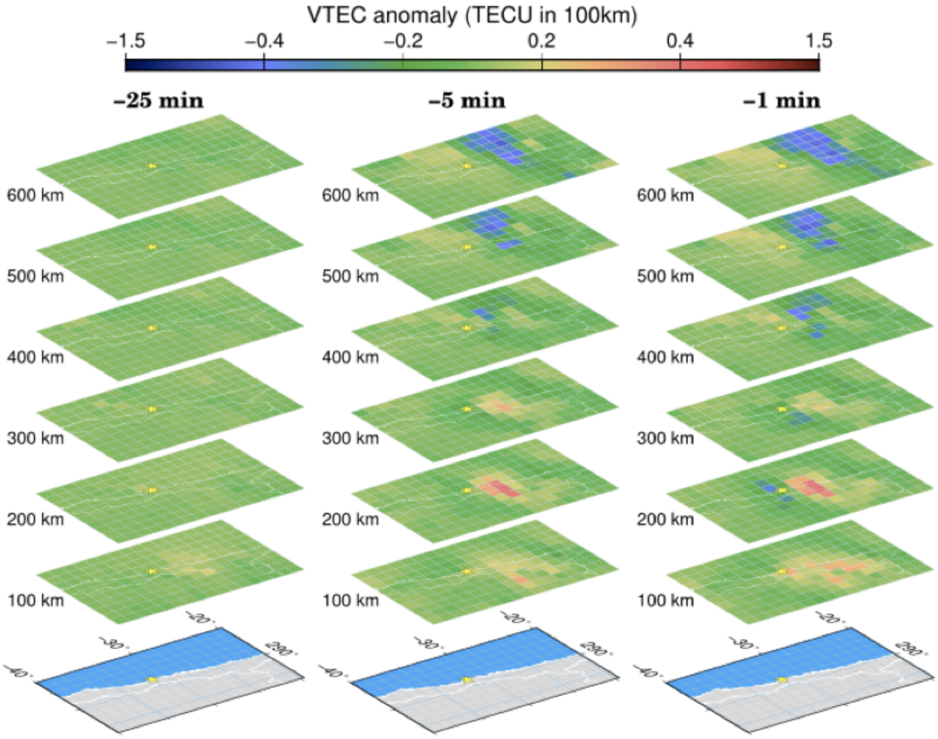

Figure 49: Electron density anomalies at heights from 100 km to 160 km before the 2015 Illapel earthquake derived by the 3-D-tomography at three epochs, 25 min (left), 5 min (middle) and 1 min (right) before the earthquake. The yellow star indicates epicenter. From: He & Heki (2018)

3.3 Conclusion

Heki (2011) sparked a debate about the possibility of a pre-seismic TEC enhancement 20 to 40 minutes before the earthquake. Several studies replied to his findings (e.g. Kamogawa & Kakinami, 2013, Utada & Shimizu, 2014, Masci et al., 2015) and mainly criticized his approach of calculating the reference curve using a polynomial fit by only excluding 20 minutes after the earthquake from the fitting process. Masci et al. (2015) also shows the variability of the cubic fitting for one station satellite pair. Eisenbeis & Occhipinti (in prep. b) picks up at the results from He & Heki (2016) for the South American earthquakes and by trying to reproduce the reference curve of He & Heki (2016) discovered that the vTEC residual depends highly on the choice of degree of the polynomial fit as well as of the length of the time window before and after the earthquake. Staying within the specifications given by He & Heki (2016) for the calculation of the reference curve

Eisenbeis & Occhipinti (in prep. b) could obtain mainly results that support the hole after the earthquake theory but for only one specific time window could also reproduce the fit of He & Heki (2016). This proves that the pre-seismic enhancement appears after a subjective tuning of parameters and consequently it could be an artifact

4 3D Ionospheric Tomography – new ideas and preliminary results

Tomography describes a method to reconstruct the volume of an object (e.g the human body in medical imaging or a geologic structure in geophysics) from measurements taken from outside the object. As with so many terms it derives from the ancient Greek words τομος (slice) and γράΦω (to write). The aim of a tomography is to visualize internal structures without destroying the object. Therefore it is an non-invasive technique. Various sensors (sound pressure, attenuation of a light beam, variation in velocity of polarization of seismic waves) can be used for measurements that contain information on the structure or the physical properties of the body and can be used to reconstruct it. Probably the main application of tomography is in geophysics or medicine but there are also may other possible fields where it can be used. An interesting example comes from the field of archaeology, where a tomography was used to determine the cause of death of the Pharao Tutanchamun (Hawass, 2005).

Mathematically a tomography can be divided in two steps. First of all the physical phenomena that are measured need to be described accurately in what is called the forward model. After this the physical properties of the object or rather a 3D distribution of them within the object can be determined based on the defined forward model.

A relatively simple example explaining the principle of a tomography is a Sudoku. The objective is to fill a 9 x 9 grid with digits so that each column, each row and each internal block contains all the numbers from 1 to 9. In a first step we can define the forward model as the sum of each row and each column. Knowing this, the inverse model is to complete the grid. More theoretically, we can treat a Sudoku board as a (9×9) matrix $S = (s_{ij})$, $s_{ij} = (v_{ij}, M_{ij})$ where the entries are ordered pairs of values $v_{ij} \in \{\emptyset, 1, . . . , 9\}$ and pencil-marks $M_{ij} \subset \{1, . . . , 9\}$. Note that we allow $\emptyset$ as a value and not zero – we will refer to this as the “null” value, since nothing will be shown there in a Sudoku puzzle. Also, we require that a cell has a non-null value if and only if the set of pencil-marks is nonempty. It is easy to verify in the following section that all methods preserve this. We say that a Sudoku board is solved when for each entry s_{ij}, $v_{ij} = \emptyset$ and $M_{ij} = \emptyset$, as well as the conditions as the typical row, column and block requirements are fulfilled. Each entry in our matrix corresponds to a cell in the Sudoku board, and to each cell ij we associate a neighbourhood $N_{ij} = R_{ij} \cup C_{ij} \cup B_{ij}$ the union of the cells in the i-th row, in the j-th column, and the block containing ij. If a cell ij is contained in the neighborhood of a cell kl, these cells are called neighbours (a symmetric, reflexive, non-transitive relation).

The numerical solution of a Sudoku is normally easier than the analytical one. A simple analytical solution is presented by seismological tomography. In the case of seismology, seismic waves provide by traveling through the Earth, for instance, information about its 3D velocity structure and therefore about the interior of the Earth (e.g. Rawlinson et al., 2010).

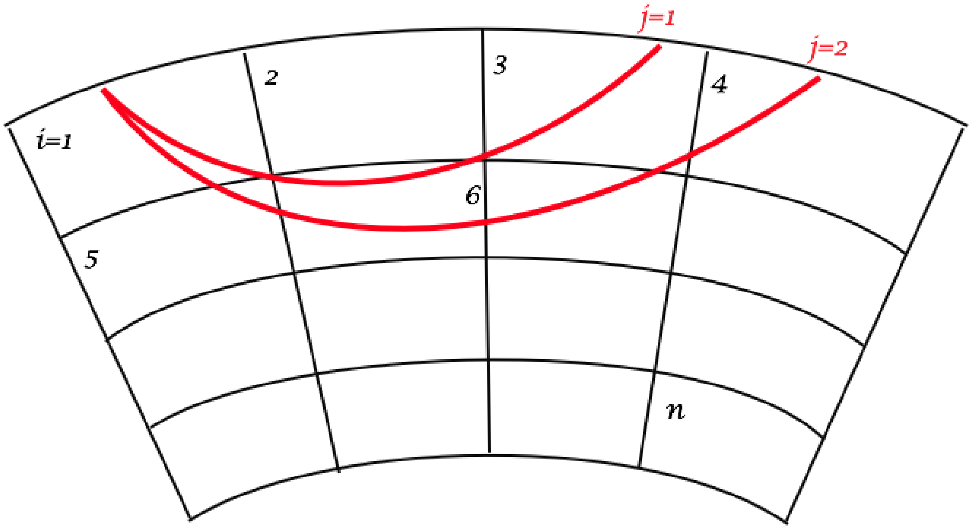

Figure 50: Schematic view of the parametrization of travel times of seismic waves in the earth

With the parametrization of seismic waves shown in Figure 50 the travel time T of ray j can be written as $T_j=\sum v_i^{-1} * ds_{ij}$ with v_i^{-1} being the slowness in cell i and ds_{ij} the path of the ray j in cell i. This can be written as T=A*V, with T a vector containing the travel times, A the Matrix containing all the ds and V the vector with the seismic slowness that are searched. Solving this inverse problem gives us $V=A^{-1}T$, allowing us to know the velocity field in all cells or at least the cells crossed by a large number of rays.

In medicine the use of x-rays (λ = 0.01 – 10 nm) is an example for the use of tomography. X-rays are attenuated while traveling through the body of the patient and lose intensity. Sending the x-rays from different angles and different directions gives information about the interior of the patient and can help to look at specific organs or bones without the need of a surgery.

The methodology of a tomography can also be used on the ionosphere as there are electromagnetic waves traveling through it as well as being refracted due to the existence of free electrons. Comparing the travel times of those waves to an a priori ionospheric model can be used to reconstruct the electron density distribution (e.g. Roy et al., 2014). Since GNSS systems offer widely available data from dense networks it is most often used in modern ionospheric tomography as will be explained in the following parts.

4.1 GNSS ionospheric tomography

Initially GPS was developed for military use only but nowadays it has several military and civilian applications. Since GPS data became available for scientific applications it can be used for ionospheric tomography. Figure 51 illustrates the principle of ionospheric monitoring and specifically here GPS tomography. As already mentioned, the GPS satellites emit two signals using two different frequencies (f_1=1.575 GHz and f_2=1.227 GHz) that traverse the ionosphere and are recorded at the ground station. Other GNSS systems like GLONASS or Galileo work basically the same way using slightly different frequency bands or changing frequency for each satellite like GLONASS.

As described before EM waves are perturbed when traveling through the ionosphere by the free electrons being present. The GNSS receivers on the ground measure the phase delays of the signals which are induced by the ionospheric refraction. This is also called the ionospheric delay. Between the two signals of the two different frequencies there is a phase difference $\Delta\Phi$ that correlates to the TEC which is the integral of the electron density along the path of the ray fro the ground station to the satellite by

$$\Delta\Phi = \left(\frac{1}{f_1^2} - \frac{1}{f_2^2}\right) \int N_e ds \tag{26}$$

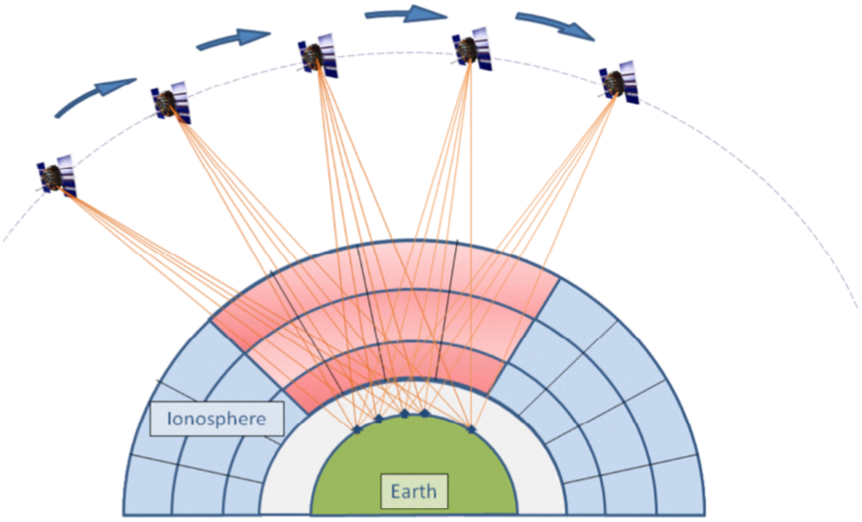

Figure 51: Principle of GPS tomography. The GPS satellite orbiting around the Earth is emitting signals that are measured at several receivers on the ground. The measured sTEC can be inverted for the local electron density perturbation in the red area of the ionosphere.

The sum of the electron density N_e along the raypath is the slant TEC, where ds is the partial element of the raypath between the satellite and the station. An estimation of the local electron density distribution can be obtained using the measurements of TEC and a priori model of the ionosphere. With this method it is possible to create a full multidimensional image. This is an advantage compared to other measuring techniques. The methodology can be written similarly to what has been shown above for seismic waves. For a grid in the ionosphere of n cells the TEC of ray j can be written as $TEC_j=\sum Ne_i * ds_{ij}$ with Ne_i being the electron density in cell i and ds_{ij} the path of the ray j in cell i. This can be written as $TEC=A*N_e$, with TEC a vector containing the total electron content, A the Matrix containing all the ds and N_e the vector with electron densities we want to obtain. Solving this inverse problem gives us $N_e=A^{-1}$ TEC. This is explained in more detail later in this Chapter.

Austen et al. (1988) did a first test of an ionospheric tomography using synthetic data for real satellite station combinations. In using the SIRT (simultaneous iterative reconstruction technique; Gilbert, 1972) he successfully showed the feasibility of an ionospheric tomography by GPS by creating two vertical cross sections of electron density. Before the first experimental results were reported, different other numerical tests have been carried out trying different algorithms for image reconstruction (Raymund et al., 1990; Raymund, 1994).

Andreeva et al. (1990) published the first experimental results for TEC data used in a tomography. They used a constellation of three stations in Russia and were able to reconstruct a two dimensional cross-section. This was the start of a wide use of GPS-based computerized ionospheric tomography to investigate the spatial and temporal variations of structures in the ionosphere (Hansen et al., 1997; Hajj et al., 1994; Hernandez-Pajares et al., 1998; Bust et al., 2004; Garcia & Crespon, 2008; Ma et al., 2005; Yizengaw et al., 2005; Wen et al., 2007). In addition, with the installation of global (e.g. IGS) and regional (e.g. GEONET in Japan) ground-based GPS networks ionospheric tomography was feasible worldwide. In Europe (Mitchell & Spencer, 2003), Russia (Kunitsyn et al., 1994), Antarctica (Heaton et al., 1996), China (Wen et al., 2007) as well as the polar caps (Pokhotelov et al., 2011).

A big advantage of the use of TEC data is the huge amount of data available with numerous networks on the ground and multiple satellites. Nevertheless ionospheric tomography is an ill posed problem. Generally datasets can be contaminated with noise or an incomplete sampling of information and therefore the inversion can be ill posed. This often leads to unstable solutions (due to the sensitivity to small data changes) and solutions being not unique (more than one possible reconstruction fits the observed data).

Since the development of GPS, a lot of different reconstruction algorithms were tested for ionospheric tomography to address these problems of instability and non-uniqueness. Kersley et al. (1993), Heaton et al. (1995), Mitchell et al. (1995), Pryse et al. (1995), Vasicek & Kronschnabl (1995) used the iterative MART (Multiplicative Algebraic Reconstruction Technique; Gordon et al., 1970) algorithm. This algorithm modifies the background ionosphere until the difference between measured and calculated synthetic TEC are acceptably small. The ART (Algebraic Reconstruction Technique) incorporates some a priori information on each pixel of the ionospheric grid and was used by Kunitsyn et al. (1994). For this inversion an a priori model with information about the ionosphere is used which leads to the problem that for the cells without any rays crossing it, the solution depends strongly on the input model. As an improvement for this Wen et al. (2010) proposed the CART (constrained algebraic reconstruction technique) algorithm. In this case the cells not crossed by rays use information from neighbouring cells instead of relying solely on the input model. This was validated with simulations of synthetic data as well as a tomography of real data over China. Kunitake et al. (1995) successfully reconstructed TEC over Japan in a magnetically disturbed period using a modified version of singular value decomposition

Data from different measurements like for example radars is a good opportunity to verify the results of the tomography. Pryse & Kersley (1992) were the first to compare the results of a tomography that was using two stations in Scandinavia with the results of the EISCAT radar. Following this first attempt to use radar data for validation of an ionospheric tomography by GPS data, other studies also implemented EISCAT as verification of tomography results over Scandinavia (Nygren et al., 1997; Walker et al., 1997).

Another possibility to validate the tomography is to compare the results to ionosonde data, particularly peak electron densities and the altitude of the layer of maximum electron density. By doing a tomography over Europe at mid-latitudes Fehmers et al. (1998) found that their results undervalue the maximum electron density $N_{e,\ max}$ by 20% and overvalue the altitude of the layer of maximum electron density between 80 – 200 km. Dear & Mitchell (2007) also compared their tomography results to ionosonde data. They used the MIDAS (Multi-Instrument Data Analysis System) algorithm for the tomography and could observe that the peak of the electron density is underestimated by 15% for synthetic data and up to 40% for real GPS data. This underestimation is explained by them with the simplified set of basis functions which used in the reconstruction algorithm. They also improve their results by including data from two ionosondes (e.g. F_2 peak height) as input in the reconstruction algorithm which gives results corresponding better with the ionosonde data.

Tomography has also been used to image TIDs (e.g. Cook & Close, 1995; Markkanen et al., 1995; Pryse et al., 1995).

Even with the high number of measurements available with GPS which makes it a powerful tool for studying the ionosphere, there are theoretical limitations of ionospheric tomography using the GPS configuration of satellite to station paths. These limitations are discussed by Yeh & Raymund (1991) and Na & Sutton (1994). Datasets are not only limited spatially and temporally by the setup of the networks. There is also a limitation by the finite sampling frequency and viewing angles of the stations being limited. This can lead to an incomplete dataset. Additionally many studies assumed an invariant ionosphere during the measurement. The rather high frequency of the GPS signals limits its sensitivity to the peal electron density and due to the constellation of the satellites and stations horizontal raypaths are missing. This leads to a poor vertical resolution of the tomography.

To overcome these difficulties in the reconstruction of the ionosphere mainly three approaches have been tried. Heaton et al. (1995) could improve the vertical profiles by implementing scaled ionograms. Kersley et al. (1993) additionally used ionosonde data and could also improve the results by implementing it into the reconstruction algorithm. Markkanen et al. (1995) incorporated peak heights of the ionospheric layers as a priori information in the tomography and applied a Bayesian approach to synthetic data.

A different approach is to fill the gap in information with vertical profiles from ionospheric models. Fremouw et al. (1992) applied a set of vertical orthonormal functions to image the vertical profile. A disadvantage of this method is that ionospheric models are often not very accurate and mostly fail to model the day to day variations that can be very strong. This leads to the results of tomography using vertical profiles of ionospheric models often being not very accurate and not necessarily improving over the use of GPS data only. Also tests with a model independent algorithm which was thought to compensate the lack of horizontal raypaths show moderate success (Fehmers et al., 1998)

The third approach we will present here to improve the solution of the GPS tomography is a joint inversion of measurements from different sources, e.g. from ionosondes (as mentioned above), radar (also see the Chapter 4.2 which is dedicated to this) or occultation measurements. For instance Rius et al.

(1997) showed included occultation data in his inversion of GPS TEC which has improved the vertical resolution. This again showed that the use of ground data alone is insufficient for a good vertical resolution, They also showed that a joint inversion improves the overall resolution of the ionospheric image as the different measurement are sensitive to different areas of the ionosphere..

Fridman & Nickisch (2001) did an interesting test in combining GPS TEC measurements from several station in the Caribbean with vertical and backscatter ionograms from an OTH radar in a simultaneous inversion. They could obtain a smooth 3D model of a fixed region. Notwithstanding this first test combining together from OTH radar data and GPS TEC data is interesting, the inversion is only limited to the leading edge echo curve. This means it contains, for each frequency, only the information of the ray with minimal group delay. In the following section (4.2) we describe a more accurate method to inverse OTH radar measurement. Fridman et al. (2006) and Fridman et al. (2009) developed a 3D real-time reconstruction method of the ionosphere (GPSII) where they combine several measurements. Their method can be used with several inputs including TEC data from ground and space GPS receivers (absolute and relative) also including occultation, vertical TEC from altimeters, vertical electron density profiles from ionosondes and in situ measurements on LEO satellites such as CHAMP. In their updated version of the methodology Fridman et al. (2012) also allow for the use of backscatter sounding data. Their method is applied to a fixed geographical region and delivers a dynamic ionospheric model. The results are consistent with backscatter data (using the leading edge only), vertical sounding data, as well as with TEC data from a number of GPS/LEO rmeasurements.

A big improvement in the resolution of ionospheric tomography by GPS was the growing number of available stations and networks. This lead to attempts to reconstruct the time evolution of the ionosphere in 3D. In his study to reconstruct the ionosphere over Scandinavia for a full month van de Kamp (2013) used GPS data from the GEOTRIM network in Finland and imaged the ionosphere in a three dimensional resolution for December 2006. To constrain the vertical profile they use data from the EISCAT radar The use of EISCAT data instead of Chapman profiles improved the resolution of vertical profiles or irregularities in the ionosphere.

We would like to test the idea of a joint inversion of GNSS-TEC and OTH radar data as described in the following part.

4.2 Joint inversion OTH radar/ SuperDARN/ GNSS-TEC

Classic radars operate in a way that they emit EM waves which are scattered when they hit a target, e.g. ionospheric disturbance, and then receive part of this returning energy at a receiver in the same position as the emitter. The direction of the radar emission in combination with the travel time of the wave allows to locate the range where the wave was reflected. Additionally for moving objects the velocity can be determined by using the doppler shift of a backscattered signal. This explains the origin of the acronym RADAR from RAdio Detection And Ranging. This classic radar methodology is limited by the curvature of the earth in particular as well as other obstacles. To detect a target at longer distance e.g. more than 1000 km over-the-horizon (OTH) radars were developed.

OTH radars normally operate in the frequency band of 3 – 30 MHz. Ionization increases until 300 km altitude and therefore EM waves are bent towards the ground. Like this distances up to thousands of kilometres away and beyond the geometric horizon can be reached. Figure 52 shows the difference methodologies of a classic radar and an OTH radar. Headrick & Anderson (2008) describes the principle of OTH radars in detail. In case of a single path, meaning only one reflection in the ionosphere an OTH radar can reach distances of roughly 2000 km whereas for multi-path this can be extended to up to 4000 km

There are two types of OTH radars, monostatic and bistatic. Monostatic radars have the emitter and receiver at the same location, so the signal is reflected in the ionosphere and then backscattered from the ground and returning on the same path to the receiver. For bistatic radars the emitter and receiver are located in different places. This wave contains information about the medium it passes through and therefore can be used to study the structure of the ionosphere.

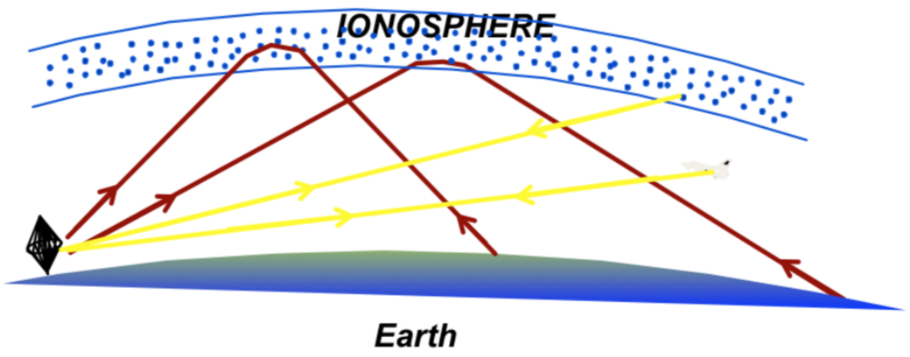

Figure 52: Schematic representation of OTH (red) and classical radar (yellow).

4.2.1 Worldwide development of OTH radars

The quest to build OTH radar systems started in times of the Cold War as it became important to be able to reach targets without limitation from the Earth's curvature. We will describe some of these systems in this chapter and for more information Liu (2007) describes them exhaustively.

Unsurprisingly the US played a big role in the development of OTH radars. The first experiments with monostatic radars were held in the 1950s by the Naval Research Laboratory in Chesapeake, Virginia. They built the MADRE (Magnetic Drum Radar Equipment) which got its name from the fact that the data was recorded on magnetic drums. In central California the WARF (Wide Aperture Research Facility) radar was the first experimental bistatic radar. It showed major improvement compared to MADRE (Thomson, 2003). The first operational radar was known as Cobra Mist but was running for only two years as the performance regarding range and azimuth resolution was poorer than expected. This was followed by a second operational OTH radar, the OTH-B (Over-the-Horizon-Backscatter). Thess were actually two systems of bistatic radars, at the east and west coast of the US. The west coast system had its emitter in Christmas Valley, Oregon and the receiver in Tulelake, California. It has been removed in 2007. For the east coast the emitter was located in Moscow, Maine and the receiver in Columbia, Maine. The Us systems are described in detail in Thompson (2003).

Additionally the US Navy developed its own system. The original purpose was to track ships and aircraft over the ocean. So the first prototype was installed on the Aleutian islands to monitor the Russian coast between 1991 and 1993. It was named the ROTHR (Relocatable Over the Horizon Radar). After the end of the Cold War it has been moved to Virginia (ROTHR-VA) to track illegal drug trade. Additional systems were installed in Texas and Puerto Rico to control drug smuggling in Central America and the Caribbean.

Obviously the Soviet Union were also developing their own systems. The first was the DUGA-2 radar which started operation in 1971. The succeeding system was named STEEL YARD. It was nicknamed Russian woodpicker as it emitted loud and repetitive pulses. The Russians announced a new system in 2015 (Karpenko, 2014).

Also Australia had its own projects. In the 1960s they've started the operation of the Jindalee radar which is a bistatic radar located in Alice Springs in central Australia. It was later in 2003 combined with two additional systems. The name of this new system is JORN (Jindalee Operational Radar Network). More details about the Australian OTH radar projects can be found in Colegrove (2000).

China, Japan and Iran are also in possession of OTH radar systems but little is known about them.

There are two OTH radars in France. One of them is located in Valensole and operated by the University Pierre et Marie Curie (Six et al., 1996) and another one (Nostradamus) south of Paris. It is operated by the Office National d'Etudes et de Recherche Aerospatiale (ONERA) and other than most of the systems described above it is monostatic. So the antennas for the emission and the reception are co-located. The OTH radar system consists of several antennas of 7 m height and 6m width. The antennas are arranged in a kind of star-shap which gives the opportunity for a 360° coverage in azimuth. The biconical nature of the antennas ives the option to control the elevation of the emitted EM wave.

4.2.2 The SuperDARN network

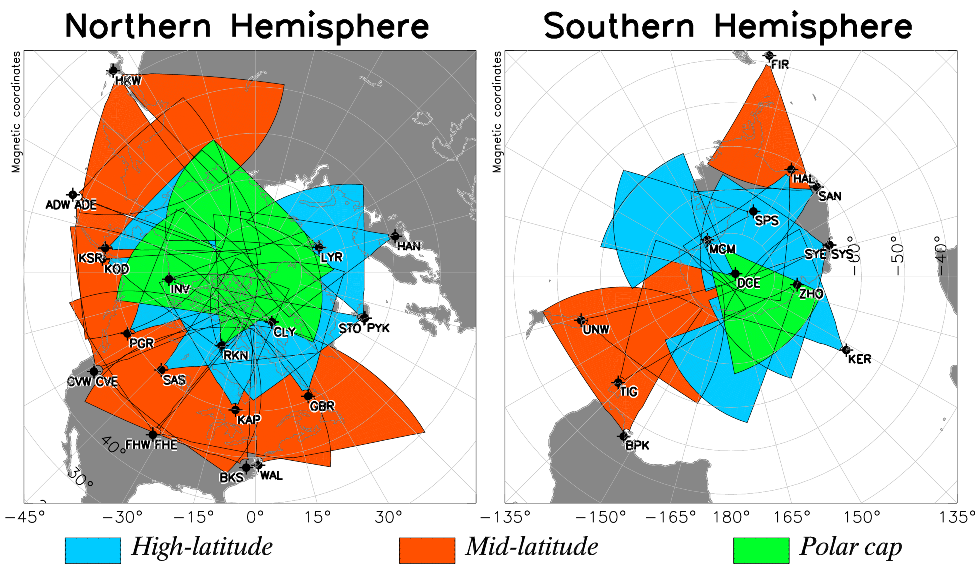

Figure 53: Currently operational SuperDARN radars and their fields of view in the northern (left) and southern (right) hemisphere. From: http://vt.superdarn.org/tiki-index.php

Super Dual Auroral Network (SuperDARN) is a global scale network of High Frequency (HF) and Very High Frequency (VHF) radars, constructed by engineers and scientists of a dozen different countries. SuperDARN radars were built for research of the polar ionosphere. Therefore they are located at mid (30º-55º) to high (>55º) latitudes with their fields of view pointing towards the polar regions. It is the main objective of the project to have continuous observations of ionospheric disturbances and their motion in mid and high latitudes. (Greenwald et al., 1995).

Figure 53 shows all the operational SuperDARN radars and their field of view. In 2019 the network contains of 23 radars in the Northern Hemisphere and 13 in the Southern Hemisphere which are all continuously operating. The radars can sound regions of polar oceans which can help understand climate variability. The azimuthal resolution at a frequency of 12 MHZ is approximately 4º (Greenwald et al., 1995).

SuperDARN has been successfully used to investigate the ionosphere, magnetosphere and thermosphere and their coupling. The measurements of the radars are the backscattered energy, the line-of-sight Doppler velocity and the width of the Doppler spectrum (Baker et al., 2010). Using the Doppler spectrum of ionospheric disturbances the properties of the ionospheric electric field can be derived and also the plasma convection velocity can be calculated. Ionospheric convection maps are created every 1-2 minutes on a global scale. This can be of good use to investigate the energy transfer of solar winds into the ionosphere and magnetosphere.

There are also other objectives of SuperDARN radars in science. For example investigation of large scale traveling ionospheric disturbances, plasma motion in the ionosphere, ionospheric irregularities in general and the plasma structures at high-latitude. In addition, the roughness at the Earth's surface including ocean waves and ice-cover can be investigated with SuperDARN. In this case it uses the fact that the backscattered energy is higher at water-covered areas than over land and weakest for ice covered surfaces.

4.2.3 Ionospheric tomography by OTH radar

Roy et al. (2014) presented a new tomographic method of the lower ionosphere (≤300 km) based on the full inversion of over-the-horizon (OTH) radar data. The OTH radar takes advantage of the refraction of the ionosphere. As explained in the chapter before the emitted signal is reflected in the ionosphere and can reach the ground beyond the geometric horizon. The signal is backscattered from there and travels back to the receiver following

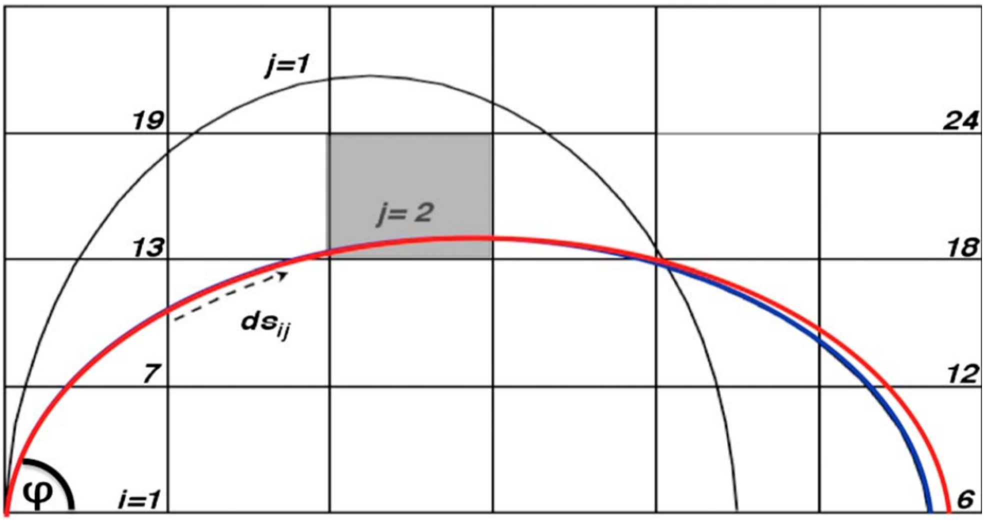

Figure 54: Schematic representation of the parametrization of j rays with elevation angle φ and i cells with the raypath deflection induced by a localized perturbation (e.g. grey cell) producing a perturbed ray (red) compared to the unperturbed ray (black). From: Roy et al. (2014)

the same raypath (Figure 54). The received signal contains all information about the propagating medium. It is emphasized that the point where the signal is backscattered is not fixed and changes with the ionization of the propagating medium.

Two different methodologies have been used for the ionospheric tomography by OTH radars and therefore to estimate the properties of the ionosphere (the critical frequency f_c, the peak height and the semi-thickness of each layer) They either tried to fit the observed travel times of leading edge with a quasi-parabolic ionospheric layer (Rao, 1974; Bertel & Cole, 1988; Ruelle & Landeau, 1994;Landeau et al., 1997) or used ray tracing for a numerical simulation of the leading edge (Coleman, 1998; Fridman & Fridman, 1994; Fridman, 1998).

All the mentioned studies of tomography by OTH radar used only the leading edge echo curve. A big disadvantage of this is that a lot of information present in the data is ignored. Roy et al. (2014) tried to overcome this limitation. To do so they use the ray-tracing tool TDR (Occhipinti, 2006) to calculate the synthetic propagation time. This code uses the NeQuick model (Radicella & Leitinger, 2001, see Chapter 1.4.2) and the elliptical WGS84 coordinate system (National Imagery and Mapping Agency, 2000) to trace the rays, For the ray tracing they numerically solve the Eikonal equation and describe the propagation of the rays in a medium by a fourth-order Runge-Kutta method. In the inverse problem the electron density in the ionosphere is directly estimated from the difference between the calculated and measured propagation time as already described in Chapter 4.2.5. Some OTH radars can’t discriminate the polarization of the wave, so to be able to be applied to all OTH radars, the ray tracing tool neglects the magnetic field. To improve the methodology they developed the v&r method that takes into account both the speed variation due to the ionospheric anomaly as well as the fact that the exact point where the ray is backscattered isn’t known. Figure 55 shows the results of Roy et al. (2014) for synthetic tests with a checkerboard perturbation for the Nostradamus radar in France. Shown are results for three different methods: the frozen ray shows the best resolution theoretically possible with the used ray coverage; the v method is taking into account only the perturbation of the speed of the ray; the v&r method that is taking into account both the speed variation and the raypath deflection.

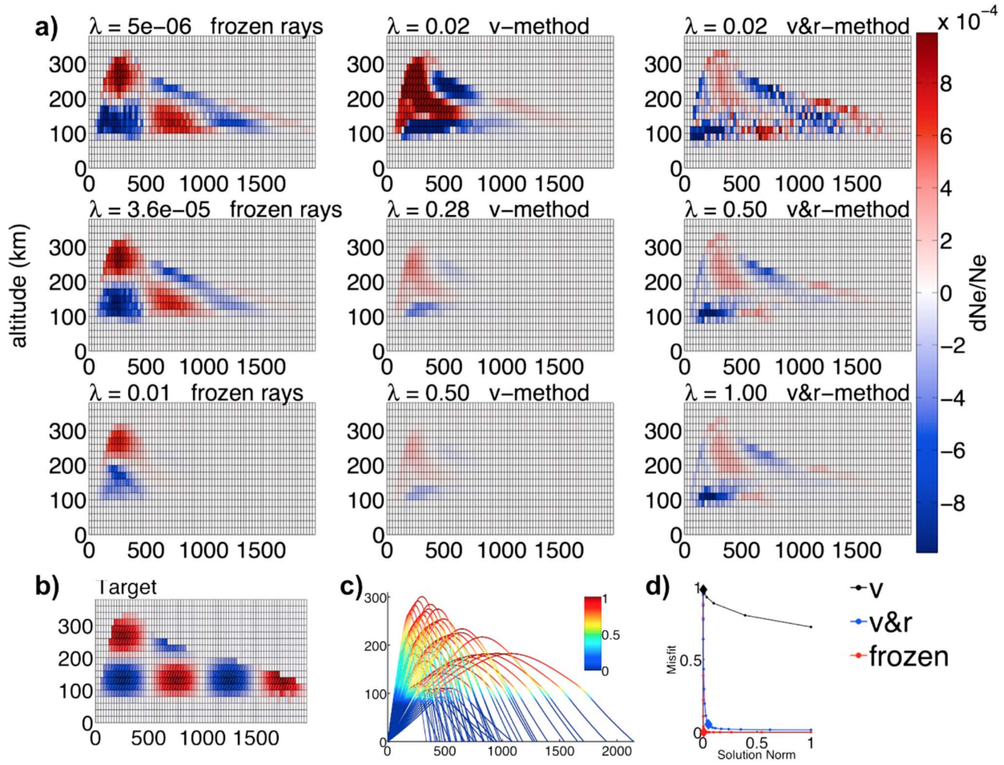

Figure 55: (a) Inversion results for a checkerboard perturbation with three different methods and for three different values of the regularization parameter λ. Frozen rays (left column, v method (middle column) and v&r method (right column). (b) Target model (c) Ratio between plasma frequency and emission frequency along the raypath quantifying the sensitivity of each ray to the propagation medium. Rays are most sensitive to the medium where the ration is approximately 1. (d) L curves for the frozen rays, v method and v&r method. Diamonds correspond to the best values of regularization. From: Roy et al. (2014)

4.2.4 Ionospheric Tomography by SuperDARN

SuperDARN radars are designed to analyze only the signal backscattered by ionospheric perturbation (e.g., plasma bubbles) and the ground-backscattered data are neglected (e.g. Chisham et al., 2008, Yeoman et al., 2008). In the same time, all the data reflected in the ionosphere and backscattered from the ground contains great information about the ionospheric structure as proven by Roy et al. (2014). We aim to apply the method proposed by Roy et al. (2014) to SuperDARN data, and nominally to the SuperDARN radar in Hokkaido for which a dataset was provided by Emma Bland from the University Centre in Svalbard (UNIS). We analyzed the complete dataset for Jan 5th 2014 for a constellation around 10:00 UTC for one azimuth (54°). In total this were 2131 rays. We used the same synthetic checkerboard perturbation as shown in Figure 55 for the ray coverage of the Hokkaido SuperDARN radar at that day and time. Figure 56 shows the results for the synthetic tests using the Hokkaido radar configuration of January 5th 2014. The regularization parameter λ only affect the noise level and not the solution of the inverse problem in the area of the best ray coverage. This shows that the method works well and it produces a stable inversion result. We can also see that in the area where we have a good coverage, the input model can be reproduced fairly well up to roughly 1200 km distance from the radar and at the altitude of 250 km. Compared to the ray coverage of the Nostradamus OTH radar (Figure 55) it is visible that the rays emitted at the Hokkaido radar don’t reach the same altitude and distance as the Nostradamus radar. The SuperDARN radars are designed to operate with an elevation angle of 10° - 40° and within a frequency range of 8 – 20 MHz whereas in normal operations they are operated around 10 – 14 MHz. The operating capacity of the Nostradamus radar lies at a frequency range of 6 – 16 MHz and elevation angles of 10° - 60° (Bazin et al., 2006). Those differences in the operating parameters account for the different ray coverage observed. In particular, the difference comes from the reception network and technical capability that allows, for the Nostradamus radar, a better resolution in the elevation angle estimation.

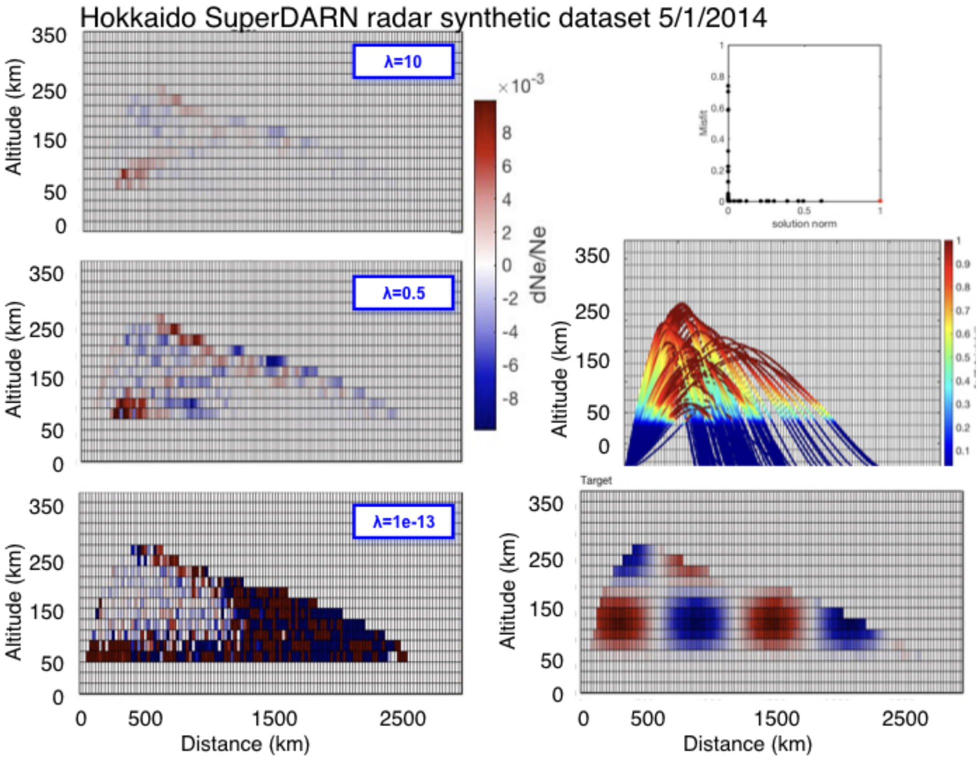

Figure 56: Results of synthetic tests for the Hokkaido Super DARN radar. Left column shows results for three different values of the regularization parameter λ. Right column from top to bottom, the L curve, ray coverage and target model

After the synthetic tests for the configuration on Jan 5th 2014 looked promising, we attempted an inversion of the real data for that day, assuming that the ionosphere was stable and not changing over the few minutes needed to acquire the dataset with different frequencies for one azimuth. The dataset contains a total of 2131 rays and within five frequency bands (9-9.2 MHz, 10.7-10.85 MHz, 11 MHz, 14.5-14.7 MHz, 16-16.2 MHz). Out of those rays were many with quite a big difference compared to the synthetic travel time computed using NeQuick (Radicella & Leitinger, 2001). The difference reached sometimes more than 100% and often it’s between 30% and 100% of the travel time. This is very likely due to the dataset being contaminated with ionospheric scatter which has low velocity and low spectral width; consequently it cannot be removed. Figure 57 shows the propagation time of real data compared to synthetic data for the Nostradamus OTH radar in France. The difference for

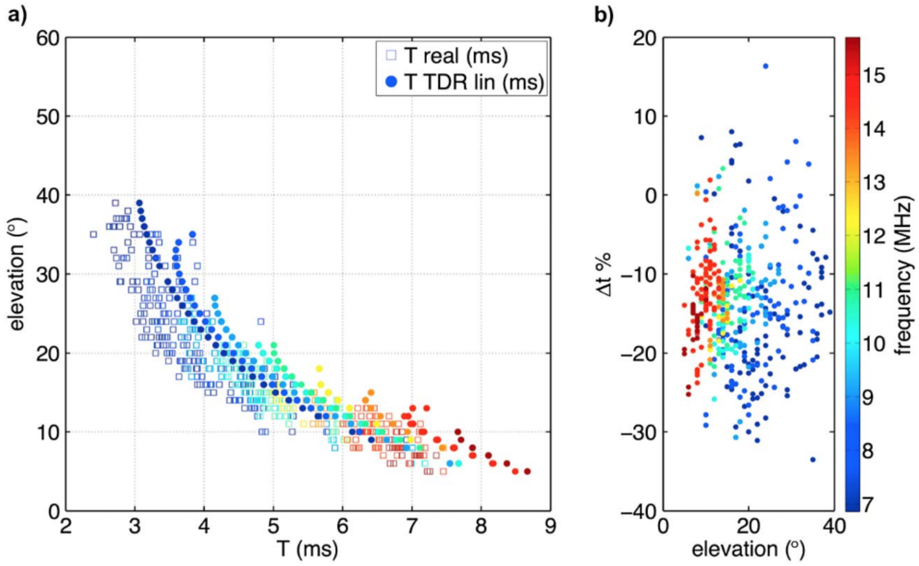

Figure 57: Propagation time of the real data and synthetic data simulated by ray tracing as (a) function of frequency and elevation angle and the (b) difference (%). From: Roy et al. (2014)

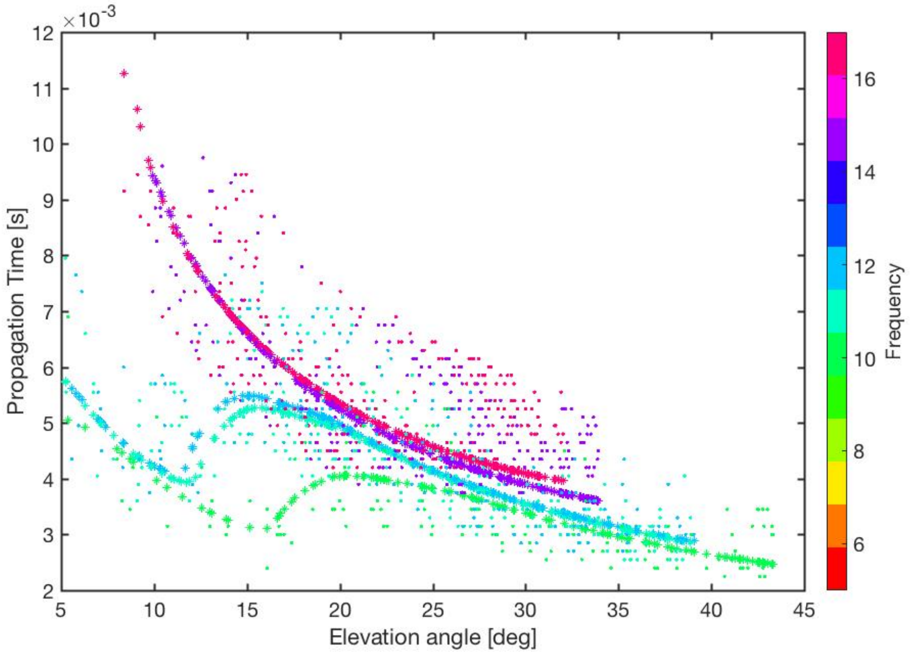

Figure 58: Propagation time of real data (*) and synthetic data (o) as a function of frequency and elevation angle for the Hokkaido SuperDARN on 5 Jan 2014

almost all rays lie within 30%. Therefor we have decided to use only rays that have a maximum difference of 30% compared to the synthetic data for our inversion of SuperDARN data. This reduces our dataset to 978 rays, meaning we remove more than half of the rays of the original dataset. If we use a filter condition of 15% difference there are only 542 rays left. Figure 58 shows the comparison of real data to synthetic travel times for the SuperDARN dataset. Compared to Figure 57 the travel times seem to spread more and have bigger differences. As mentioned before, this is related to the limit of SuperDARN to well estimate the elevation angle of the received signals. Additionally, this is only a first set of data analyzed for the Hokkaido SuperDARN; consequently the preliminary results have to be tested to more accurate, maybe less noisy, and larger datasets.

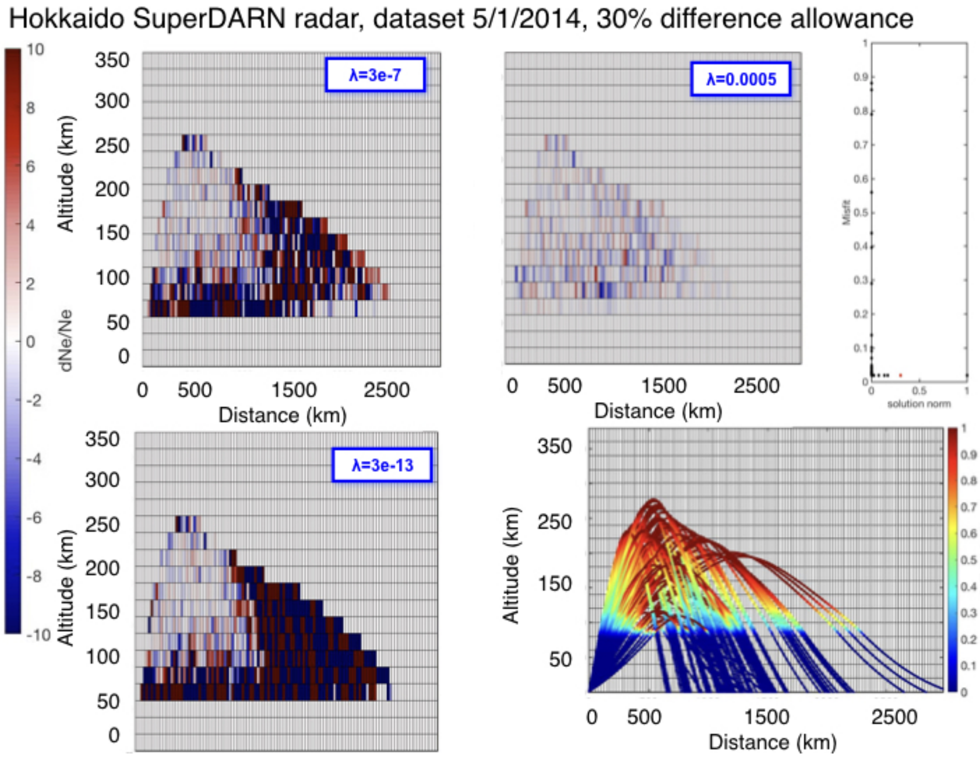
Hokkaido SuperDARN radar, dataset 5/1/2014, 30% difference allowance

Figure 59: Inversion results for the Hokkaido SuperDARN dataset of 5 Jan 2014 using an allowance of 30% difference in the propagation time between real and synthetic data. Shown are the results for three different regularization parameters λ (left and top middle), the ray coverage (bottom right) and the L curve (top right)

Figure 59 shows the results for the inversion of real data with an allowance of 30% difference to the synthetic travel times and Figure 60 for 15 % allowance. In both cases we get a stable solution in the area of good ray coverage and the regularization parameter is only influencing the noise level which supports the methodology adapted from the Nostradamus OTH radar to SuperDARN is working well. At the same time the amplitude of the solution is way off the expected. In both cases we see a perturbation of the ionosphere up to ten times the order of the background ionosphere. Those are not realistic results and most likely caused by a contaminated dataset. It's also noticeable that the inversion for both 30% and 15% allowance is different even though both are stable and robust solutions for their dataset. This also points to the conclusion that it is caused by the dataset being contaminated and that the methodology is working also for SuperDARN. The great advantage of SuperDARN is the number of radars close to each other, consequently this first test pushes us forward to extend the methodology to a full 3D grid to include several datasets together which can improve the methodology and the results.

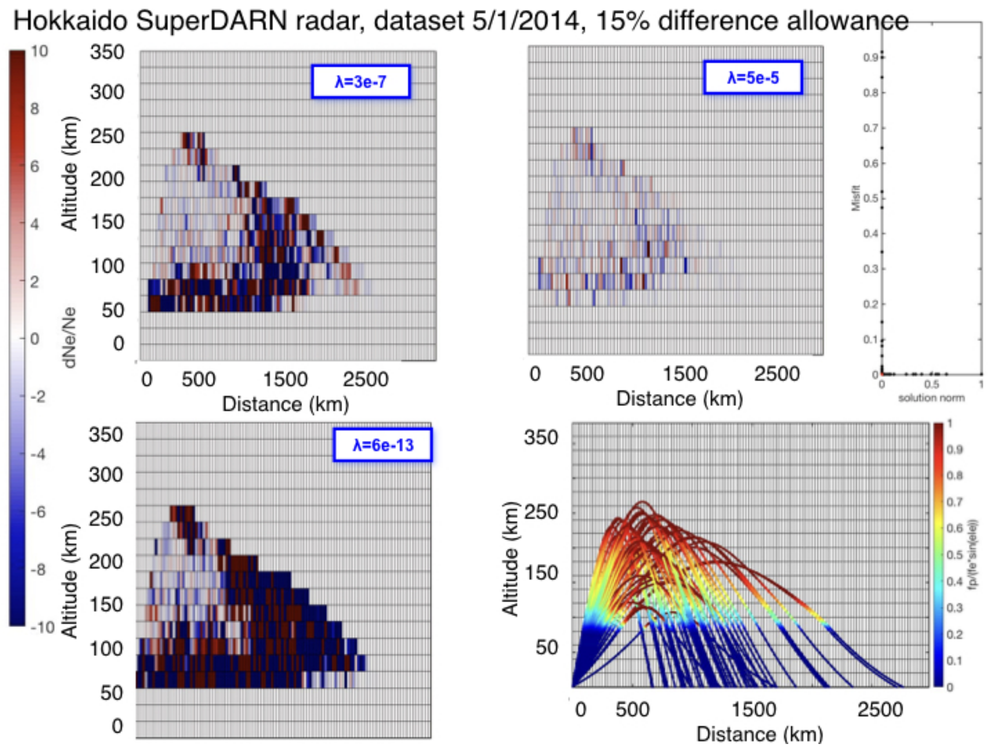

Figure 60: Same as Figure 59 but for 15% difference allowance, reducing the dataset even further

4.2.5 Joint ionospheric tomography by OTH radar/ SuperDARN/ GNSS-TEC

In order to explore the joint inversion coupling together several datasets, nominally the OTH radar, the SuperDARN and the GNSS-TEC, we start to extend our methodology to 3D. The preliminary test in Figure 61 shows the parametrization of the rays and the grid. Depicted are also the rays for an OTH radar/SuperDARN to show that this can potentially be implemented when the inversion shown by Roy et al. (2014) for a 2 dimensional plane of an OTH radar/SuperDARN is adjusted to 3D.

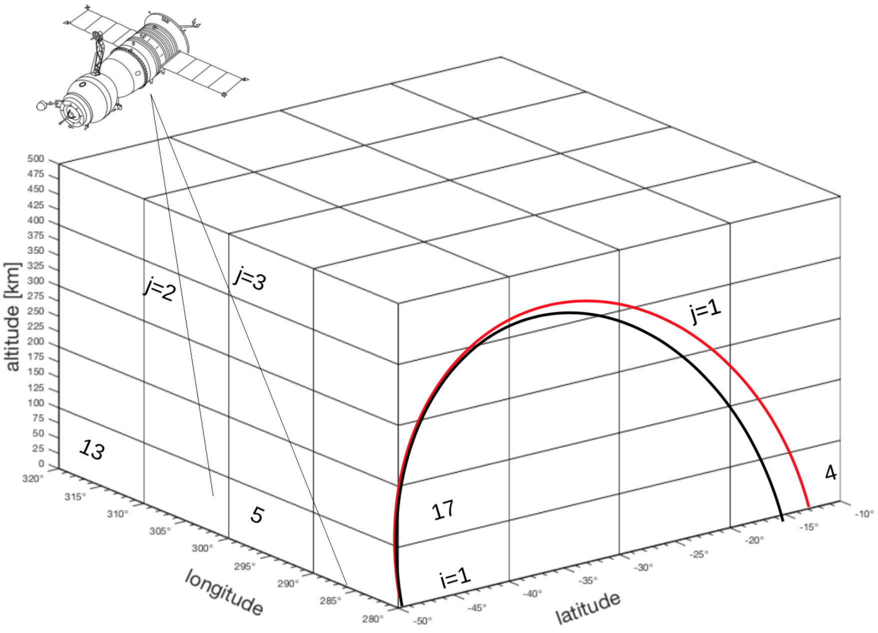

Figure 61: Schematic representation of the parametrization of the rays j and cells i with the raypath deflection induced by a localized perturbation producing a perturbed ray (red) compared to the unperturbed ray (black) for OTH radar. GPS satellite ground receiver raypaths are only shown in black as both start and endpoint of the rays are known.

For every measurement j the TEC can be expressed as the integral of the electron density perturbation δN_e:

$$dTEC_j = \int_j \delta_i N_e^{real} \, ds_{ij} \tag{27}$$

Where ds_{ij} is the length of the raypath segments within cell i of ray j. Introducing the matrix A of size M x N where M is the number of TEC measurements and N is the number of cells in the grid equation 27 can be rewritten as:

$$dTEC_j = \sum_{i=1}^{N} \delta N_e A_{ji} \tag{28}$$

In tensor notation equation 28 takes the form:

$$d\boldsymbol{TEC} = \boldsymbol{A} \cdot \delta \boldsymbol{N_e} \tag{29}$$

Where **δN**$\boldsymbol{\delta N_e}$ is the vector of model parameters with N unknown electron density perturbations $\delta N_{e,j}$, **dTEC** is the vector containing the M observed differential TEC measurements $dTEC_j$ and **A** is the geometric matrix containing the M x N raypath segments ds_{ij} of the j-th ray in cell i.

The inverse problem can now be written as:

$$\boldsymbol{dNe}=(\boldsymbol{A})^{-1}\boldsymbol{dTEC} \tag{30}$$

To solve equation 22 we use the damped least squares solution suggested by Menke (1989) and also used by Roy et al. (2014) for the inversion of OTH radar data. By using the same approach for GNSS data we aim for a joint inversion of GNSS/OTH radar/SuperDARN data. From now, we use OTH radar to include both, OTH radar and SuperDARN, as the method developed by Roy et al. (2014) works for both (Chapter 4.2.4). For the case of OTH radar the travel time of the ray can be written as:

$$T=\frac{-40.3}{cf_e^2}\int_{ray} N_e ds \tag{31}$$

With f_e the emission frequency and T the travel time. Using an a priori model this can be written as a travel time perturbation dT as a function of an electron density perturbation dN_e of the a priori model. Using the parametrization as in Figure 61 this becomes:

$$dT_j=\frac{-40.3}{f_{e_j}^2 c}\sum_{i=1}^{N} dN_e A_{ji} \tag{32}$$

Introducing a Matrix A’ to take into account not only the speed variation but also the raypath deflection induced by the variation of the scattering point this becomes in tensor formalism: dT = (A+A’) dN_e. For the joint inversion we can therefore write:

$$\begin{pmatrix} dT \\ dTEC \end{pmatrix}=\begin{pmatrix} A+A' \\ A \end{pmatrix} dN_e \tag{33}$$

And for the inversion:

$$dN_e=\begin{pmatrix} A+A' \\ A \end{pmatrix}^{-1}\begin{pmatrix} dT \\ dTEC \end{pmatrix} \tag{34}$$

Figure 62 shows the results of a first test with a synthetic perturbation as input model and the constellation of satellite and ground receivers at the time of the 2014 Iquique earthquake. In the area where we have rays crossing the cells we see that we can reconstruct the model quite well, whereas the cells without rays consequently show no perturbation after the inversion. For this very simple test with a small grid we show that the inversion algorithm works well in reconstructing the input model for the areas of good ray coverage.

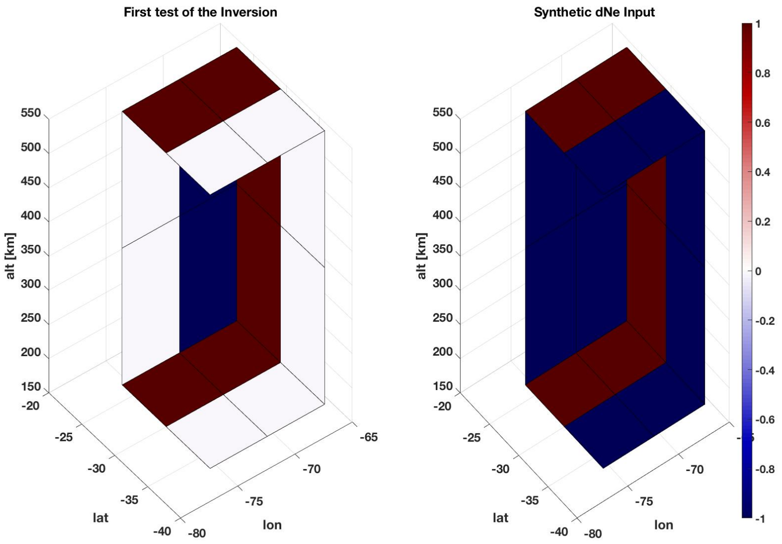

Figure 62: Inversion results of a first test with synthetic perturbation. Inversion results on the left and the input model on the right. Raypath coverage was used as was at the time of the Iquique earthquake 2014 in Chile

Figure 63 shows the statistics of an inversion test with the same input model as shown in Figure 62 but a much finer grid and using more rays. This way we can also verify the algorithm calculating the length of a ray in each cell crossed. In areas where neighboring cells have a big difference in the ray coverage there’s also an increasing difference in the solution and also in areas that are near the switch from the positive to the negative perturbation in the input model we can see quite big differences in the inversion results compared to the input. This shouldn’t be too worrying as the striped input model doesn’t really describe a realistic ionospheric disturbance and was also used to test the algorithm.

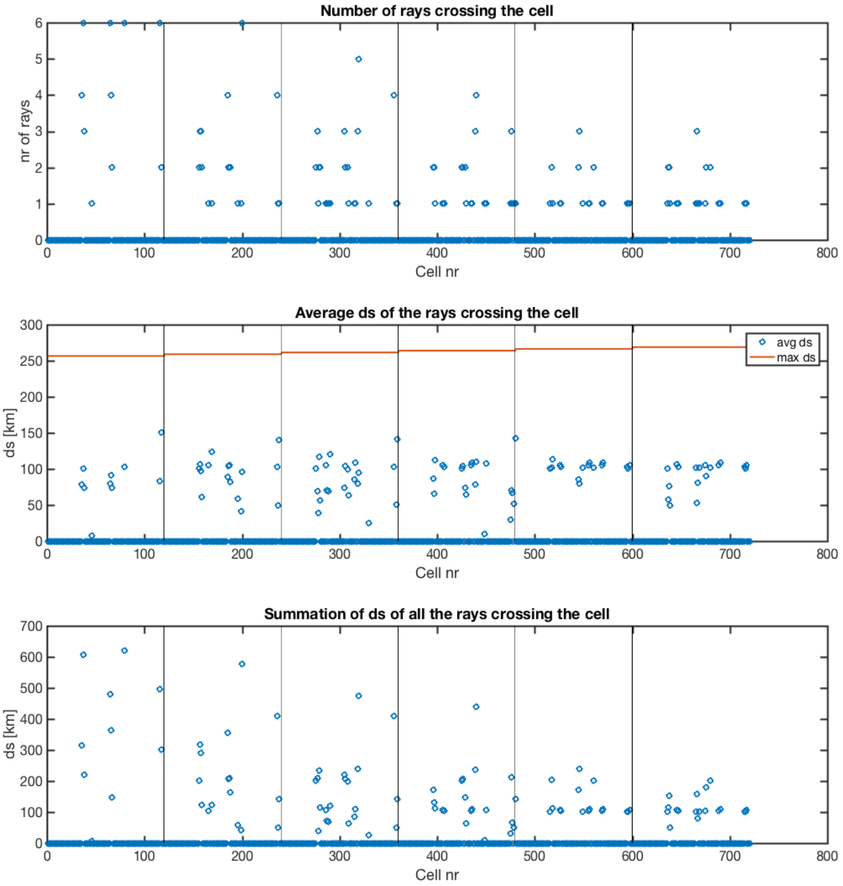

Figure 63: Statistics of the inversion test with synthetic input model. shown are from the top, the number of rays per cell over the number of the cell, the average length of a ray segment in the cell, the sum of all ray segments crossing the cell and on the bottom the difference of the inversion results to the input model

4.2.6 Ionospheric background model

In order to compute the differential TEC used in our inversion, we need to define an ionospheric background model. As discussed in Chapter 3 the use of a polynomial fit is rather subjective and we seek to use a model that doesn't strongly depend on data itself. To define a correct background model that correctly describes the ionosphere, is generally one of the most important objectives in ionospheric science and space weather studies. In this last part we wish to explore the limits of the different ionospheric models in comparison to the data. For that we first compute absolute TEC in correcting for satellite and ground receiver induced biases. To correct for the satellite bias we use the values from the CODE IONEX files of the University of Bern. The receiver bias is removed using the minimum-scalloping method (Rideout & Coster, 2006). Figure 64 shows the effect of the bias correction showing raw, satellite bias corrected and absolute TEC corrected for both satellite and receiver bias.

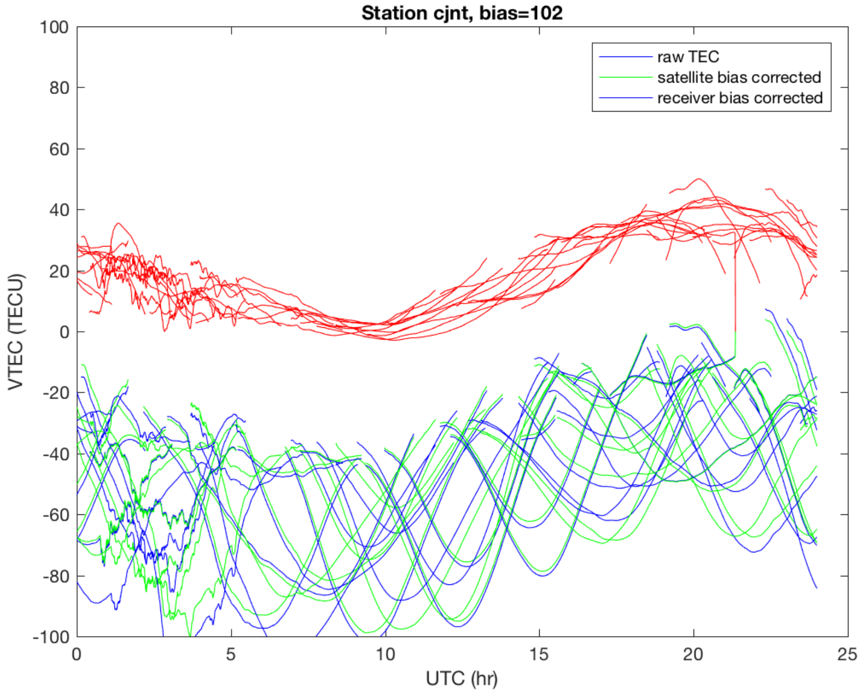

Figure 64: Comparison of raw TEC data (blue), TEC data corrected for satellite bias (green) and absolute TEC data corrected for both satellite and receiver bias (red) for station CJNT in Chile for the 27 February 2010

After computing the absolute TEC we can compare this to several background models. Figure 65 shows a comparison of the computed absolute TEC for station TERO in South America and satellite 24 with synthetic TEC calculated using several background models. For NeQuick we used the options included in NeQuick2 (Nava et al., 2008) to calculate directly the synthetic sTEC. For GIM (Global Ionospheric Map) we interpolate the values of the cells for the two hours between each GIM TEC map and then get the vTEC value corresponding to the position of the IPP for each epoch before converting it to sTEC for comparison. The synthetic IRI data is computed using a grid over the area and then getting the IRI value in 30s steps for the whole grid. After

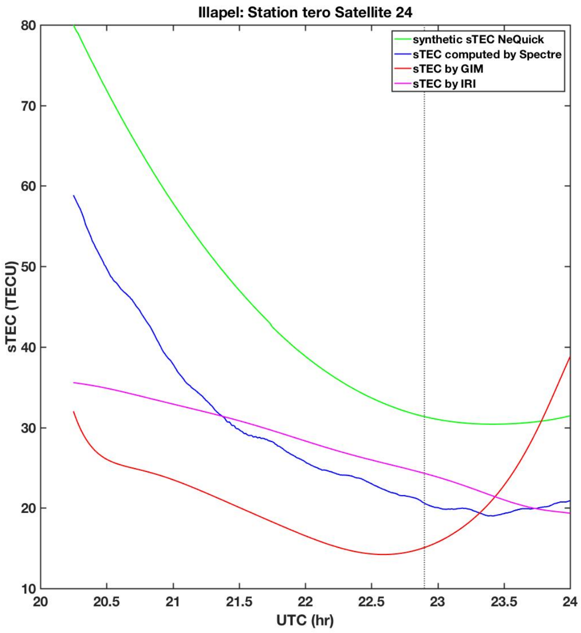

Figure 65: Comparison of absolute sTEC measured at station TERO with satellite 24 with synthetic TEC computed using NeQuick, IRI and GIM models. The dashed vertical line shows the time of the Illapel earthquake

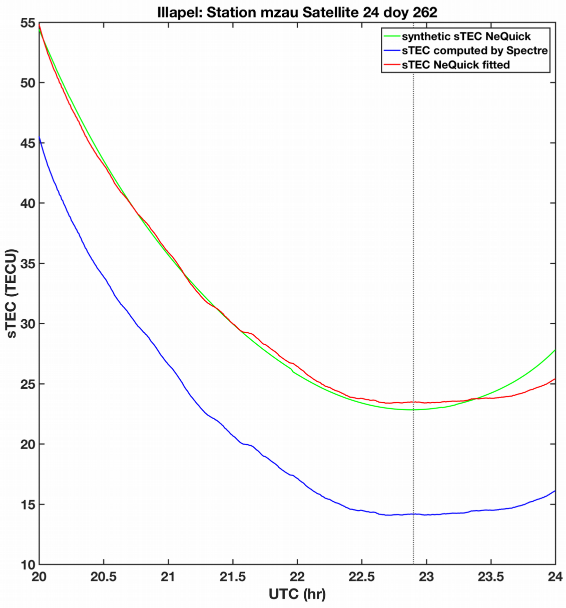

Figure 66: Comparison of absolute sTEC compared to NeQuick and absolute sTEC fitted to NeQuick

we use the calculated length of each ray inside a cell and the IRI value of the electron density to calculate the synthetic sTEC. For low angles the ray might have left the grid and therefor we get smaller values than expected looking at the curvature of the real data as some part of the ray is not taken into account in the summation in this case. In general the NeQuick data is fastest to compute and fits the data best looking at the form and curvature of the signal. Figure 66 shows the comparison of absolute sTEC to synthetic NeQuick and absolute sTEC where the bias correction is done in a way to minimize the difference between the NeQuick model and the data. This example of station MZAU depicts an example where this method works fine and we get a good fit of synthetics and real data. The shift between the model and the real data isn’t always constant though for different satellites as well as the curvature of the TEC can vary between real data and model. Therefore fitting data and model this way doesn’t always give sufficient results to use it as a way to calculate differential TEC. Finding a good background model that describes the ionosphere in a way that it can be used to compute differential TEC is probably the biggest challenge to get to the point of being able to do an inversion of real data without a strong assumption.

4.3 Conclusion

We have shown that the methodology of Roy et al. (2014) is adaptable for SuperDARN radar using a dataset of the Hokkaido radar. Additional to the effect of the ionospheric anomaly on the velocity of the passing wave the method also accounts for the raypath deflection. Both effects are comparable As we could show the application of this methodology on real data of the Hokkaido SuperDARN radar gives us stable solutions. The quality of the solution depends obviously on the ray coverage and the sensitivity of the rays to the ionosphere as the ray are reflected where the emission frequency is close to the plasma frequency. Although the solutions being stable there is the problem of the used dataset for the Hokkaido SuperDARN radar being contaminated with ionospheric scatter that couldn’t be removed automatically. Therefor we filter the dataset using only rays that have a difference in propagation time compared to synthetic data of maximum 30% and 15%. The fact that the two solutions are different proves that the dataset is very likely still contaminated with scatter data. Finding a reliable solution to clean the dataset before the inversion is therefore another challenge to obtain good results for a tomography of SuperDARN data. This is only a preliminary result on one single dataset, consequently exploring additional datasets is necessary to really understand the limit of the SuperDARN inversion. The stability of the preliminary solutions for the Hokkaido SuperDARN, mainly in the covered zone, is already a success, proving that the methodology developed for OTH radar can be applied to SuperDARN. The great advantage of SuperDARN is the dense network of radars, and consequently the dense number of rays coming from different directions. This pushes us to extent the inverse method proposed by Roy et al. (2014) in a full 3D grid in order to invert the entire SuperDARN network together.

The installation of the GPS system drove forward the attempts to reconstruct the ionosphere offering good raypath coverage and a high amount of available data. Several works show a successful reconstruction of the ionosphere or are even mapping TIDs (e.g. Cook & Close, 1995; Markkanen et al., 1995; Pryse et al., 1995). Our approach is to couple the inversion methodology used by Roy et al. (2014) for an ionospheric tomography by OTH radar together with the inversion of total electron content measured by GNSS satellites. First synthetic resolution tests using realistic station satellite positions over South America show that in areas of good coverage we are able to reproduce the input model in our solution. The big challenge in performing an inversion of real data will be to find a suitable background model. Several attempts to model the data have been carried out using different background models (NeQuick, IRI, GIM). The idea being to find an objective approach in using a background model that does not depend on the data itself compared to the rather subjective approach of using a polynomial fit to describe the background. One of the challenges is to calculate absolute TEC which is done using the minimum-scalloping method (Rideout & Coster, 2006). As shown in their publication the calculation of the receiver bias can have an error range of up to 10 TECU. Therefor we also carried out some tests using the background model to define the background ionosphere in the calculation of the receiver bias. This lead in some cases to improvement over the original calculation but not for all of the data. This shows the necessity of further tests and research in the quest to establish a good fitting background model before performing the inversion of real data.

5 Conclusion

This PhD had two main topics using GNSS TEC data: the detection of traveling ionospheric disturbances generated during total solar eclipses and the debate about the possibility of short-term earthquake precursors.

Regarding the total solar eclipses we obtained nice results for the Great American Eclipse which moved with a narrow 160 km wide Moon's shadow over the entire North America during daytime (10:00-15:00 LT) and along the path from Oregon to North Carolina. Outside of the totality zone, a partial solar eclipse associated with the penumbra covered the majority of the US. This amazing and unique phenomena was also observed by the wide network of ~3000 GNSS stations. The network showed for the first time, and with an unprecedently high spatial and time resolution, the response of the ionosphere visualized by TEC measurements all around North America. The TEC signature of the eclipse shows a strong absolute sTEC depletion of the order of 25% of the normal background estimated using the day before and day after the eclipse. We particularly imaged the signature of the eclipse on the entire North American subcontinent computing differential vertical TEC maps based on ~3000 stations and 21 satellites between GPS and GLONASS. Our differential vertical TEC maps show a depletion of -0.4 TECU in average following the Moon's shadow with a delay of around 10 min and broadly extended until 60 % of shadow in North America. Using different data fitting approaches we can show a proof of the existence of a bow wave trailing the eclipse in the TEC maps. We additionally use the high spatial and temporal resolution of our maps to fully analyze the wave propagation visible in the ionosphere as TIDs related to the Great American Eclipse: we perform an omega-k analysis by a 3D Fast Fourier Transform. We confirm the presence of TIDs with period of 40-70 min and wavelength of 200-450 km already observed in the literature using keograms, as well as the presence of TIDs with a period of 25-30 min and the wavelength of 300 km possibly triggered by the supersonic speed of the Moon's shadow. We also highlighted –for the first time in literature- longer wavelength (500-600 km) TIDs with a period of 30-60 min that are related to the TEC depletion due to the Moon's shadow, as well as shorter wavelength (50-100 km) TIDs with period of 40-65 min. Those last TIDs have sources co-located with the regions of stronger gradient of EUV at a specific time and consequently support the role of the modulation of sunspot in those waves generation. With our work we wished to push forward the full interpretation of the effect of the Great American Eclipse and generally the fast changing of the ionospheric plasma density related to quick solar flux variation.

In order to push forward our understanding of the solar eclipse signature in the ionosphere, we additionally analyzed another event that occurred on July 2nd 2019 over the Pacific Ocean and South America. Due to sparse or rather non-existent coverage over the Pacific we can only observe the last minutes of totality before sunset in Chile and Argentina. We could see a clear decrease in TEC for some stations in western Argentina where the Moon's shadow first arrived over South America. Compared to the surrounding days those stations show a decrease of about 25- 40 % compared to the background ionosphere. This lies within the expectations for solar eclipses at mid-latitudes (Jakowski et al., 2008, Ding et al., 2010).

We have also shown for two stations (mzal and mzac) observing satellite 19 which moves from north into the path of totality the TEC didn't recover to the background level before as the eclipse coincided with sunset. This made it challenging to show the depletion due to the eclipse using differential TEC for the spatial coverage on maps. Both the use of a polynomial fit as well as a bandpass filter didn't show clear results due to the overlap of the eclipse with the sunset. Nevertheless the implementation of additional processing of GLONASS data using the Spectre code added to the coverage compared to GPS use only. This increased the number of measurements by 1.5 to 2 times compared to GPS only and introduced a significant improvement of the Spectre code for processing GNSS TEC.

The second main topic was the debate sparked by Heki (2011) about the possibility of predicting earthquakes observing, in the ionosphere, the pre-seismic TEC enhancement 20 to 40 minutes before the earthquake. Several studies replied to his findings (e.g. Kamogawa & Kakinami, 2013; Utada & Shimizu, 2014) and mainly criticized his approach of calculating the reference curve and interpreted the observed perturbation (using a different reference curve) as a depletion in the ionospheric TEC after the event: the so called Ionospheric Hole. This started the Hole vs Enhancement debate that is still ongoing since 2011. The key of the debate is the computation of the unperturbed TEC reference curve used to highlight the hole or the enhancement.

Masci et al. (2015) showed that the natural daily variability of the TEC didn't allow to define a curve to discriminate between the hole or the enhancement in the TEC. Consequently we focussed our effort in explore the limits and the subjectivity of the method to define the unperturbed TEC reference curve. Eisenbeis & Occhipinti (in prep.b) picks up at the results from He & Heki (2016) for the South American earthquakes and by trying to reproduce the reference curve used by He & Heki (2016) to highlight the TEC enhancement, we discovered that the vTEC residual depends highly on the choice of degree of the polynomial fit as well as of the length of the time window before and after the earthquake. Staying within the specifications given by He & Heki (2016) for the calculation of the reference curve Eisenbeis & Occhipinti (in prep.b) could obtain mainly results that support the genesis of the hole in the TEC measurement after the earthquake and for only one specific time window, could also reproduce the fit of He & Heki (2016) showing the pre-seismic enhancement. Our results clearly demonstrated the choice of the unperturbed TEC reference curve is subjective reducing the possibility to predict earthquakes.

He & Heki (2016) also introduced the idea that the observed enhancement close to the epicenter is part of a perturbation that is also extended far away from the epicenter. Nominally, He & Heki (2016) proposed the idea that, during the nucleation process the fault acts as a dipole, producing electromagnetic perturbations which propagate into the ionosphere following the geomagnetic lines.

He & Heki (2018) visualized this in 3D with a more robust theory, but the problem is still the computation of the unperturbed background TEC reference curve. An additional problem is the resolution of the GNSS tomography so we explored, with preliminary results, the joint inversion with other techniques, in this case OTH radar and SuperDARN. Our approach is to adapt the inversion methodology used by Roy et al. (2014) for an ionospheric tomography by OTH radar to the use of GPS. This will facilitate a joint inversion later on. First synthetic resolution tests using realistic station-satellite positions over South America show that in areas of good coverage we are able to reproduce the input model in our solution. The big challenge in performing an inversion of real data will be to find a suitable background model. Several attempts to model the data have been carried out using different background models (NeQuick, IRI, GIM). The idea being to find an objective approach in using a background model that does not depend on the data itself compared to the rather subjective approach of using a polynomial fit to describe the background.

We have shown that the methodology of Roy et al. (2014) is adaptable for SuperDARN radar using a dataset of the Hokkaido radar. This methodology accounts for both the effect of the ionospheric disturbance on the velocity of the wave as well as the deflection of the raypath. As we could show the application of this methodology on real data of the Hokkaido SuperDARN radar gives us stable solutions. This shows the reliability of the inversion method. The quality of the solution depends obviously on the ray coverage and the sensitivity of the rays to the ionosphere as the ray are reflected where the emission frequency is close to the plasma frequency. Although the solutions being stable there is the problem of the used dataset for the Hokkaido SuperDARN radar being contaminated with ionospheric scatter that couldn’t be removed automatically. Finding a reliable solution to clean the dataset before the inversion is therefore another challenge to obtain good results for a tomography of SuperDARN data and the possibility to implement this in a joint inversion with GNSS TEC data.

Bibliography

[Afraimovich et al., 1998]: Afraimovich, E. L., Palamartchouk, K.S., Perevalova, N. P., Chemukov, V. V., Lukhnev, A.V., Zalutsky V. T., Ionospheric effects of the solar eclipse of March 9, 1997, as deduced from GPS data , 1998, Geophysical Research Letters, 25(4), , 465-468,
[Afraimovich et al., 2005]: Afraimovich, E.L., E.I. Astafyeva, V.V. Kiryushkin, Ionospheric disturbance in the near-field area of the epicenter of the September 25, 2003 Hokkaido earthquake, 2005, Radiophysics Quant. Electr., , 48, 268-280,
AIAA, 1999: , Guide to Reference and Standard Ionosphere Models, 1999
[Andreeva et al., 1990]: Andreeva, E.S., A.V. Galinov, V.E> Kunitsyn, Y.A. Mel'Nichenko, E.E. Tereschenko, M.A. Filimonov & S.M. Chernyakov, Radiotomographic reconstruction of ionization dip in the plasma near the earth, 1990, Soviet Journal of Experimental and Theoretical Physics Letters, 52, , 145-148,
[Anduaga, 2009]: Anduaga, A., Sydney Chapman on the Layering of the Atmosphere: Conceptual Unity and the Modelling of the Ionosphere, 2009, Annals of Science, 66, 3, 333-344, https://doi.org/10.1080/00033790802329455
[Appleton & Barnett, 1925]: Appleton, E. V. and Barnett, M. A., Local reflection of wireless waves from the upper atmosphere , 1925, Nature, 115, , 333,
[Arbesser-Rastburg, 2006]: Arbesser-Rastburg, B., The Galileo Single Frequency Ionospheric Correction Algorithm, 2006, European Space Weather Week, Brussels
[Artru et al., 2004]: Artru, J., T. Farges, P. Lognonne, Acoustic waves generated from seismic surface waves: propagation properties determined from Doppler sounding observation and normal-modes modeling, 2004, Geophys. J. Int., , 158, 1067-1077,
[Aryal et al., 2019]: Aryal, S., G. Geddes, S.C. Finn, S. Mrak, I. Galkin & I. Cnossen , Multispectral and multi-instrument observation of TIDs following the total solar eclipse of 21 August 2017 , 2019, Journal of Geophysical Research: Space Physics, 124, , 3761-3774,
[Astafyeva et al., 2011]: Astafyeva, E., P. Lognonné, and L. Rolland, First ionosphere images for the seismic slip of the Tohoku-oki Earthquake, 2011, Geophys. Res. Lett., 38, L22104, ,
[Astafyeva et al., 2013]: Astafyeva, E., S. Shalimov, E. Olshanskaya & P. Lognonné, Ionospheric response to earthquakes of different magnitudes: Larger quakes perturb the ionosphere stronger and longer, 2013, Geophysical Research Letters, 40, 9, , https://doi.org/10.1002/grl.50398
[Astafyeva et al., 2016]: Astafyeva, E., I. Zakharenkova, and Y. Pineau, Occurrence of the dayside three-peak density structure in the F2- and the topside ionosphere, 2016, J. Geophys.Res.-Space Physics, 121, N7, 6936-6949, doi:10.1002/2016JA022641
[Astafyeva et al., 2017]: Astafyeva, E., I. Zakharenkova, J.D. Huba, E. Doornbos, J. van den Ijssel, Global Ionospheric and thermospheric effects of the June 2015 geomagnetic disturbances: multi-instrumental observations and modeling, 2017, J. Geophys. Res.-Space Physics, 122, N11, 11716-11742, doi:10.1002/2017JA024174
[Astafyeva et al., 2018]: Astafyeva, E., I. Zakharenkova, K. Hozumi, P. Alken, P. Coisson, M.R. Hairston, andW.R. Coley, Study of the Equatorial and Low-latitude Electrodynamic and Ionospheric Disturbances during the 22-23 June

2015 Geomagnetic StormUsing Ground-based and Space-borne Techniques, 2018, J. Geophys. Res. - SpacePhysics, 123, N3, 2424-2440, doi:10.1002/2017JA024981
[Austen et al., 1988]: Austen, J.R., S.J. Franke & C.H. Liu, Ionospheric imaging using computerized tomography , 1988, Radio Science, 23, 3, 299-307,
[Azpilicueta & Brunini, 2008]: Azpilicueta, F. & C. Brunini, Vertical TEC in the equatorial anomaly region from satellite altimetry data, 2008, Advances in Space Research, 42, 4, 745-752, https://doi.org/10.1016/j.asr.2007.12.016
[Bailey at al., 2000]: Bailey, G. J., Y. Z. Su & K.-I. Oyama, Yearly variations in the low-latitude topside ionosphere, 2000, Ann. Geophys., 18, , 789-798, doi:10.1007/s00585-000-0789-0
[Baker et al., 2010]: Baker, J., J. Ruohoniemi, A. Ribeiro, L. Clausen, R. Greenwald, N. Frissell & K. Sterne, Monitoring ionospheric space weather with the Super Dual Auroral Radar Network (SuperDARN), 2010, 2010 IEEE Radar Conference, 1414-1417,
[Balasis & Mandea, 2007]: Balasis, G. & M. Mandea, Can electromagnetic disturbances related to the recent great earthquakes be detected by satellite magnetometers?, 2007, Tectonophysics, 431, , 173-195,
[Banks, 1976]: Banks P.M., R.W. Schunk & W.J. Raitt, The Topside Ionosphere: ARegion of Dynamic Transition, 1976, Annual Review of Earth and Planetary Sciences, 4, 1, 381-440,
[Bazin et al., 2006]: Bazin, V., J. Molinie, J. Munoz, P. Dorey, S. Saillant, G. Auffray, V. Rannou & M. Lesturgie, A general description about the OTH-radar Nostradamus, in Radar, 2006 IEEE Conference, 2006, Electromagnetism and Radar Dept., ONERA, Palaiseau, France, 634-642,
[Belrose, 2004]: Belrose, J.S., O.M. Bucci & G. Pelosi, Letters to the Editor - Marconi and the History of Radio, 2004, IEEE Antennas and Propagation Magazine, 46, 2, 130-131, 10.1109/MAP.2004.1305565
[Bent & Llewllyn, 1973]: Bent, RB. & Llewllyn, SK., Documentation and description of the Bent ionospheric model, 1973, SAMSO Technical, Report, , , 73-252,
[Bertel & Cole, 1988]: Bertel, D. G> & R.F. Cole, The inversion of backscatter ionograms IPS radio and space services, 1988, Technical Report, IPS-TR-88-03, , , ,
[Beynon & Jones, 1962]: Beynon, W. J. G. and E. S. O. Jones, Ionospheric effects of nuclear explosions, 1962, Nature, , 196, 253-254,
[Bilitza et al., 2017]: Bilitza, D., D. Altadill, V. Truhlik, V. Shubin, I. Galkin, B. Reinisch, X. Huang, International Reference Ionosphere 2016: From ionospheric climate to real-time weather predictions, 2017, Space Weather, 15, 2, 418-429, https://doi.org/10.1002/2016SW001593
[Bilitza et al., 2014]: Bilitza, D., D. Altadill, Y. Zhang, C. Mertens, V. Truhlik, P. Richards,L.-A. McKinnell, B. Reinisch, The International Reference Ionosphere 2012 - a model of international collaboration, 2014, J. Space Weather Space Clim., A07, 4, 1-12, doi:10.1051/swsc/2014004
[Bilitza, 1990]: Bilitza, D., International Reference Ionosphere 1990, 1990
[Bilitza, 2001]: Bilitza, D., International reference ionosphere 2000, 2001, Radio Sci., 36, 2, 261-275,
[Blanc & Richmond, 1980]: Blanc, M., and A. D. Richmond, The ionospheric disturbance dynamo, 1980, J.Geophys. Res., 85, , 1669-1686, doi:10.1029/JA085iA04p01669

[Bolt, 1964]: Bolt, B. A., Seismic air waves from the great 1964 Alaskan earthquake, 1964, Nature,
[Booker, 1977]: Booker, H.G., Fitting of multi-region ionospheric profiles of electron density by a single analytic function of height, 1977, J. Atmos. Terr. Phys., 39, 5, 619-623,
[Borries et al., 2015]: Borries, C., J. Berdermann, N. Jakowski, and V. Wilken, Ionosphericstorms—A challenge for empirical forecast of the total electron content, 2015, J. Geophys. Res. Space Physics, 120, , 3175-3186, doi:10.1002/2015JA020988
[Bracewell & Bracewell, 2000]: Bracewell, R. N. & R. Bracewell, The Fourier Transform and Its Applications, 2000
[Bust et al., 2004]: Bust, G.S., T.W. Garner & T.L. Gaussiran, Ionospheric Data Assimilation Three-Dimensional (IDA3D) A global, multisensor, electron density specification algorithm, 2004, Journal of Geophysical Research: Space Physics, 109, A11, ,
[Cahyadi & Heki, 2013]: Cahyadi, M.N. & K. Heki, Ionospheric disturbances of the 2007 Bengkulu and the 2005 Nias earthquakes, Sumatra, observed with a regional GPS network, 2013, Journal of Geophysical Research: Space Physics, 118, 4, 1777-1787, https://doi.org/10.1002/jgra.50208
[Calais & Minster, 1995]: Calais, E. & J. B. Minster, GPS detection of ionospheric perturbations following the January, 1994, Northridge earthquake, 1995, Geophys. Res. Lett., 22, , 1045-1048,
[Calais & Minster, 1996]: Calais, E. & J. B. Minster, GPS detection of ionospheric perturbations following a Space Shuttle ascent, 1996, Geophys. Res. Lett., 23, 1897-1900,
[Calais et al., 1998]: Calais, E., J. B. Minster, M. A. Hofton and M.A.H. Hedlin, Ionospheric signature of surface mine blasts from Global Positioning System measurement, 1998, Geophys. J. Int., 132, , 191-202,
[Chapman, 1931]: Chapman, S., Ferraro, V. C. A., A new theory of magnetic storms, 1931, Journal of Geophysical Research, 36, 2, 77-97, https://doi.org/10.1029/TE036i002p00077
[Chen et al., 2019]: Chen, P., H. Liu, Y. Ma & N. Zheng, Accuracy and consistency of different global ionospheric maps released by IGS ionosphere associate analysis centers, 2020, Advnces in Space Research, 65, 1, 163-174, https://doi.org/10.1016/j.asr.2019.09.042
[Cherniak and Zakharenkova, 2018]: Cherniak, I. and Zakharenkova, I., Ionospheric total electron content response to the great American solar eclipse of 21 August 2017, 2018, Geophysical Research Letters, 45, , 1199-1208, https://doi.org/10.1002/2017GL075989
[Chimonas and Hines, 1971]: Chimonas, G. and Hines, C.O., Atmospheric gravity waves induced by a solar eclipse, 2, 1971, Journal of Geophysical Research, 76(28), , 7003-7005,
[Chimonas, 1970]: Chimonas, G., Internal gravity-wave motions induced in the Earths atmosphere by a solar eclipse, 1970, Journal of Geophysical Research, 75(28), , 5545-5551,
[Chisham et al., 2008]: Chisham, G, T.K. Yeoman & G.J Sofko, Mapping ionospheric backscatter measured by the SuperDARN HF radars - Part 1: A new empirical height model, 2008, Ann. Geophys., , 26, 823-841,
[Coisson et al., 2006]: Coisson, P., S. M. Radicella, R. Leitinger & B. Nava, Topside electron density in IRI and NeQuick: Features and limitations, 2006,

Advances in Space Research, 37, 5, 937-942, https://doi.org/10.1016/j.asr.2005.09.015
[Coisson et al., 2008]: P. Coisson, S.M. Radicella, B. Nava & R. Leitinger, Low and equatorial latitudes topside in NeQuick, 2008, J. Atmos. Sol. Terr. Phys., 70, 6, 901-906,
[Colegrove, 2000]: Colegrove, S., Project Jindalee: from bare bones to operational OTHR, 2000, Radar Conference, 2000. The Record of the IEEE 2000 International, , , 825-830,
[Coleman, 1998]: Coleman, C.J., A ray tracing formulation and its application to some problems on over-the-horizon radar, 1998, Radio Sci., , 33(4), 1187-1197,
[Cook & Close, 1995]: Cook, J. & S. Close, An investigation of TID evolution observed in MACE'93 data, 1995, Annales Geophysicae 13(12), , , 1320-1324,
[Coster et al., 2017]: Coster, A. J., Goncharenko, L., Zhang, S.-R., Erickson, P. J., Rideout, W., Vierinen, J., GNSS Observations of ionospheric variations during the 21 August 2017 solar eclipse, 2017, Geophysical Research Letters, 44, , , https://doi.org/10.1002/2017GL075774
[Crowley et al., 2006]: Crowley, G., C.L. Hackert, R.R. Meier, D.J. Strickland, L.J. Paxton, X. Pi, A. Manucci, A.B. Christesen, D. Morrison, G.S. Bust, R.G. Roble, N. Curtis & G. Wene, Global thermosphere-ionosphere response to onset of 20 November 2003 storm, 2006, Journal of Geophysical Research - Space Physics, 111, A10, , https://doi.org/10.1029/2005JA011518
[Dang et al., 2018]: Dang, T., J. Lei, W. Wang, B. Zhang, A. Burns & H. Le, Global responses of the coupled thermosphere and ionosphere system to the August 2017 Great Americn Solar Eclipse, 2018, Journal of Geophysical Research: Space Physics, 123, , 7040-7050,
[DasGupta et al., 2006]: DasGupta, A., A. Das, D. Hui, K. K. Bandyopadhyay, and M. R. Sivaraman, Ionospheric perturbation observed by the GPS following the December 26th, 2004 Sumatra-Andaman earthquake, 2006, Earth Planet. Space, 35, , 929-959
[Dautermann & Calais, 2008]: Dautermann, T. & E. Calais, TEC Data Processing Software, 2008
[Davies & Baker, 1965]: Davies, K. and D. M. Baker, The integrated ionospheric response to internal atmospheric gravity waves, 1965, J. Geophys. Res., , 70, 2251-2253
[Dear & Mitchell, 2007]: Dear, R.M. & C.N. Mitchell, Ionospheric imagin at mid-latitudes using both GPS and ionosondes, 2007, Journal of atmospheric and solar-terrestrial physics, 69, 7, 817-825,
[Di Giovanni & Radicella, 1990]: Di Giovanni, G. & S. M. Radicella, An analytical model of the electron density profile in the ionosphere, 1990, Advances in Space Research, 10, 11, 27-30, https://doi.org/10.1016/0273-1177(90)90301-F
[Dieminger & Kohl, 1962]: Dieminger, W. and H. Kohl, Effects of nuclear explosions in the ionosphere, 1962, Nature, , 193, 963-964,
[Ding et al., 2010]: Ding, F., Wan, W., Ning, B., Liu, L., Le, H., Xu, G., Yang, M., GPS TEC response to the 22 July 2009 total solar eclipse in East Asia , 2010, Journal of Geophysical Research, 115(A7), , A07308, https://doi.org/10.1029/2009JA015113
[Donn & Posmentier, 1964]: Donn, W. and E. S. Posmentier, Ground-coupled air waves from the great Alaskan earthquake, 1964, J. Geophys. Res., 5357-5361, 69, ,

[Ducic et al., 2003]: Ducic, V., J. Artru, P. Lognonne, Ionospheric remote sensing of the Denali Earthquake Rayleigh surface waves, 2003, Geophys. Res. Lett., 30, , 1951-1954,
[Eisenbeis & Occhipinti in prep.a]: Eisenbeis, J. & G. Occhipinti, New constraints from the LYAR station: the TEC enhancement before the seismic event is a simple artifact
[Eisenbeis & Occhipinti in prep.b]: Eisenbeis, J. & G. Occhipinti, New constraints from the LYAR station: the TEC enhancement before the seismic event is a simple artifact
[Eisenbeis et al., 2019]: Eisenbeis, J., G. Occhipinti, E. Astafyeva & L. Rolland, Short- and Long-Wavelength TIDs Generated by the Great American Eclipse of 21 August 2017, 2019, JGR Space Physics
https://doi.org/10.1029/2019JA026919
[Evans & Hagfors, 1968]: Evans, J.V. & T. Hagfors, Radar Astronomy, 1968, McGraw-Hill
[Fehmers et al., 1998]: Fehmers, G.C., L.P.J. Kamp, F.W. Sluijter & T.A.T. Spoelstra, A model-independent algorithm for ionospheric tomography: 1. Theory and tests, 1998, Advances in Space Research, 10, 11, 27-30,
[Feichter & Leitinger, 1997]: Feichter, E. & R. Leitinger, A 22-year cycle in the F layer ionization of the ionosphere, 1997, Ann. Geophys., 15, , 1015-1027, doi:10.1007/s00585-997-1015-0.
[Fremouw et al., 1992]: Fremouw, E.J., J.A. Secan & B.M. Howe, Application of stochastic inverse theory to ionospheric tomography, 1992, Radio Science, 27, 5, 721-732,
[Fridman & Fridman, 1994]: Fridman, O.V. & S.V. Fridman, A method of determining horizontal structure of the ionosphere from backscatter ionograms, 1994, J. Atmos. Terr. Phys., , 56(1), 115-131,
[Fridman & Nickisch, 2001]: Fridman, S.V. & L.J. Nickisch, Generalization of ionospheric tomography on diverse data sources: Reconstruction of the three-dimensional ionosphere from simultaneous vertical ionograms, backscatter ionograms and total electron content data, 2001, Radio Science, 36, 5, 1129-1139,
[Fridman et al., 2006]: Fridman, S.V., L.J. Nickisch, L. Aiello & M. Hausman, Real-time reconstruction of the three-dimensional ionosphere using data from a network of GPS receivers , 2006, Radio Science, 41, 5, ,
[Fridman et al., 2009]: Fridman, S.V., L.J. Nickisch & M. Hausman, Personal-computer-based system for real-time reconstruction of the three-dimensional ionosphere using data from diverse sources, 2009, Radio Science, 44, 3, ,
[Fridman et al., 2012]: Fridman, S.V., L. Nickisch & M. Hausmann, Inversion of backscatter ionograms and TEC data for over-the-horizon radar, 2012, Radio Science, 47
[Fridman, 1998]: Fridman, S.V., Reconstruction of a three-dimensional ionosphere from backscatter and vertical ionogramsmeasured by over-the-horizon radar, 1998, Radio Sci., , 33(4), 1159-1171,
[Fuller-Rowell et al., 1994]: Fuller-Rowell, T.J., M.V. Codrescu, R.J. Moffett & S. Quegan, Response of the thermosphere and ionosphere to geomagnetic storms, 1994, J. Geophys. Res., 99, , 3893-3914,
[Galvan et al., 2012]: Galvan, D. A., A. Komjathy, M. P. Hickey, P. Stephens, J. Snively, Y. T. Song, M. D. Butala, and A. J. Mannucci, Ionospheric signatures of

Tohoku-Oki tsunami of March 11, 2011: Model comparisons near the epicenter, 2012, Radio Sci., 47, , 4003,
[Garcia & Crespon, 2008]: Garcia, R. & F. Crespon, Radio tomography of the ionosphere: Analysis of an underdetermine, ill-posed inverse problem and regional application, 2008, Radio Sci., 43, , ,
[Geller et al., 1997]: Geller, R.J., D.D. Jackson, Y. Kagan, F. Mulargia, Earthquakes can not be predicted, 1997, Science, 275, 5306, , doi:10.1126/science.275.5306.1616.
[Gilbert, 1972]: Gilbert, P., Iterative methods for the three-dimensional reconstruction of an object from projections, 1972, Journal of Theoretical Biology, 36, 1, 105-117,
[Gillmor, 1982]: Gillmor, C., Wilhelm Altar, Edward Appleton, and the Magneto-Ionic Theory, 1982, Proceedings of the American Philosophical Society, 126, 5, 395-440,
[Goncharenko et al., 2007]: Goncharenko, L. P., J. C. Foster, A. J. Coster, C. Huang, N. Aponte, and L. J.Paxton, Observations of a positive storm phase on September 10, 2005, 2007, J. Atmos. Sol. Terr. Phys., 69, , 1253–1272,
[Gonzalez et al., 1994]: Gonzalez, W.D., J.A. Jocelyn, Y. Kamide, H.W. Kroehl, G. Rostocker, B.T. Tsurutani & V.M Vasyliunas , What is a geomagnetic storm?, 1994, J. Geophys. Res., 99, A4, 5771-5792,
[Gordon et al., 1970]: Gordon, R., R. Bender & G.T. Herman, Algebraic reconstruction techniques (ART) for three-dimensional electron microscopy and X-ray photography, 1970, Journal of theoretical Biology, 29, 3, 471-481,
[Greenwald et al., 1995]: Greenwald, R.A., K.B. Baker, J.R. Dudeney, M.Pinnock, T.B. Jones, E.C. Thomas, J.-P. Villain, J.-C. Cerisier, C. Senior, C. Hanuise, R.D. Hunsucker, G. Sofko, J. Koehler, E. Nielsen, R. Pellinen, A.D.M. Walker, N. Sato & H. Yamagishi, Darn/Superdarn: A global View of the Dynamics of High-Latitude Convection, 1995, Space Science Reviews, , 71, 761-796,
[Hajj et al., 1994]: Hajj, G.A., R. Ibanez-Meier, E. Kursinski & L. Romans, Imgaing the ionosphere with the Global Positioning System, 1994, International Journal of Imaging Systems and Technology, 5, 2, 174-187,
[Hansen et al., 1997]: Hansen, A.J., T. Walter & P. Enge, Ionospheric correction using tomography, 1997, Proceedings of Institute of Navigation ION GPS-97, Kansas City, 249-260,
[Harding et al., 2018]: Harding, B.J., D. P. Drob, R. A. Buriti & J. J. Makela, Nightside detection of a large-scale thermospheric wave generated by a solar eclipse, 2018, Geophysical Research Letters, , 45, 3366-3373,
[Harkrider, 1964]: Harkrider, D. G., Theoretical and observed acoustic-gavity waves from explosive sources in the atmosphere, 1964, J. Geophys. Res., 69, , 5295,
Hawass, 2005: Hawass, Z., Tutankhamun CT Scan http://www.guardians.net/hawass/press_release_tutankhamun_ct_scan_results.htm, 2005
[Hayakawa et al., 2011]: Hayakawa, M., Y. Kasahara, T. Nakamura, F. Muto, T. Horie, S. Maekawa, Y. Hobara, A. A. Rozhnoi, M. Solovieva & O. A. Molchanov, A statistical study on the correlation between lower ionospheric perturba- tions as seen by subionospheric VLF/LF propagation and earthquakes, 2011, J. Geophys. Res., 115, A09305, , doi:10.1029/2009JA015143

[He & Heki, 2018]: He, L. & K. Heki, Three-dimensional tomography of ionospheric anomalies immediately before the 2015 Illapel earthquake, 2018, Journal of Geophysical research: Space Physics, 123, , ,
[He & Heki, 2016]: He, L. & K. Heki, Three-dimensional distribution of ionospheric anomalies prior to three large earthquakes in Chile, 2016, Geophysical Research Letters, 43, , 7287-7293,
[He & Heki, 2017]: He, L. & K. Heki, Ionospheric anomalies immediately before Mw 7.0-8.0 earthquakes, 2017, Journal of Geophysical Research: Space Physics, 122, , 8659-8678,
[He et al., 2018]: He, L., K. Heki & L. Wu, Three-dimensional and trans-hemispheric changes in ionospheric electron density caused by the great solar eclipse in North America on 21 August 2017, 2018, Geophysical Research Letters, , 45, 933-940,
[Headrick & Anderson, 2008]: Headrick, J. M. & S. J. Anderson, HF Over-the-Horizon Radar, 2008, Radar Handbook, McGraw-Hill
[Heaton et al., 1995]: Heaton, J., S. Pryse & L. Kersley, Improved background representation, ionosonde input and independent verification in experimental ionospheric tomography, 1995, Annales Geophysicae 13(12), , , 1297-1302,
[Heaton et al., 1996]: Heaton, J., G. Jones & L. Kersley, Toward ionospheric tomography in Antarctica: first steps and comparison with dynasonde observations, 1996, Antarctic Science, 8, , 297-302,
[Heki, 2011]: Heki, K., Ionospheric electron enhancement preceding the 2011 Tohoku-Oki earthquake, 2011, Geophysical Research Letters, 38, , ,
[Heki & Enomoto, 2013]: Heki, K. & Y. Enomoto, Preseismic ionospheric electron enhancements revisited, 2013, Journal of Geophysical Research: Space Physics, 118, , 6618-6626,
[Heki & Enomoto, 2014]: Heki, K. & Y. Enomoto, Reply to comment by K. Heki and Y. Enomoto on " Preseismic ionospheric electron enhancement revisited", 2014, Journal of Geophysical Research: Space Physics, 119, , 6016-6018,
[Heki & Enomoto, 2015]: Heki, K. & Y. Enomoto, Mw dependence of the preseismic ionospheric electron enhancements, 2015, Journal of Geophysical Research: Space Physics, 120, , 7006-7020,
[Heki & Ping, 2005]: Heki, K. & J. Ping , Directivity and apparent velocity of coseismic ionospheric disturbances obsvered with a dense GPS array, 2005, Earth Plan. Sciences Let., , 236, 845-855,
[Heki et al., 2006]: Heki, K., Y. Otsuka, N. Choosakul, N. Hemmakorn, T. Komolmis, T. Maruyama, Detection of ruptures of Andaman fault segments in the 2004 gret Sumatra earthquake with coseismic ionospheric disturbances, 2006, J. Geophys. Res., 111, B09313, ,
[Hernandez-Pajares et al. (1999)]: Hernandez-Pajares, M., J. Juan & J. Sanz, New approaches in global ionospheric determination using ground GPS data, 1999, J. Atmos. Sol. Terr. Phys. , 61, 16, 1237-1247, 10.1016/s1364-6826(99)00054-1
[Hernandez-Pajares et al., 2009]: Hernández-Pajares, M., J. Juan, J. Sanz, R. Orus, A. Garcia-Rigo, J. Feltens, A. Komjathy, S. Schaer, A. Krankowski, The IGS VTEC maps: a reliable source of ionospheric information since 1998, 2009, J. Geod., , , 263-275, 10.1007/s00190-008-0266-1
[Hernandez-Pajares et al., 1998]: Hernandez-Pajares, K., J.M. Juan, J. Sanz & J.G. Sole, Global observations of the ionospheric electronic response to solar

events using ground and LEO GPS data, 1998, Journal of Geophysical Research: Space Physics, 103, A9, 20789-20796,
[Hines, 1960]: Hines, C.O., Internal atmospheric gravity waves at ionospheric heights, 1960, Can. J. Phys., , 38, 1441-1481,
[Ho et al., 1996]: Ho, C., A. Mannucci, U. Lindqwister, X. Pi, B. Tsurutani, Global ionosphere perturbations monitored by the worldwide GPS network, 1996, Geophys. Res. Lett., 23, 22, 3219-3222, 10.1029/96GL02763
[Hoque et al., 2016]: Hoque, M. M., Wenzel D., Jankowski, N., Gerzen, T., Berdermann, J., Wilken, V., Minkwitz, D., Ionospheric response over Europe during the solar eclipse of March 20, 2015, 2016, Journal of Space Weather and Space Climate , 6(A36), , , doi:10.1051/swsc/2016032
[Huang & Cheng, 1994]: Huang, Y.-N. & K. Cheng, Solar cycle variation of the total electron content around equatorial anomaly crest region in east asia, 1994, Journal of Atmospheric and Terrestrial Physics, 57, 12, 1503-1511,
[Huang et al., 1989]: Huang, Y.-N., K. Cheng & S.-W. Chen, On the equatorial anomaly of the ionospheric total electron content near the northern anomaly crest region, 1989, J. Geophys. Res., 94, 13, 13515-13525, doi:10.1029/JA094iA10p13515
[Huba & Drob, 2017]: Huba, J.D. & D. Drob, SAMI3 prediction of the impact of the 21 August 2017 total solar eclipse on the ionosphere/plasmasphere system, 2017, Geophysical Research Letters, , 44, 5928-5935,
[Huba et al., 2016]: Huba, J. D., Sazykin, S., & Coster, A., SAMI3-RCM simulation of the 17March 2015 geomagnetic storm, 2016, Journal of Geophysical Research: SpacePhysics, 122, , , doi:10.1002/2016JA023341, 1246–1257
[Ivanova et al., 1998]: Ivanova, V. A., Ryabova, N. V. and Shumaev, V. V., Effect of the solar eclipse of 22 July 1990 at mid-latitude path of HF propagation, 1998, Journal of Atmospheric and Solar Terrestrial Physics , 59, , 1013-1016,
[Iyemori et al., 2005]: Iyemori, T., M. Nose, D. Han, Y. Gao, M. Hashizume, N. Choosakul, H. Shinagawa, Y. Tanaka, M. Utsugi, A. Saito, H. McCreadie, Y. Odagi & F. Yang , Geomagnetic pulsations caused by the Sumatra earthquake on December 26, 2004, 2005, Geophysical Research Letters, 32, 20, ,
[Jakowski et al, 1981]: Jakowski, N., H. D. Bettac, B. Lazo & L. Lois, Seasonal variations of the columnar electron content of the ionosphere observed in Havana from July 1974 to April 1975, 1981, J. Atmos. Terr. Phys., 43, , 7-11, doi:10.1016/0021-9169(81)90003-9.
[Jakowski et al., 2008]: Jakowski, N., Stankov, S., Wilken, V., Borries, C., Altadill, D., Chum, J., Canderd, L. R., Ionospheric behaviour over Europe during the solar eclipse of 3 October 2005, 2008, J. Atmos. Sol. Terr. Phys., 70, , 836-853,
[Kakinami et al., 2012]: Kakinami, Y., M. Kamogawa, Y. Tanioka, S. Watanabe, A.R. Gusman, J.-Y. Liu, Y. Watanabe & T. Mogi, Tsunamigenic ionospheric hole, 2012, Geophysical Research Letters, 39, , ,
[Kamogawa & Kakinami, 2013]: Kamogawa, M. & Y. Kakinami, Is an ionospheric electron enhancement preceding the 2011 Tohoku-Oki earthquake a precursor?, 2013, Journal of Geophysical Research: Space Physics, 118, , 1751-1754,
[Kamogawa, 2006]: Uyeda, S., M. Kamogawa & T. Nagao, Preseismic lithosphere-atmosphere-ionosphere coupling, 2006, Complexity in Earthquakes, Tsunamis, and Volcanoes, and Forecasting and Early Warning of their Hazards,

edited by W. H. K. Lee, Series of Encyclopedia of Complexity and System Science (Editor-in-Chief, Robert Meyers), Springer, 87(40), , 417-424, doi:10.1029/2006EO400002
[Kamogawa, 2007]: Kamogawa, M., Reply to Comment on “Preseismic lithosphere- atmosphere-ionosphere coupling”, 2007, Eos Trans. AGU, 88(23), , 248, doi:10.1029/2007E0230009
[Kanamori (1977)]: Kanamori, H., The energy release in great Earthquakes, 1977, J. Geophys. Res., 82, , 2981-2987,
[Karpenko, 2014]: , The radar station (ZGRLS) of 29b6 below the horizon "CONTAINER", 2014, htttp://bastion-karpenko.ru/container/
[Kelly et al., 2014]: Kelly, M.A., J.M. Comberiate, E.S. Miller & L.J. Paxton, Progress toward forecasting of space weather effects on UHF SATCOM after Operation Anaconda, 2014, Space Weather, 12, 10, 601-611, https://doi.org/10.1002/2014SW001081
[Kersley et al., 1993]: Kersley, L., A.T. Heaton, S.E. Pryse & T.D. Raymund, Experimental ionospheric tomography with ionosonde input and EISCAT verification, 1993, Annales Geophysicae 11, , , 1064-1074,
[Kersley et al., 1997]: Kersley, L., S. Pryse, I. Walker, J. Heaton, C. Mitchell, M. Williams & C. Willson, Imaging of electron density troughs by tomographic techniques, 1997, Radio Science, 32, 4, 1607-1621,
[Kirby et al., 1934]: Kirby, S. S., L. V. Berkner & D. M. Stuart, Studies of the ionosphere and their application to radio transmission, 1934, Proc. Inst. Rad. Eng., 22, , 481-521,
[Klobuchar, 1985]: Klobuchar, J.A., Ionospheric time delay effects on earth space propagation, 1985, Handbook of Geophysics and the space environment, Chapter 10.8, (A.S. Jursa, editor), US Air Force, Washington D.C., , , 1084-1088,
[Kunitake et al., 1995]: Kunitake, M., K. Ohtaka, T. Maruyama, M. Tokumaru, A. Morioka & S. Watanabe, Tomographic imaging of the ionosphere over Japan by the modified truncated SVD method, 1995, Annales Geophysicae 13(12), , , 1303-1310,
[Kunitsyn et al., 1994]: Kunitsyn, V.E., E.S. Andreeva, O.G. Rezinkov & E.D. Tereshenko , Phase and phase-difference ionospheric radio tomography, , International Journal of Imaging Systems and Technology, 5, 2, 128-140,
[Landeau et al., 1997]: Landeau, T., F. Gauthier & N. Ruelle, Further improvements to the inversion of elevation-scan backscatter sounding data, 1997, J. Atmos. Terr. Phys., , 59(1), 125-138,
[Lay et al., 2005]: Lay, T., H. Kanamori, C.J. Ammon, M. Bettles, S.N. Ward, R.C. Aster, S.L. Bilek, M.R. Brudzinski. R. Butler, H.R. DeShon, G. Ekstrom, K. Satake & S. Sipkin, The great Sumatra-Andaman earthquake of 26 December 2004, 2005, Science, 308, , 1127-133,
[Le et al., 2009]: Le, H., L. Liu, X. Yue, W. Wan, B. Ning, Latitudinal dependance of the ionospheric response to solar eclipses, 2009, Journal of Geophysical Research, A07308, 114, , doi:10.1029/2009JA014072
[Le et al., 2011]: Le, H., J. Y. Liu, and L. Liu, A statistical analysis of ionosphericanomalies before 736 M6.0+ earthquakes during 2002–2010, 2011, J. Geophys.Res., 116, A02303, , doi:10.1029/2010JA015781
[Le Pichon et al., 2005]: Le Pichon, A., P. Herry, P. Mialle, J. Vergoz, N. Brachet, M. Garces, D. Drob & L. Ceranna, Infrasound associated with 2004–2005 large Sumatra earthquakes and tsunami, 2005, Geophys. Res. Lett., 32, L19802, ,

[Lei et al., 2018]: Lei, J., T. Dang, W. Wang, A. Burns, B. Zhang & h. Le, Long-lasting response of the global thermosphere and ionosphere to the 21 August 2017 solar eclipse, 2018, Journal of Geophysical Research: space Physics, , 123, 4309-4316,
[Leitinger et al., 2005]: Leitinger, R., M.-L. Zhang & S. M. Radicella, An improved bottomside for the ionospheric electron density model NeQuick, 2005, Annals of Geophysics, 48, 3, , https://doi.org/10.4401/ag-3217
[Leonard & Barnes, 1965]: Leonard, R. S. and R. A. Barnes, Observation of ionospheric disturbances following the Alaskan earthquake, 1965, J. Geophys. Res., , 70, 1250-1253,
[Lin et al., 2018]: Lin, C. Y., Deng, Y. and Ridley, A., Atmosperic gravity waves in the ionosphere and thermosphere during the 2017 solar eclipse, 2018, Geophysical Research Letters, 45, , 5246-5252, https://doi.org/10.1029/2018GL077388
[Liu, 2007]: Liu, B.-Y., HF Over-the-horizon Radar system Performance analysis, 2007, Ph.D thesis, Naval Postgraduate School
[Liu et al., 1998]: Liu, J. Y., Hsiao, C. C., Tsai, L. C., Liu, C. H., Kuo, F. S. , Vertical phase and group velocities of internal gravity waves derived from ionograms during the solar eclipse of 24 October 1995, 1998, Journal of Atmospheric and Solar Terrestrial Physics, 60(1998), , 1679-1686,
[Liu et al., 2004]: Liu, J.Y., Y.J. Chuo, S.J. Shan, Y.B. Tsai, Y.I. Chen, S.A. Pulinets and S.B. Yu, Pre-earthquake ionospheric anomalies registered by continuous GPS TEC measurements, 2004, Annales Geophysicae, , , 1585-1593,
[Liu et al., 2006]: Liu, J.Y., Y.I. Chen, Y.J. Chuo & C.S. Chen, A statistical investigation of preearthquake ionospheric anomaly, 2006, Journal of Geophysical Research: Space Physics, 111, A5, , https://doi.org/10.1029/2005JA011333
[Liu et al., 2006a]: Liu, J. Y., Y. B. Tsai, S. W. Chen, C. P. Lee, Y. C. Chen, H. Y. Yen, W. Y. Chang, and C. Liu, Giant ionospheric distrubances excited by the M9.3 Sumatra earthquake of 26 December 2004, 2006, Geophys. Res. Lett., 33, L02103, ,
[Liu et al., 2006b]: Liu, J., Y. Tsai, K. Ma, Y. Chen, H. Tsai, C. Lin, M. Kamogawa, and C. Lee, Ionospheric GPS total electron content (TEC) disturbances triggered by the 26 December 2004 Indian Ocean tsunami, 2006, J. Geophys. Res., 111, A05303, ,
[Liu et al., 2011]: Liu, J.-Y., C.-H. Chen, C.-H. Lin, H.-F. Tsai, C.-H. Chen, and M. Kamogawa, Ionospheric disturbances triggered by the 11 March 2011 M9.0 Tohoku earthquake, 2011, J. Geophys. Res., 116, A06319, ,
[Lognonne et al., 2006]: Lognonne, P., J. Artru, R. Garcia, F. Crespon, V. Ducic, E. Jeansou, G. Occhipinti, J. Helbert, G. Moreaux & P.-E. Godet , Ground-based GPS imaging of ionospheric post-seismic signal, 2006, Planetary and Space Science, 54, , 528-540,
[Lu et al., 2008]: Lu, G., L. P. Goncharenko, A. D. Richmond, R. G. Roble, and N. Aponte, A dayside ionospheric positive storm phase driven by neutral winds, 2008, J. Geophys.Res., 113, A08304, , doi:10.1029/2007JA012895
[Ma et al., 2003]: Ma, R., J. Xu & H. Liao, The features and a possible mechanism of semiannual variation in the peak electron density of the low latitude F2 layer, 2003, J. Atmos. Sol. Terr. Phys., 65, 47-57, doi:10.1016/S1364-6826(02)00192-X

[Ma et al., 2005]: Ma, X.F., T. Maruyama, G. Ma & T. Takeda, Three-dimensional ionospheric tomography using observation data of GPS ground receivers and ionosonde by neural network, 2005, Journal of Geophysical Research: Space Physics, , A5, 110,

[Mai & Kiang, 2009]: Mai, C.-L. and J.-F. Kiang, Modeling of ionospheric perturbation by 2004 Sumatra tsunami, 2009, Radio Sci., 44, RS3011, ,

[Main, 1999]: Main, I., Is the reliable prediction of individual earthquakes a realistic scientific goal?, 1999, Nature

[Manucci et al. (1993)]: Manucci, A.J., B.D. Wilson and C.D. Edwards, A new method for monitoring the Earth's ionospheric total electron content using GPS global network, 1993, Paper presented at ION GPS-93, Salt Lake City, September 22-24, 1993

[Manucci et al., 1998]: Manucci, A. J., B. D. Wilson, D. N. Yuan, C. H. Ho, U. J. Lindqwister, T. F. Runge, A global mapping technique for GPS-derived ionospheric electron content measurments., 1998, Radio Sci., 33, , 565-582,

[Markkanen et al. (1995)]: Markkanen, M., M. Lehtinen, T. Nygren, J. Pirttila, P. Hnelius, E. Vilenius, E. Tereshenko & B. Khudukon, Bayesian approach to satellite radiotomography with applications in the Scandinavian sector, 1995, Annales Geophysicae 13(12), , , 1277-1287,

[Markkanen et al., 1995]: Markkanen, M., M. Lehtinen, T. Nygren, J. Pirttila, P. Hnelius, E. Vilenius, E. Tereshenko & B. Khudukon, Bayesian approach to satellite radiotomography with applications in the Scandinavian sector, 1995, Annales Geophysicae 13(12), , , 1277-1287,

[Maruyama et al., 2005]: Maruyama, N., Richmond, A. D., Fuller-Rowell, T. J., Codrescu, M. V., Sazykin, S.,Toffoletto, F. R., , 2005, Geophys. Research Lett., 32, L17105, , https://doi.org/10.1029/2005GL023763

[Masci et al., 2015]: Masci, F., J. Thomas, F. Villani, J. Secan & N. Rivera, On the onset of ionospheric precursors 40 min before strong earthquakes, 2015, Journal of Geophysical Research: Space Physics, 120, , 1383-1393,

[Mayr & Mahajan, 1971]: Mayr, H. G., and K. K. Mahajan, Seasonal variation in the F2 region, 1971, J. Geophys. Res., 76, , 1017-1027, doi:10.1029/JA076i004p01017

[McNamara and Smith, 1982]: McNamara, L. F., and D. H. Smith, Total electron content of the ionosphere at 31°S, 1967–1974, 1982, J. Atmos. Terr. Phys., 44, , 227-239, doi:10.1016/0021-9169(82)90028-9

[Mendillo et al., 2005]: Mendillo, M., C. Huang, X. Pi, H. Rishbeth & R. Meier, The global ionospheric asymmetry in total electron content, 2005, J. Atmos. Sol. Terr. Phys., 67, , 1377-1387, doi:10.1016/j.jastp.2005.06.021

[Menke, 1989]: Menke, W., Geophysical Data Analysis: Discrete InverseTheory, 1989, Academic Press, San Diego, Calif.

[Mitchell & Spencer, 2003]: Mitchell, C.N. & P.S. Spencer, A three-dimensional time-dependent algorithm for ionospheric imaging using GPS, 2003, Annals of Geophysics, 46, 4, 1311-1319,

[Mitchell et al., 1995]: Mitchell, C., D. Jones, L. Kerseley, S.E. Pryse, Imaging of field-aligned structures in the auroral ionosphere, 1995, Annales Geophysicae 13(12), 1311-1319,

[Momani et al., 2010]: Momani, M. A., Yatim, B. & Mohd Ali, M. A., Ionospheric and geomagnetic response to the total solar eclipse on 1 August 2008 over Northern Hemisphere , 2010, Journal of Geophysical Research, 115(A8), , A08321, https://doi.org/10.1029/2009JA014999

[Mrak et al., 2018a]: Mrak, S., J. Semeter, D. Drob & J. D. Huba, Direct EUV/X-Ray modulation of the ionpsphere during the August 2017 total solar eclipse, 2018, Geophysical Research Letter, , 45, 3820-3828,
[Mrak et al., 2018b]: Mrak, S., J. Semeter, Y. Nishimura, M. Hirsch & N. Sivadas, Coincidental TID production by tropospheric weather during the August 2017 total solar eclipse, 2018, Geophysical Research Letters, , 45, 10,903-10,911,
[Na & Sutton, 1994]: Na, H. & E. Sutton, Resolution analysis of ionospheric tomography systems, 1994, International Journal of Imaging Systems and Technology, 5, 2, 169-173,
[Najita & Yuen, 1979]: Najita, K. & P. C. Yuen, Long-Period oceanic Rayleigh wave group velocity dispersion curve from HF Doppler sounding of the ionosphere, 1979, Journal of Geophysical Research, 84, 4, ,
[Najman and Kos, 2014]: Najman, P. & T. Kos, Performance analysis of empirical ionosphere models by comparison with CODE vertical TEC maps., 2014
[National Imagery and Mapping Agency, 2000]: National Imagery and Mapping Agency, Department of defense world geodetic system 1984: Its definition and relationships with local geodetic systems, 2000, Tech Rep., TR8350.2, , , ,
[Nava et al., 2008]: Nava, B., P. Coisson & S. M. Radicella, A new version of the NeQuick ionosphere electron density model, 2008, Journal of Atmospheric and Solar-Terrestrial Physics, 70, 15, 1856-1862, https://doi.org/10.1016/j.jastp.2008.01.015
[Nayak and Yigit, 2018]: Nayak, C. & Yigit, E., GPS-TEC observation of gravity waves generated in the ionosphere during 21 August 2017 total solar eclipse, 2018, Journal of Geophysical Research: Space Physics, , 123, 725-738,
[Nygren et al., 1997]: Nygren, T., M. Markkanen, M. Lehtinen, E. Tereshenko, B. Khudukon, O. Evstafiev & P. Pollari, Comparison of F-region electron density observations by satellite radio tomography and incoherent scatter methods, 1997, Annales Geophysicae 14(12), , , 1422-1428,
[Occhipinti, 2015]: Occhipinti, G., , 2015, From Mantle Flow to Mega Disasters, 169-182, 10.1002/9781118888865.ch9
[Occhipinti et al., 2006]: Occhipinti, G., P. Lognonné, E. Alam Kherani, and H. Hebert, Three-dimensional waveform modeling of ionospheric signature induced by the 2004 Sumatra tsunami, 2006, Geophys. Res. Lett., 33, L20104, ,
[Occhipinti et al., 2008]: Occhipinti, G., A. Komjathy, and P. Lognonné, Tsunami detection by GPS: how ionospheric observation might improve the Global Warning System, 2008, GPS World, 19, 2, 50-56,
[Occhipinti et al., 2010]: Occhipinti, G., P. Dorey, T. Farges & P. Lognonne, Nostradamus: The radar that wanted to be a seismometer, 2010, Geophysical Research Letters, 37, 10.1029/2010gl044009
[Occhipinti et al., 2018]: Occhipinti, G. F. Aden-Antoniow, A. Bablet, J.-P. Molinie & T. Farges, Surface waves magnitude estimation from ionospheric signature of Rayleigh waves measured by Doppler sounder and OTH radar, 2018, Scientific Reports
[Occhipinti et al., 2013]: Occhipinti, G., L. Rolland, P. Lognonné & S. Watada, , 2013, Journal of Geophysical Research: Space Physics, 118, 6, 3626-3636, 10.1002/jgra.50322

[Occhipinti, 2006]: Occhipinti, G., Observations multi-parametres et modelisation de la signature ionospherique du grand seisme de Sumatra, 2006, PhD thesis, Institut de Physique du Globe de Paris
[Occhipinti, 2015]: Occhipinti, G., , 2015, From Mantle Flow to Mega Disasters, 169-182, 10.1002/9781118888865.ch9
[Okal & Talandier, 1989]: Okal, E. A. and J. Talandier, Mm: A variable period mantle magnitude, 1989, J. Geophys. Res., , 94, 4169-4193,
[Okal & Talandier, 1991]: Okal, E. A. and J. Talandier, Single-station estimates of the seismic moment of the 1960 Chilean and 1964 Alaskan earthquakes, using the mantle magnitude Mm, 1991, Pure appl. Geophys., , 136, 103-126,
[Olivier, 1962]: Olivier, J., A summary of observed seismic surface wave dispersion, 1962, Bull. Seismol. Soc. Amer., 127, 44, ,
[Orus et al., 2002]: Orús, R., M. Hernández-Pajares, J. Juan, J. Sanz & M. Garcı́a-Fernández, Performance of different TEC models to provide GPS ionospheric corrections, 2002, J. Atmos. Sol. Terr. Phys., 64, 18, 2055-2062, 10.1016/s1364-6826(02)00224-9
[Park et al., 2005]: Park, J., K. Anderson, R. Aster, R. Butler, T. Lay & D. Simpson, Global Seismographic Network records the Great Sumatra-Andaman earthquake, 2005, Eos. Trans. AGU, 86, 6, ,
[Paznukhov et al., 2009]: Paznukhov, V. V., D. Altadill, and B. W. Reinisch, Experimental evidence forthe role of the neutral wind in the development of ionospheric storms in midlatitudes, 2009, J. Geophys. Res., 114, A12319, , doi:10.1029/2009JA014479
[Picone et al., 2002]: Picone, J. M., Hedin, A. E., Drob, D. P. and Aikin, A. C., NRLMSISE-00 empirical model of the atmosphere: Statistical comparisons and scientific issues, 2002, J. Geophys. Res., 107(A12), , 1468, doi:10.1029/2002JA009430
[Pinon et al., 2018]: Pinon, D.A., D.D. Gomez, R. Smalley, S.R. Cimbaro, E.A. Lauria & M.G. Bevis, The History, State and Future of the Argentine continuous Satellite monitoring network and its contributions to Geodesy in Latin America, 2018, Seismological research Letters, 89, 2A, 475-482, https://doi.org/10.1785/0220170162
[Pitteway & Hines, 1963]: Pitteway, L. V. & C. O. Hines, The viscous damping of atmospheric gravity waves, 1963, Canaian J. Phys., 41, 12, 1935-1948,
[Pokhotelov et al., 2011]: Pokhotelov, D., P. Jayachandran, C. Mitchell, J. MacDougall & M. Denton, GPS tomography in the polar cap: comparison with ionosondes and in situ spacecraft data, 2011, GPS Solutions, 15, 1, 79-87,
[Pradipta et al., 2018]: Pradipta, R., E. Yizengaw & P. Doherty, Ionospheric density Irregularities, turbulence and wave disturbances during the total solar eclipse over North America on 21 August 2017, 2018, Geophysical Research Letters, 45, , 7909-7917,
[Press & Harkrider, 1962]: Press, F. & D. Harkrider, Propagation of acoutstic-gravity waves in the atmosphere, 1962, J. Geophys. Res., 67, 10, 3889,
[Prölss, 1976]: Prölss, G.W., On explaining the negative phase of ionospheric storms, 1976, Planet. Space Sci., 24, , 607-609,
[Prölss, 1980]: Prölss, G.W., Magnetic Storm Associated Perturbations of the UpperAtmosphere: Recent Results Obtained by Satellite-Borne Gas Analyzers, 1980, Reviews of Geophysics and Space Physics, 18, N1, 183-202,

[Pryse & Kersley, 1992]: Pryse, S. & L. Kersley, A preliminary experimanteal test of ionospheric tomography, 1992, Journal of Atmospheric and Terrestrial Physics, 54, 7-8, 1007-1012,
[Pryse et al., 1995]: Pryse, S., C. Mitchell, J. Heatonn & L. Kersley, Travelling ionospheric disturbances imaged by tomographic techniques, 1995, Annales Geophysicae 13(12), 1325-1330,
[Radicella & Leitinger, 2001]: Radicella, S. M. & R. Leitinger, The evolution of the DGR approach to model electron density profiles, 2001, Advances in Space Research, 27, 1, 35-40, https://doi.org/10.1016/S0273-1177(00)00138-1
[Rao, 1974]: Rao, N. N., Inversion of sweep-frequency sky-wave backscatter leading edge for quasiparabolic ionospheric layer parameters, 1974, Radio Sci., , 9(10), 845-847,
[Rawlinson et al., 2010]: Rawlinson, N., S. Pozgay & S. Fishwick, Seismic tomography: A window into deep Earth, 2010, Physics of th Earth and Planetary Interiors, 178, 3-4, 101-135,
[Raymund et al., 1990]: Raymund, T.D., J.R. Austen, S.J. Franke, C.H Liu, J.A. Klobuchar & J. Stalker, Application of computerized tomography to the investigation of ionospheric structures, 1990, Radio Science, 25, 5, 771-789,
[Raymund, 1994]: Raymund, T.D., Ionospheric tomography algorithms, 1994, International Journal of Imaging Systems and Technology, 5, 2, 75-85,
[Rideout & Coster, 2006]: Rideout, W. & A. Coster, Automated GPS processing for global total electron content data, 2006, GPS solutions, , 10, 219-228,
[Ridley et al., 1984]: Ridley, E. C., R. E. Dickinson, M. H. Rees & R. G. Roble , Thermospheric response to the June 11, 1983 solar eclipse, 1984, Journal of Geophysical Research, , 89(A9), 7583-7588,
[Rishbeth et al., 2000]: Rishbeth, H., I. C. F. Müller-Wodarg, L. Zou, T. J. Fuller-Rowell, G. H. Millward, R. J. Moffett, D. W. Idenden & A. D. Aylward, Annual and semiannual variations in the ionospheric F2-layer: II. Physical discussion, 2000, Ann. Geophys., 18, , 945-956, doi:10.1007/s00585-000-0945-6
[Rishbeth, 1998]: Rishbeth, H. , How the thermospheric circulation affects the ionosphere, 1998, J. Atmos. Sol. Terr. Phys., 60, , 1385-1402, doi:10.1016/S1364-6826(98)00062-5
[Rishbeth, 2007]: Rishbeth, H., Do earthquake precursors really exist?, 2007, Eos Trans. AGU, 88(29), , 296, doi:10.1029/2007EO290008
[Rius et al., 1997]: Rius, A., G. Ruffini & L. Cucurull, Improving the vertical resolution of ionospheric tomography with GPS occultations, 1997, Geophysical Research Letters, 24, 18, 2291-2294,
[Rodger & Clilverd, 2007]: Rodger, C. J., and M. A. Clilverd, Comment on “Preseismic Lithosphere-Atmosphere-Ionosphere Coupling”, 2007, Eos Trans. AGU, 88(23), doi:10.1029/2007EO230008
[Rolland et al., 2010]: Rolland, L., G. Occhipinti, P. Lognonné & A. Loevenbruck, Ionospheric gravity waves detected offshore Hawaii after tsunamis, 2010, Geophys. Res. Lett., 37, 17, ,
[Rolland et al., 2011]: Rolland, L. M., P. Lognonné, E. Astafyeva, E. A. Kherani, N. Kobayashi, M. Mann, and H. Munekane, The resonant response of the ionosphere imaged after the 2011 off the Pacific coast of Tohoku Earthquake, 2011, Earth Planets Space, 63, , 853-857,
[Rose et al., 1961]: Rose, G., J. Oksman and E. Kataja, Round the world sound waves produced by the nuclear explosion on October 30, 1961, and their effect on the ionosphere at Sodankyla, 1961, Nature, , 192, 1173-1174,

[Row, 1966]: Row, R. V., Evidence of long-period acoustic-gravity waves launched into the F region by the Alaskan earthquake on March 28, 1964 , 1966, J. Geophys. Res., , 71, 343-345,
[Roy et al., 2014]: Roy, C., G. Occhipinti, L. Boschi, J.-P. Molinie & M. wieczorek, Effect of ray and speed perturbations on ionospheric tomography by over-the-horizon radar: A new method, 2014, J. Geophys. Res. Space Physics, 119, , 7841-7857, doi:10.1002/2014JA020137
[Ruelle & Landeau, 1994]: Ruelle, N. & T. Landeau, Interpretation of elevation-scan HF backscatter data from Losquet Island radar, 1994, J. Atmos. Terr. Phys., , 56(1), 103-114,
[Saha et al., 1963]: Saha, A. K., M. Karabin and K. K. Mahajan , Ionospheric effect following distant nuclear detonations, 1963, J. atmospheric Terrest. Phys., , 25, 212-218,
[Saito et al., 2011]: Saito, A., T. Tsugawa, Y. Otsuka, M. Nishioka, T. Iyemori, M. Matsumura, S. Saito, C. H. Chen, Y. Goi, and N. Choosakul, Acoustic resonance and plasma depletion detected by GPS total electron content observation after the 2011 off the Pacific coast of Tohoku Earthquake, 2011, Earth Planets Space, 63, , 863-867,
[Saksman et al. (1997)]: Saksman, E., T. Nygren & M. Markkanen, ionospheric structures invisible in satellite radiotomography, 1997, Radio Science, 32, 2, 605-616,
[Sauli et al., 2006]: Sauli, P., Abry, P., Boska, J., Duchayne, L., Wavelet characterisation of ionospheric acoustic and gravity waves occuring during the solar eclipse of August 11, 1999, 2006, Journal of Atmospheric and Solar Terrestrial Physics, 68(3), , 586-598,
[Schaer, 1999]: Schaer, S., Mapping and predicting the Earth's ionosphere using the global positioning system, 1999, Geod. Geophys. Arb. Schweiz, 59, 8, ,
[Scholz et al. (1973)]: Scholz, C. H., L.R. Sykes, Y. Aggarwal , Earthquake Prediction: A Physical Basis, 1973, Science, 181, 4102, 803-810, doi:10.1126/science.181.4102.803
[Schunk & Nagy, 2000]: Schunk, R. W. and Nagy, A. F., Ionospheres, 2000, Cambridge Univ. Press, , , , https://doi.org/10.1017/CBO9780511635342
[Schunk & Nagy, 2009]: Schunk, R. W. and Nagy, A. F., Ionospheres, 2009
[Schunk, 2013]: Schunk, R. W., Ionospheric Models for Earth, 2013
[Six et al., 1996]: Six, M., J. Parent, A. Bourdillon & J. Delloue, A new multibeam receiving equipment for the Valensole skywave HF radar: description and applications, 1996, Geoscience and Remote Sensing, IEEE Transactions on,
[Smith et al., 2005]: Smith, W., R. Scharroo, V. Titov, D. Arcas, and B. Arbic, Satellite altimeters measure Tsunami, 2005, Oceanography, 18, 2, 102,
[Stephenson, 2004]: Stephenson, R., D.M. Willis, T.J. Hallinan, The earliest datable observation of the aurora borealis, 2004, Astronomy & Geophysics , 45, 6, 6.15-6.17, https://doi.org/10.1046/j.1468-4004.2003.45615.x
[Stoffregen, 1962]: Stoffregen, W., Ionospheric effects observed in connection with nuclear explosion at Novaya Zemlya on October 23 and 30, 1961, 1962
[Sun et al., 2018]: Sun, Y.-Y., Liu, J.-Y., Lin, C.-H., ... Chou, M.-Y., Ionospheric bow wave induced by the moon shadow ship over the continent of United States on 21 August 2017, 2018, Geophysical Research Letters, 45, , 538-544, https://doi.org/10.1002/2017GL075926

[Tanaka et al. (1984)]: Tanaka, T., T. Ichinose, T. Ouzawa, T. Shibata, HF-Doppler observations of acoustic waves excited by the Urakawa-Oki earthquake on 21 March 1982, 1984, J. Atmospheric Terrest. Phys., , 46, 233-245,

[Thomason, 2003]: Thomason, J.F., Development of Over-the-Horizon Radar in the United States, 2003, IEEE Radar 2003 Conference 2003, Adelaide, Australia, September 3-5, 599-601,

[Thomason, 2003]: Thomason, J.F., Development of Over-the-Horizon Radar in the United States, 2003, IEEE Radar 2003 Conference 2003, Adelaide, Australia, September 3-5, 599-601,

[Torr and Torr, 1973]: Torr, M. R. & D. G. Torr, The seasonal behaviour of the F2-layer of the ionosphere, 1973, J. Atmos. Terr. Phys., 35, , 2237-2251, doi:10.1016/0021-9169(73)90140-2

[Tsai and Liu, 1999]: Tsai, H. F. and Liu, J. Y., Ionospheric total electron content response to solar eclipses , 1999, Journal of Geophysical Research, 104(A6), , 12657, https://doi.org/10.1029/1999JA900001

[Tsai et al., 2011]: Tsai, H. F., J.-Y. Liu, C.-H. Lin, and C.-H. Chen, Tracking the epicenter and the tsunami origin with GPS ionosphere observation, 2011, Earth Planets Space, 63, , 859-862,

[Tsugawa et al., 2011]: Tsugawa, T., A. Saito, Y. Otsuka, M. Nishioka, T. Maruyama, H. Kato, T. Nagatsuma, and K. T. Murata, Ionospheric disturbances detected by GPS total electron content observation after the 2011 off the Pacific coast of Tohoku Earthquake, 2011, Earth Planet Space, 63, , 875-879,

[Unnikrishnan et al., 2002]: Unnikrishnan, K., R. B. Nair & C. Venugopal, Harmonic analysis and an empirical model for TEC over Palehua, 2002, Atmos. Sol. Terr. Phys., 64, , 1833-1840, doi:10.1016/S1364-6826(02)00187-6

[Utada & Shimizu, 2014]: Utada, H. & H. Shimizu, Comment on "Preseismic ionospheric electron enhancements revisited" by K. Heki and Y. Enomoto, 2014, Journal of Geophysical Research: Space Physics, 119, , 6011-6015,

[Uyeda et al., 2009]: Uyeda, S., M. Kamogawa & T. Nagao, Electromagnetic signals of Earthquakes, 2009, Complexity in Earthquakes, Tsunamis, and Volcanoes, and Forecasting and Early Warning of their Hazards, edited by W. H. K. Lee, Series of Encyclopedia of Complexity and System Science (Editor-in-Chief, Robert Meyers), Springer, 2621-2635,

[Uyeda et al., 2011]: Uyeda, S., T. Nagao & M. Kamogawa, Earthquake Precursors and Prediction, 2011, Encyclopedia of Solid Earth Geophysics, Springer

[van de Kamp, 2013]: van de Kamp, M.M.J.L., Ionospheric tomography: an algorithm enhancement, 2013, Annales Geophysicae 31, , , 75-89,

[van Hulsteyn, 1965]: van Hulsteyn, D. B., The atmospheric pressure wave generated by a nuclear explosion, 1965, J. Geophys. Res., , 70, 257-278,

[Vasicek & Kronschnabl, 1995]: Vasicek, C. & G. Kronschnabl, Ionospheric tomography; an algorithm enhancement, 1995, Journal of Atmospheric and Terrestrial Physics, 57, 8, 875-888,

[Vigny et al., 2005]: Vigny, C., W.J.F. Simons, S. Abu, R. Bamphenyu, C.Satirapod, N.Choosakul, C. Subarya, A. Socquet, K. Omar, H.Z. Abidin & B.A.C. Ambrosius, Insight into the 2004 Sumatra-Andaman earthquake from GPS measurement in southeast Asia, 2005, Nature, 436, , 201-206,

[Walker et al., 1997]: Walker, I., J. Heaton, L. Kerseley, C. Mitchell, S. Pryse & M. Williams, EISCAT veification in the development of ionospheric tomography, 1997, Annales Geophysicae 14(12), 1413-1421,

[Watson-Watt, 1929]: Watson-Watt, Robert A., Weather and wireless, 1929, Q. J. Royal Meteorological Society, 55, , 273,
[Webb & Daniels, 1964]: Webb, H. D. and F. B. Daniels, Ionospheric oscillations following nuclear explosion, 1964, J. Geophys. Res., , 69, 545-546,
[Wen et al., 2010]: Wen, D., S. Liu & P. Tang, Tomographic reconstruction of ionospheric electron density based on constrained algebraic reconstruction technique, 2010, GPS Solutions, 14, , 375-380,
[Wen et al., 2007]: Wen, D. Y. Yuan & J. Ou, Monitoring the three-dimensional ionospheric electron density distribution usng GPS observations over China, 2007, Journal of eath system science, 116, 3, 235-244,
[Weston, 1962]: Weston, V. H., The pressure pulse produced by a large explosion in the atmosphere, 1962, Can. J. Phys., 40, 2, 431-445,
[Wilson et al., 2005]: Wilson, C., J. Olson and H. Stenbaek-Nielsen, Infrasound from auroral electro jet motion at i53us, 2005, Geophys. Res. Lett., 32, L14, 810,
[Wilson, 1969a]: Wilson, C., Infrasonic wave generation by aurora, 1969, J. Atm. Terr. Phys., 37, 973988, ,
[Wilson, 1969b]: Wilson, C., Auroral infrasonic waves, 1969, J. Geophys. Res., 18121836, 74, ,
[Wilson, 2003]: Wilson, C., Auroral infrasound at Fairbanks, Alaska observed at CTBT infrasonic array i53us, 2003, Inframatics, , 2, 1018,
[Wilson, 2005]: Wilson, C., Infrasoun from auroral electro jet motion at i53us, 2005, Inframatics, 113, 10, ,
[Yamamoto, 1956]: Yamamoto, R., The microbarographic oscillations produced by the explosions of hydrogen bombs in the Marshall Islands, 1956, Bull. Am. Metorol. Soc., 37, , 406-409,
[Yamamoto, 1957]: Yamamoto, R., A dynamical theory of micro-barographic oscillations produced by the explosions of hydrogen bombs, 1957, J. Meteorol. Soc. Japan, 35, , 32-40,
[Yeh & Raymund, 1991]: Yeh, K.C. & T.D. Raymund, Limitations of ionospheric imaging by tomography, 1991, Radio Science, 26, 6, 1361-1380,
[Yeoman et al., 2008]: Yeoman, T.K., G. Chisham, L.J> Baddeley, R.S> Dhillon, T.J.T. Karhunen, T.R. Robinson, A. Senior & D.M. Wright, Mapping ionospheric backscatter measured by the SuperDARN HF radars - Part 2: Assessing SuperDARN virtual height models, 2008, Ann. Geophys., , 26, 843-852,
[Yizengaw et al., 2005]: Yizengaw, E., P. Dyson, E. Essex & M. Moldwin, Ionosphere dynamics over the Southern Hemisphere during 31 March 2001 severe magnetic storm using multi-instrument measurement data, 2005, Annales Geophysicae, 23
[Yonezawa, 1971]: Yonezawa, T., The solar-activity and latitudinal characteristics of the seasonal, non-seasonal and semi-annual variations in the peak electron densities of the F2-layer at noon and midnight in middle and low latitudes, 1971, J. Atmos. Terr. Phys., 33, , 889-907, doi:10.1016/0021-9169(71)90089-4
[Yu et al., 2004]: Yu, T., W. Wan, L. Liu & B. Zhao, Global scale annual and semi-annual variations of daytime NmF2 in the high solar activity years, 2004, J. Atmos. Sol. Terr. Phys., 66, , 1691-1701, doi:10.1016/j.jastp.2003.09.018
[Yuen and Roelofs, 1967]: Yuen, P. C. & T. H. Roelofs, Seasonal variations in ionospheric total electron content, 1967, J. Atmos. Terr. Phys., 29, , 321-326, doi:10.1016/0021-9169(67)90203-6

[Zeng et al., 2008]: Zeng, Z., A. Burns, W. Wang, J. Lei, S. Solomon, S. Syndergaard, L. Qian & Y. Kuo, Ionospheric annual asymmetry observed by the COSMIC radio occultation measurements and simulated by the TIEGCM, 2008, J. Geophys. Res., 113, A07305, , doi:10.1029/2007JA012897
[Zhang et al., 2017]: Zhang, S.-R.,Erickson, P. J., Goncharenko, L. P., Coster, A. J., Rideout, W., Vierinen, J., Ionospheric bow waves and perturbations induced by the 21 August 2017 solar eclipse, 2017, Geophysical Research Letters, 44, , , https://doi.org/10.1002/2017GL076054
[Zou et al., 2000]: Zou, L., H. Rishbeth, I. C. F. Muller-Wodarg, A. D. Aylward, G. H. Millward, T. J. Fuller-Rowell, D. W. Idenden & R. J. Moffett, Annual and semiannual variations in the ionospheric F2-layer: I. Modelling, 2000, Ann. Geophys., 18, , 927-944, doi:10.1007/s00585-000-0927-8